FORSCHUNGSZENTRUM KARLSRUHE

– Technik und Umwelt –

Wissenschaftliche Berichte

FZKA 5828

Comparison of Hadronic Interaction Models Used in Air Shower Simulations and of Their Influence on Shower Development and Observables

J. Knapp[a 1], **D. Heck**[b], **G. Schatz**[b]

[a]Universität Karlsruhe, Institut für Experimentelle Kernphysik, Postfach 3640, D 76021 Karlsruhe
[b]Forschungszentrum Karlsruhe, Institut für Kernphysik III, Postfach 3640, D 76021 Karlsruhe

Forschungszentrum Karlsruhe GmbH, Karlsruhe
1996

[1]corresponding author: e-mail: knapp@ik1.fzk.de

Abstract

Comparison of Hadronic Interaction Models Used in Air Shower Simulations and of Their Influence on Shower Development and Observables

In the extensive air shower simulation program CORSIKA the interaction models HDPM and VENUS are available to simulate hadronic reactions of cosmic rays in the atmosphere. In the most recent version of CORSIKA we have implemented three further interaction models which are widely used in air shower simulations, namely SIBYLL, QGSJET, and DPMJET. A comparison of the interaction models with each other and with experimental data was performed for primary nucleons, mesons, and nuclei in the energy range from $E_{lab} = 10^{11}$ to 10^{17} eV colliding with nucleons and nitrogen. In addition, the properties of 10^{14} and 10^{15} eV air showers induced by primary p and Fe nuclei simulated with the different models were examined.

Zusammenfassung

Vergleich hadronischer Wechselwirkungsmodelle für Luftschauersimulationen und ihres Einflusses auf Schauerentwicklung und beobachtbare Größen

Im Rahmen des Programmes CORSIKA zur Simulation von Luftschauern stehen die Wechselwirkungsmodelle HDPM und VENUS zur Berechnung hadronischer Stöße der kosmischen Strahlung mit den Atomkernen der Atmosphäre zur Verfügung. In die neueste Version von CORSIKA wurden drei weitere Wechselwirkungsmodelle eingebaut, die schon vielfach für Luftschauersimulationen verwendet wurden. Es handelt sich um die Programme SIBYLL, QGSJET und DPMJET. Für Nukleonen, Mesonen und Kerne im Energiebereich $E_{lab} = 10^{11}$ bis 10^{17} eV, die mit Nukleonen und Stickstoffkernen kollidieren, wurden Vergleiche der Modelle untereinander und mit experimentellen Daten durchgeführt. Außerdem wurden die Eigenschaften von 10^{14} und 10^{15} eV Luftschauern untersucht, die von primären Protonen und Eisenkernen mit den verschiedenen Modellen erzeugt werden.

Contents

1 Introduction

The interpretation of extensive air shower (EAS) measurements relies strongly on the model of the shower development in the Earth's atmosphere. Such models are used to simulate the transport of particles through the atmosphere, their interaction with air nuclei and the production of secondary particles.

The parts of the shower model which base on electromagnetic or weak interactions can be calculated with good accuracy. The hadronic interaction, however, is still subject to large uncertainties. A wealth of data exists on inelastic cross sections and particle production from $p\bar{p}$ colliders up to energies of $\sqrt{s} = 1800$ GeV and from heavy ion experiments up to energies of about 200 GeV/n. But almost all collider experiments do not register particles emitted into the forward direction. These particles carry most of the hadronic energy in an EAS and, therefore, are of utmost importance for the shower development. Since most of these particles are produced in interactions with small momentum transfer, QCD is at present not capable of calculating their energies.

During the past years many models of hadronic interactions have been built around experimental results, predominately of $p\bar{p}$ colliders. Extrapolations to higher energies, to small angle processes, and to nucleus-nucleus collisions have been performed with varying levels of sophistication.

Many EAS experiments have used specific models to determine the primary energy and to draw conclusions on the primary elemental composition of the cosmic radiation. Experience shows that different models can lead to different results when applied to the same data. Hence, considerable systematic uncertainties remain. We, therefore, considered it worthwhile to compare several interaction models applied in the analysis of cosmic ray data in a systematic way. We present a comparison of calculations with the CORSIKA air shower simulation program [10] employing five different models for the high energy hadronic interactions which have been used widely for EAS calculations. The models are HDPM [10], VENUS [19], QGSJET [15], SIBYLL [12] and DPMJET [17]. They were implemented into the CORSIKA frame with the valuable help of the respective authors.

The models VENUS, QGSJET, and DPMJET base on Gribov-Regge theory (GRT) and describe soft particle interactions by exchange of one or multiple Pomerons. Inelastic reactions are simulated by cutting Pomerons, thus, creating two color strings per Pomeron which subsequently fragment into color neutral hadrons. All three models calculate detailed nucleus-nucleus collisions by tracking the participating nucleons both in target and projectile. The differences between the models are in technical details of the realization in a Monte Carlo code, e.g. the treatment and the fragmentation of strings. An important difference is that QGSJET and DPMJET are both able to treat hard processes, whereas VENUS, in its present form, is not. VENUS on the other hand allows for secondary interactions of strings which are close to each other in space and time, which is not the case in QGSJET and DPMJET.

SIBYLL and HDPM extrapolate experimental data from low to high energies and from p to nuclei with simple theoretical ideas. Nuclei are treated as superpositions of free nucleons. SIBYLL takes the production of minijets, i.e. hard processes, into account.

In section 2 of this report we show results of interactions of nucleons, pions, and nuclei on nucleon and nucleus targets at energies of relevance for EAS simulations. In section 3 we present calculations of vertical air showers induced by $E = 10^{14}$ and 10^{15} eV protons and Fe nuclei using the five models within the standard CORSIKA program.

P	T	E_{lab} (GeV)	Diff.	P	T	E_{lab} (GeV)	Diff.
$\bar{p}$	p	50	no	π^+	N	50	yes
$\bar{p}$	p	10^2	no	π^+	N	10^2	yes
$\bar{p}$	p	10^3	no	π^+	N	10^3	yes
$\bar{p}$	p	1.50×10^3	no	π^+	N	10^4	yes
$\bar{p}$	p	10^4	no	π^+	N	10^5	yes
$\bar{p}$	p	2.13×10^4	no	π^+	N	10^6	yes
$\bar{p}$	p	10^5	no	π^+	N	10^7	yes
$\bar{p}$	p	1.59×10^5	no				
$\bar{p}$	p	4.32×10^5	no				
$\bar{p}$	p	10^6	no	N	N	10^3	yes
$\bar{p}$	p	1.73×10^6	no	N	N	10^4	yes
$\bar{p}$	p	10^7	no	N	N	10^5	yes
$\bar{p}$	p	10^8	no	N	N	10^6	yes
$\bar{p}$	p	10^9	no	N	N	10^7	yes
$\bar{p}$	p	10^{10}	no				
p	N	50	yes	Fe	N	10^4	yes
p	N	10^2	yes	Fe	N	10^5	yes
p	N	10^3	yes	Fe	N	10^6	yes
p	N	10^4	yes	Fe	N	10^7	yes
p	N	10^5	yes				
p	N	10^6	yes				
p	N	10^7	yes				

Table 1: Set of calculation runs performed for different projectiles (P) and targets (T) and varying energy for each of the models. The fourth column specifies whether diffractive events were simulated together with non-diffractive ones or not.

2 Comparison of Single Interactions

In this section we present results of CORSIKA used in its interaction test mode, where only the first reaction of a shower calculation is performed. All secondaries including the spectator nucleons from projectile and target are stored on the particle stack and the further shower calculation is omitted. In this mode many interactions can be generated in a short time with the same routines that are used for shower calculations and all information about the particles on stack can be used for later analysis.

Some models describe the production of charmed hadrons. Since these cannot be handled in CORSIKA they were treated as strange baryons or mesons. We can select whether instable particles decay or not before we analyze the output of an interaction. For this comparison we let π^0, η, hyperons, and resonances decay before the analysis.

For each of the interaction models we calculated a set of 35 runs which are listed in Tab. 1. Each run contains 10000 interactions. The calculations for $\bar{p}$-p were forced to be non-diffractive interactions in order to be comparable with non-diffractive collider data. All the other calculations contain a mixture of diffractive and non-diffractive events according to the model used. The calculations for $\bar{p}$-p at $E_{lab} = 1.50{\times}10^3, 2.13{\times}10^4, 1.59{\times}10^5, 4.32{\times}10^5$, and $1.73{\times}10^6$ GeV correspond to $E_{cm} = 53$, 200, 546, 900, and 1800 GeV. For these energies experimental data from collider experiments exist.

All secondary particles were registered without any energy cut.

The spectator particles have not been included in the plots. As no information is available from the generators at to which of the particles are spectators, we had to apply cuts to identify spectator nucleons. We define all particles as spectators which are protons or neutrons *and* emerge from the collision point exactly along the beam axis *and* have a Lorentz factor within 0.002 of 1 (target spectators) or of the Lorentz factor of the projectile (projectile spectators). Depending on the model we may misinterpret some of the secondary particles as spectators and vice versa.

2.1 $\bar{p}$-p Collisions

The most simple reaction is the $\bar{p}$-p reaction which has been studied in detail at the SPS and Fermilab colliders. In Tabs. 2 and 3 measured particle multiplicities at $E_{lab} = 200$ GeV [13] and at collider energies [8, 14] are compared with simulation results. Since the leading particles systematically escape detection in experiments, the experimental values were corrected for comparison with the simulations. We increased n_{ch} by 2, $(p + \bar{p})$ by 1.5, and $(n + \bar{n})$ by 0.5 to account for this bias. In general the particle numbers are reproduced and the experimental values are well within the scatter of the simulated values. For all the models the numbers of kaons produced are systematically larger than the experimental values. There is no model describing the data clearly better than the other ones.

Tab. 4 shows the average particle numbers for 10^{14}, 10^{15}, and 10^{16} eV collisions. Besides the mean values the standard deviations σ over the 10000 interactions are given. The errors of the mean values $(\sigma/\sqrt{10000})$ are much smaller.

The models agree in the number of photons produced to about 8% at 10^{14} eV but differ by 30% at 10^{16} eV. VENUS produces the smallest number of photons at high energies and QGSJET the largest one. SIBYLL produces 30 to 50% less nucleons than the other models and has, for all particles, the by far smallest fluctuations. HDPM shows most nucleons.

For higher energies (10^{15} and 10^{16} eV) the number of particles produced increases by about 40% per decade. The number of photons grows a little faster than the rest. Again, SIBYLL produces less baryons and charged pions than the other models and has the smallest fluctuation. At 10^{16} eV QGSJET produces more baryons and pions than VENUS and DPMJET and only HDPM is still higher.

In Tab. 5 the energy fraction going into the different secondary particles is shown for various energies. It is obvious that the leading particle effect giving much energy to the few $\bar{p}$ and $\bar{n}$. About 35 to 40% of the energy is transferred to charged and neutral pions for the HDPM model, decreasing with rising energy. VENUS, QGSJET, and SIBYLL feed $\approx 50\%$ into pions, whereas for DPMJET this value reaches about 60%. A preference for negative pions can be recognized, again showing the leading particle effect.

Tab. 6 shows the frequency of the most energetic secondary particle of the collision. The values are given in %. HDPM preserves best the projectile particle which is a $\bar{p}$. In about 85% the most energetic particle is an antinucleon. The other models give 55% to 71%. In roughly one third of the collisions mesons emerge as most energetic secondaries. VENUS generates a kaon as highest energy particle in about 10% of the cases whereas other models are lower with 3.5% for HDPM to 7.5% for DPMJET. HDPM has the smallest fraction of pions and photons as highest energy particles and their frequencies are even decreasing with increasing energy. Moreover, the energy dependence of the percentages is small, the most conspicuous feature being a slow increase of the fraction of kaons.

The plots 1 and 2 give the Feynman x_F distributions in the cm system for baryons, photons, and charged mesons for $\bar{p}$-p reactions at 10^{14} and 10^{16} eV. There is roughly a difference of an order of magnitude in the number of baryons at $x_F \approx 1$. It is evident that target and projectile are baryons

and, thus, lead to baryons in the fragmentation region. DPMJET produces the smallest number of forward baryons which can also be seen from Tab. 6. HDPM exhibits pronounced shoulders which represent the treatment of the leading particle. The corresponding plots for photons and mesons show better agreement among the models, but the differences are still about a factor of 2 to 5 for larger x_F. HDPM gives the lowest densities of photons and SIBYLL and DPMJET the highest ones. For mesons all models produce similar distributions. Only HDPM has a deficit of about 40% at $|x_F| \approx 0.1$. The photon distributions have smaller tails than the meson distributions, since the momentum of the parent π^0 is shared by the two decay photons, and therefore x_F is about half of the corresponding meson value.

In Fig. 3 multiplicity distributions of charged particles in collisions at 10^{15} eV are plotted. The solid line represents a negative binomial distribution of the form

$$P(N_{ch}, \langle N_{ch}\rangle, k) = \binom{N_{ch}+k-1}{N_{ch}} \left(\frac{\langle N_{ch}\rangle/k}{1+\langle N_{ch}\rangle/k}\right)^{N_{ch}} \left(\frac{1}{1+\langle N_{ch}\rangle/k}\right)^{k}$$

with the parameters k according to the parameterization of UA5 [4] $1/k = -0.104 + 0.058 \log\sqrt{s}$ and $\langle N_{ch}\rangle = \sum N_{ch} P_{N_{ch}} = 31.3$. This number corresponds to the result of UA5 at this energy, corrected by 2 for the fact that UA5 cannot see the 2 leading particles which vanish in the beam pipe, whereas in the MC simulations we count them as well. The negative binomial distribution describes the MC data well for all models except for SIBYLL. With SIBYLL we obtain $\langle N_{ch}\rangle = 28.9 \pm 9.52$, whereas the VENUS values are $\langle N_{ch}\rangle = 33.82 \pm 18.40$. The mean value of SIBYLL is lower by 15% and the fluctuations are smaller by a factor of 2. DPMJET seems to show a deviation from the negative binomial form for high multiplicities as well. The Gribov-Regge type models follow the negative binomial distribution mainly due to the fluctuations of the number of cut Pomerons, i.e. the number of strings produced. In SIBYLL there are only 2 strings produced per interaction (not regarding the mini-jets) and, hence, this source of fluctuations does not exist. HDPM generates a negative binomial distribution by construction. All the models seem to have fewer reactions with small multiplicities than predicted by the negative binomial distribution. This effect is most pronounced for SIBYLL and DPMJET which have no events below multiplicity 5.

In Fig. 4 the average charged multiplicity is shown versus the cm energy of the nucleon-antinucleon system. The models agree reasonably well with experimental data in the low energy part, just VENUS being low by about 40% at $E_{cm} = 10$ GeV. The rise with energy is most pronounced for QGSJET and HDPM, in QGSJET due to semi-hard processes, in HDPM due to the power law parameterization $\langle n_{ch}\rangle \propto s^{0.17}$. VENUS and DPMJET overlap almost perfectly for higher energies even though DPMJET produces mini-jets and VENUS does not. SIBYLL is 5 to 10 particles below the other models at high energies, the slope of the increase, however, seems to become steeper. The mini-jets obviously do not yet increase the multiplicity in the energy range displayed. We have simulated $\bar{p}$-p interactions up to 10^{19} eV for all models except for DPMJET and VENUS, which only work up to 10^{18} and 10^{16} eV, respectively, due to technical and physical limitations. A plot of the average charged multiplicity extended to these energies is shown in Fig. 5. QGSJET exhibits a drastic increase of the multiplicity as expected from mini-jet production. At 10^{19} eV QGSJET produces an average of 260 charged secondaries. HDPM reaches multiplicities of about 200 due to the power law parameterization. SIBYLL and DPMJET generate much smaller multiplicities of about 100 or below at highest energies.

In Fig. 6 the transverse momentum distributions of charged particles are shown. The form of the distributions can be described reasonably well by the form

$$E\frac{d^3\sigma}{dp^3} \propto \frac{dN}{dp_\perp^2} \propto \left(\frac{p_0}{p_0+p_\perp}\right)^n \qquad \text{or} \qquad \frac{dN}{dp_\perp} \propto \frac{(n-1)(n-2)}{p_0^2}\left(\frac{p_0}{p_0+p_\perp}\right)^n p_\perp$$

which gives an average value $\langle p_\perp\rangle = 2p_0/(n-3)$. HDPM has most high $p_\perp$ particles. Below $p_\perp = 1$

GeV/c the distributions agree within 40%. The distributions differ most for large values of $p_\perp$ which, however, represent only a very small fraction of all secondaries.

In Fig. 7 the rise of the average transverse momentum of charged particles with energy is shown. Only SIBYLL reproduces the experimental data for all energies reasonably well. At low energies DPMJET is 10% high, VENUS is 10% low and QGSJET is low by 30%. At high energies VENUS is systematically too low, possibly due to the lack of hard processes producing high $p_\perp$ secondaries. QGSJET and SIBYLL results follow nicely the experimental data due to mini-jet production, whereas HDPM and DPMJET fall low by 10%. Fig. 8 shows the average $p_\perp$ for laboratory energies up to 10^{19} eV. SIBYLL predicts the largest rise to about 0.58 GeV/c. QGSJET levels off at about 0.5 GeV/c.

Fig. 9 shows the fraction of the primary energy that goes into secondary photons (electromagnetic inelasticity). This quantity strongly influences the shower development because the energy in the electromagnetic channel is absorbed quickly and lost from the hadronic cascade. The energy fraction is basically energy independent for SIBYLL and DPMJET and slightly increasing for VENUS and QGSJET. HDPM shows a strong 40% decrease with cm energy which is correlated with the increase of elasticity seen in Fig. 10. Although the change with energy is similar for the other models, the amounts differ by about 25% with DPMJET transferring 22% and VENUS 17% of the energy in each collision into photons.

The energy fraction carried away by the highest energy baryon (elasticity) as a function of the cm energy is plotted in Fig. 10. Here HDPM is the only model showing a rise, whereas the others decline or stay constant. (The increase of HDPM leaves less energy to be shared amongst the secondaries and automatically leads to a decrease of, e.g., the energy fraction going into secondaries.) DPMJET gives the lowest of all elasticities, which corresponds to the highest energy fraction going into photons in the previous plot. At low energies the elasticity of VENUS is about 0.45 and at higher energies 0.32.

Figures 11, 12, 13, 14, and 15 show the pseudo rapidity distributions for $E_{cm} = 53$, 200, 540, 900 and 1800 GeV in comparison with UA5 and CDF data. At 53 GeV HDPM and DPMJET predict 20% higher values, the other models agree well with the data. With rising energy the agreement with the data becomes worse for $\eta > 3$, the spread between the models is of the order of 20 to 30%. The three models based on GRT predict rather similar shapes, all having higher values at $\eta > 3$. Only HDPM, which gives too high a pseudo rapidity density around $\eta = 2$, reproduces the slope of the experimental distributions at high η. Between $\eta = 3$ and 5 the detection efficiency of UA5 goes down to zero and the correction for this effect in the experimental data has been obtained by the UA5 MC generator. SIBYLL exhibits a deficit around $\eta = 2$ but gives the right central pseudo rapidity density and the same distribution for $\eta > 5$ as the other models.

The pseudo rapidity distributions are shown in Fig. 16 on a logarithmic scale for a low and the highest energy, 200 and 1800 GeV. Here the very forward part of the distributions can be seen in more detail. There are discrepancies of one order of magnitude between the models and still a factor of 5 or so between the GRT based models. The pseudo rapidity density in very forward direction is dominated by the low $p_\perp$ part of the particle production rather than by differences in the region $x_F \approx 1$ being obvious from the definition of pseudo rapidity

$$\eta = \frac{1}{2} \log \left(\frac{p + p_z}{p - p_z} \right) = \frac{1}{2} \log \left(\frac{(p + p_z)^2}{p^2 - p_z^2} \right) \approx \log \left(\frac{2p}{p_\perp} \right) \quad .$$

	Exp.	VENUS	QGSJET	SIBYLL	HDPM	DPMJET
n_{ch}	9.69 $\pm$0.06 †	7.94	10.04	9.49	10.55	9.95
p	2.84 $\pm$0.15 †	1.34	1.24	1.46	1.82	1.46
n	1.11 $\pm$0.30 †	0.96	1.04	0.86	0.46	1.02
π^+	3.22 $\pm$ 0.12	2.95	4.07	3.72	4.11	3.89
π^-	2.62 $\pm$ 0.06	2.94	4.07	3.72	4.11	3.88
γ	6.68 $\pm$ 0.48	6.65	10.40	9.93	8.02	9.55
K^+	0.28 $\pm$ 0.06	0.30	0.27	0.24	0.20	0.30
K^-	0.18 $\pm$ 0.05	0.29	0.27	0.25	0.20	0.30
K^0_S	0.17 $\pm$ 0.01	0.26	0.26	0.24	0.07	0.27

†: for the leading particles 2 was added to n_{ch}, 1.5 to p and 0.5 to n.

Table 2: Particle production in $E_{lab} = 200$ GeV p-p collisions. The experimental values are from ref. [13]. The relative statistical errors of the simulated values are much smaller than 1% due to the large number of simulated interactions.

$\sqrt{s} = 53$ GeV						
	Exp.	VENUS	QGSJET	SIBYLL	HDPM	DPMJET
n_{ch}	12.5 ± 0.2 †	13.62	14.19	13.86	15.53	15.72
$p + \bar{p}$	1.8 ± 0.05 *†	1.72	1.53	1.64	1.96	1.78
$n + \bar{n}$	0.8 ± 0.05 *†	1.27	1.26	1.03	0.97	1.30
$\pi^- + \pi^+$	≈ 9.2	10.60	11.51	11.11	12.61	12.63
$K^- + K^+$	0.74 ± 0.11 *	1.15	0.97	0.95	0.81	1.13
$K^{0L} + K^{0S}$	0.74 ± 0.11 *	1.09	0.98	0.93	0.78	1.09
γ	11.2 ± 0.7	12.03	14.81	14.95	13.61	15.26
$\sqrt{s} = 200$ GeV						
	Exp.	VENUS	QGSJET	SIBYLL	HDPM	DPMJET
n_{ch}	22.4 ± 0.4 †	24.31	21.84	21.12	23.68	24.93
$p + \bar{p}$	2.0 ± 0.2 *†	2.44	2.10	1.87	2.53	2.29
$n + \bar{n}$	1.5 ± 0.2 *†	1.93	1.79	1.30	1.56	1.76
$\pi^- + \pi^+$	17.9 ± 0.5	19.38	17.56	17.30	19.31	20.41
$K^- + K^+$	1.50 ± 0.18 *	2.21	1.92	1.71	1.58	1.95
$K^{0L} + K^{0S}$	1.50 ± 0.18 *	2.08	1.89	1.67	1.36	1.86
γ	22.2 ± 2.4	22.28	23.14	23.37	23.09	24.57
$\sqrt{s} = 546$ GeV						
	Exp.	VENUS	QGSJET	SIBYLL	HDPM	DPMJET
n_{ch}	30.4 ± 0.3 †	33.82	30.48	28.87	32.86	33.86
$p + \bar{p}$	2.95 ± 0.15 *†	3.14	2.75	2.12	3.44	2.73
$n + \bar{n}$	1.95 ± 0.15 *†	2.55	2.33	1.56	2.22	2.17
$\pi^- + \pi^+$	23.9 ± 0.4	27.14	24.50	23.90	26.57	27.96
$K^- + K^+$	2.24 ± 0.16 *	3.16	2.87	2.50	2.46	2.77
$K^{0L} + K^{0S}$	2.24 ± 0.16 *	3.03	2.91	2.44	2.39	2.67
γ	33.0 ± 3.0	31.14	32.89	32.41	34.77	33.52
$\sqrt{s} = 900$ GeV						
	Exp.	VENUS	QGSJET	SIBYLL	HDPM	DPMJET
n_{ch}	36.6 ± 0.9 †	39.60	36.88	33.81	38.03	39.49
$p + \bar{p}$	2.5 ± 0.4 *†	3.56	3.19	2.33	4.05	3.03
$n + \bar{n}$	1.5 ± 0.4 *†	2.96	2.73	1.72	2.66	2.54
$\pi^- + \pi^+$	29.9 ± 1.0	31.82	29.64	28.07	30.43	32.74
$K^- + K^+$	2.74 ± 0.30 *	3.79	3.62	3.02	3.10	3.25
$K^{0L} + K^{0S}$	2.74 ± 0.30 *	3.65	3.59	2.97	2.96	3.15
γ	41.4 ± 4.1	36.50	39.60	37.99	41.48	39.03

*: $\sigma(p + \bar{p}) = \sigma(n + \bar{n})$ and $\sigma(K^+ + K^-) = \sigma(K^0 + \overline{K^0})$ was assumed.

†: for the leading particles 2 was added to n_{ch}, 1.5 to $p + \bar{p}$ and 0.5 to $n + \bar{n}$.

Table 3: Particle production in non-diffractive $\bar{p}$-p collisions. The experimental values are from ref. [7, 14] and were corrected for the leading particles (see text). The relative statistical errors of the simulated values are much smaller than 1% due to the large number of simulated interactions.

$E_0 = 10^{14}$ eV					
	VENUS	QGSJET	SIBYLL	HDPM	DPMJET
p	1.5 ± 1.2	1.3 ± 1.0	1.0 ± 0.8	1.6 ± 1.1	1.3 ± 1.0
$\bar{p}$	1.5 ± 1.2	1.3 ± 1.0	1.1 ± 0.8	1.6 ± 1.1	1.3 ± 1.0
n	1.2 ± 1.1	1.1 ± 1.0	0.7 ± 0.8	1.0 ± 1.0	1.1 ± 1.0
$\bar{n}$	1.2 ± 1.1	1.1 ± 1.0	0.7 ± 0.8	1.0 ± 1.0	1.1 ± 1.0
γ	29.0 ± 16.9	30.3 ± 18.9	30.1 ± 12.1	31.2 ± 16.8	31.4 ± 14.5
π^-	12.7 ± 7.1	11.4 ± 6.9	11.1 ± 4.0	12.2 ± 6.6	13.1 ± 5.7
π^+	12.6 ± 7.1	11.4 ± 6.9	11.2 ± 4.0	12.2 ± 6.6	13.1 ± 5.7
K^{0L}	1.4 ± 1.5	1.3 ± 1.3	1.2 ± 1.2	1.1 ± 1.0	1.2 ± 1.3
K^{0S}	1.4 ± 1.5	1.3 ± 1.3	1.1 ± 1.2	1.1 ± 1.0	1.3 ± 1.3
K^-	1.5 ± 1.5	1.3 ± 1.3	1.2 ± 1.1	1.1 ± 1.2	1.3 ± 1.3
K^+	1.5 ± 1.4	1.3 ± 1.3	1.2 ± 1.1	1.1 ± 1.2	1.3 ± 1.3
$E_0 = 10^{15}$ eV					
	VENUS	QGSJET	SIBYLL	HDPM	DPMJET
p	2.0 ± 1.5	1.8 ± 1.4	1.2 ± 0.9	2.3 ± 1.5	1.6 ± 1.2
$\bar{p}$	2.0 ± 1.5	1.8 ± 1.4	1.2 ± 0.9	2.3 ± 1.5	1.6 ± 1.2
n	1.6 ± 1.4	1.6 ± 1.3	0.9 ± 0.9	1.6 ± 1.4	1.4 ± 1.2
$\bar{n}$	1.6 ± 1.5	1.6 ± 1.3	0.9 ± 0.9	1.6 ± 1.4	1.4 ± 1.2
γ	41.1 ± 24.7	46.5 ± 31.1	42.8 ± 17.9	47.4 ± 26.9	44.2 ± 21.4
π^-	17.8 ± 10.3	17.4 ± 11.6	15.8 ± 6.1	17.2 ± 9.9	18.4 ± 8.7
π^+	17.8 ± 10.3	17.4 ± 11.6	15.8 ± 6.2	17.2 ± 9.9	18.4 ± 8.7
K^{0L}	2.1 ± 2.0	2.2 ± 1.9	1.7 ± 1.6	1.8 ± 1.5	1.8 ± 1.7
K^{0S}	2.1 ± 2.0	2.2 ± 1.9	1.7 ± 1.6	1.8 ± 1.5	1.8 ± 1.7
K^-	2.1 ± 2.0	2.2 ± 1.9	1.7 ± 1.4	1.8 ± 1.7	1.9 ± 1.6
K^+	2.2 ± 2.0	2.1 ± 1.9	1.7 ± 1.4	1.8 ± 1.7	1.8 ± 1.6
$E_0 = 10^{16}$ eV					
	VENUS	QGSJET	SIBYLL	HDPM	DPMJET
p	2.5 ± 1.9	2.6 ± 2.0	1.5 ± 1.1	3.4 ± 2.3	2.0 ± 1.4
$\bar{p}$	2.5 ± 1.9	2.6 ± 2.0	1.5 ± 1.1	3.4 ± 2.3	2.0 ± 1.4
n	2.1 ± 1.8	2.3 ± 1.9	1.2 ± 1.1	2.7 ± 2.2	1.7 ± 1.4
$\bar{n}$	2.1 ± 1.8	2.3 ± 1.9	1.2 ± 1.1	2.7 ± 2.2	1.8 ± 1.4
γ	54.0 ± 33.6	72.1 ± 53.7	60.2 ± 28.5	68.8 ± 43.1	58.5 ± 29.5
π^-	23.4 ± 14.1	26.8 ± 19.8	22.3 ± 10.1	25.2 ± 15.9	24.4 ± 12.0
π^+	23.3 ± 14.0	26.8 ± 19.8	22.2 ± 10.1	25.2 ± 16.0	24.4 ± 12.0
K^{0L}	2.7 ± 2.5	3.5 ± 3.0	2.4 ± 2.0	3.0 ± 2.4	2.4 ± 2.1
K^{0S}	2.7 ± 2.5	3.5 ± 3.0	2.4 ± 2.1	3.0 ± 2.4	2.4 ± 2.1
K^-	2.9 ± 2.5	3.5 ± 3.0	2.5 ± 1.9	3.0 ± 2.5	2.5 ± 2.0
K^+	2.9 ± 2.5	3.4 ± 3.0	2.5 ± 2.0	3.0 ± 2.5	2.5 ± 2.0

Table 4: Average numbers of secondary particles and variances in non-diffractive collisions of 10^{14}, 10^{15}, and 10^{16} eV $\bar{p}$ on p.

$E_0 = 10^{14}$ eV					
	VENUS	QGSJET	SIBYLL	HDPM	DPMJET
p	1.59	1.33	1.15	1.71	1.43
n	1.48	1.29	1.41	1.62	1.40
$\bar{p}$	22.99	21.43	28.17	36.53	17.77
$\bar{n}$	14.87	17.92	10.42	12.97	11.75
γ	17.17	18.91	19.97	14.26	22.26
π^-	16.62	16.22	17.23	14.71	19.89
π^+	14.04	13.81	13.91	11.27	16.88
K^{0L}	2.59	2.53	1.96	1.72	2.06
K^{0S}	2.64	2.06	1.92	1.63	2.11
K^-	3.70	2.57	2.10	1.75	2.42
K^+	2.16	1.76	1.63	1.74	1.87
$E_0 = 10^{15}$ eV					
	VENUS	QGSJET	SIBYLL	HDPM	DPMJET
p	1.63	1.52	1.28	2.01	1.55
n	1.55	1.42	1.21	1.98	1.49
$\bar{p}$	22.16	19.53	27.80	40.73	17.17
$\bar{n}$	14.05	16.08	10.45	10.40	11.48
γ	17.33	19.89	20.02	12.98	22.45
π^-	16.74	16.92	17.65	14.67	19.92
π^+	14.29	15.00	13.87	10.02	16.99
K^{0L}	2.88	2.57	1.91	1.67	2.12
K^{0S}	2.91	2.16	1.87	1.75	2.22
K^-	3.90	2.77	2.08	1.83	2.54
K^+	2.42	2.00	1.73	1.89	1.90
$E_0 = 10^{16}$ eV					
	VENUS	QGSJET	SIBYLL	HDPM	DPMJET
p	1.75	1.72	1.22	2.45	1.63
n	1.61	1.56	1.30	2.19	1.46
$\bar{p}$	21.18	17.43	27.35	42.91	16.97
$\bar{n}$	13.93	14.66	10.47	10.67	11.38
γ	17.62	20.88	20.01	9.78	22.11
π^-	17.07	17.78	17.52	14.52	19.99
π^+	14.26	15.98	14.05	9.63	16.97
K^{0L}	2.93	2.61	2.10	1.97	2.24
K^{0S}	2.99	2.25	1.95	1.94	2.29
K^-	4.10	2.90	2.13	1.93	2.68
K^+	2.44	2.07	1.75	1.96	2.09

Table 5: Energy fraction going into secondary particles (in %) in non-diffractive collisions of 10^{14}, 10^{15}, and 10^{16} eV $\bar{p}$ on p.

$E_0 = 10^{14}$ eV					
	VENUS	QGSJET	SIBYLL	HDPM	DPMJET
p	1.23	0.86	0.96	0.97	1.19
$\bar{p}$	41.84	39.41	48.53	63.09	34.09
n	1.19	0.70	1.48	0.99	1.18
$\bar{n}$	27.68	32.13	17.99	21.11	21.67
γ	4.51	5.83	7.81	2.04	9.38
π^-	8.06	9.73	11.00	4.19	13.98
π^+	6.97	7.20	7.43	4.11	11.69
K^{0L}	1.99	1.24	1.39	0.80	1.58
K^{0S}	2.03	1.00	1.19	0.82	1.68
K^-	2.92	1.03	1.29	0.85	2.25
K^+	1.55	0.87	0.84	1.02	1.28
$E_0 = 10^{15}$ eV					
	VENUS	QGSJET	SIBYLL	HDPM	DPMJET
p	1.20	1.20	1.16	1.14	1.36
$\bar{p}$	41.49	36.01	48.07	69.03	33.26
n	1.30	0.85	1.17	1.19	1.29
$\bar{n}$	27.37	28.95	18.48	16.56	22.06
γ	4.29	7.05	7.50	1.30	9.38
π^-	8.59	11.27	10.98	3.73	14.01
π^+	6.64	9.44	7.71	3.47	11.60
K^{0L}	2.01	1.26	1.28	0.86	1.60
K^{0S}	2.22	1.07	1.18	0.86	1.80
K^-	3.04	1.70	1.39	0.81	2.32
K^+	1.84	1.15	1.04	1.05	1.25
$E_0 = 10^{16}$ eV					
	VENUS	QGSJET	SIBYLL	HDPM	DPMJET
p	1.33	1.21	1.10	1.39	1.36
$\bar{p}$	40.61	32.06	47.80	70.18	33.99
n	1.35	1.16	1.25	1.20	1.17
$\bar{n}$	27.03	26.90	18.29	16.07	22.06
γ	4.79	8.55	7.54	0.48	8.78
π^-	8.43	13.08	11.08	3.51	13.38
π^+	6.50	11.47	7.71	3.87	11.52
K^{0L}	2.14	1.40	1.41	0.94	1.96
K^{0S}	2.47	1.26	1.27	0.80	1.82
K^-	3.60	1.88	1.46	0.70	2.46
K^+	1.74	1.01	1.05	0.86	1.47

Table 6: Most energetic secondary particles (in %) in non-diffractive collisions of 10^{14}, 10^{15}, and 10^{16} eV $\bar{p}$ on p.

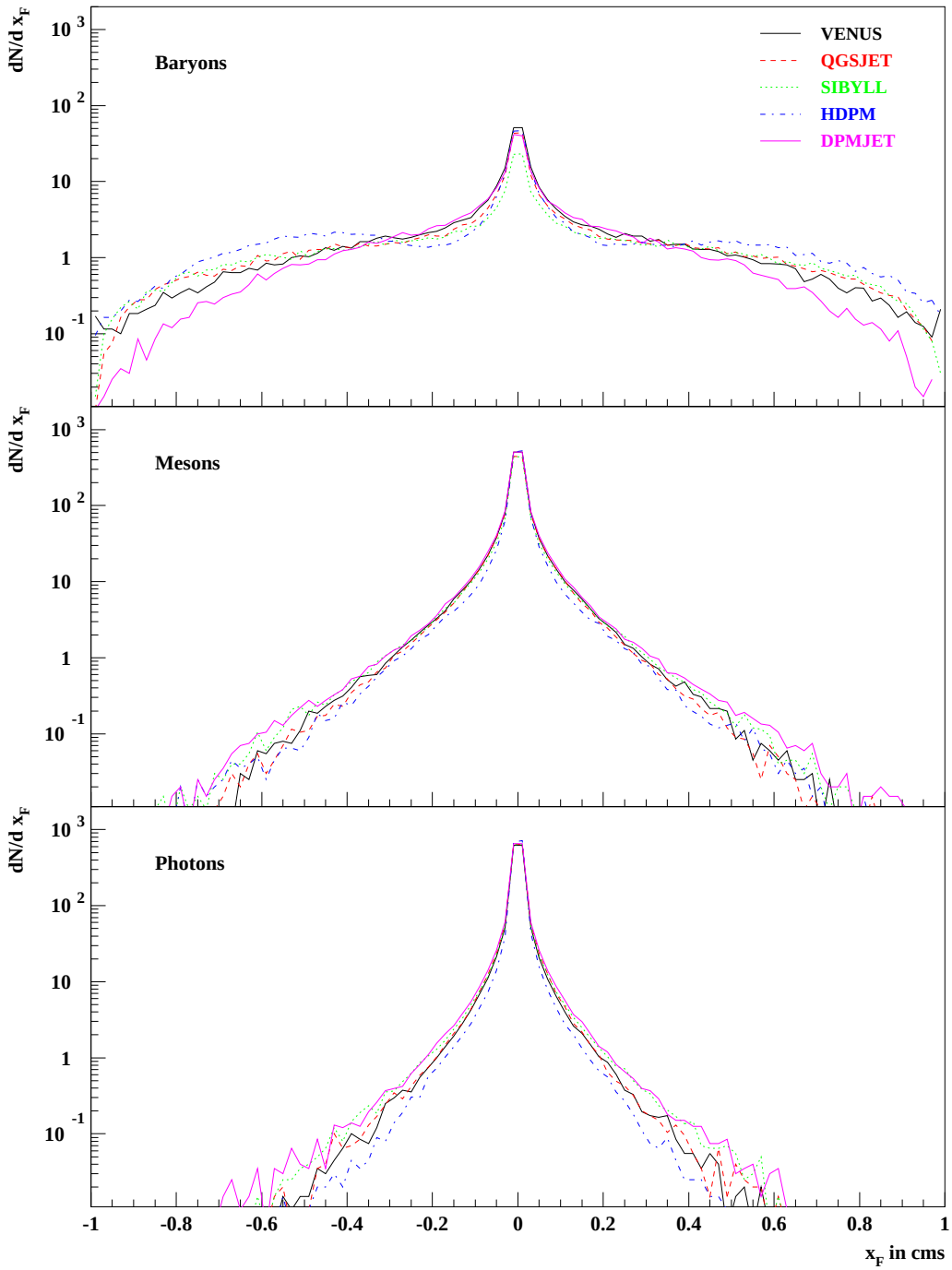

Figure 1: Feynman x_F distributions for baryons, mesons, and photons from non-diffractive collisions of 10^{14} eV $\bar{p}$ on p.

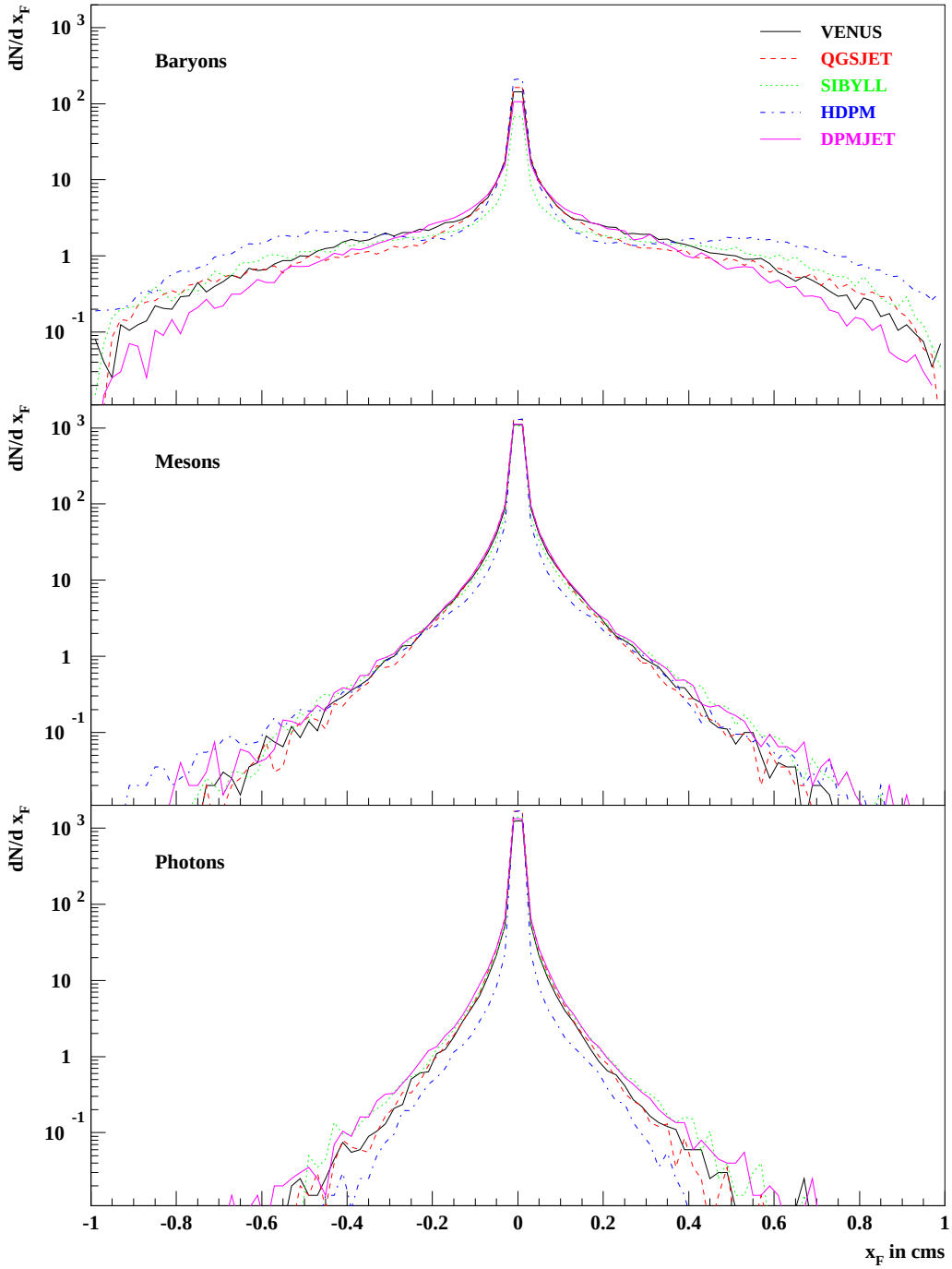

Figure 2: Feynman x_F distributions for baryons, mesons, and photons from non-diffractive collisions of 10^{16} eV $\bar{p}$ on p.

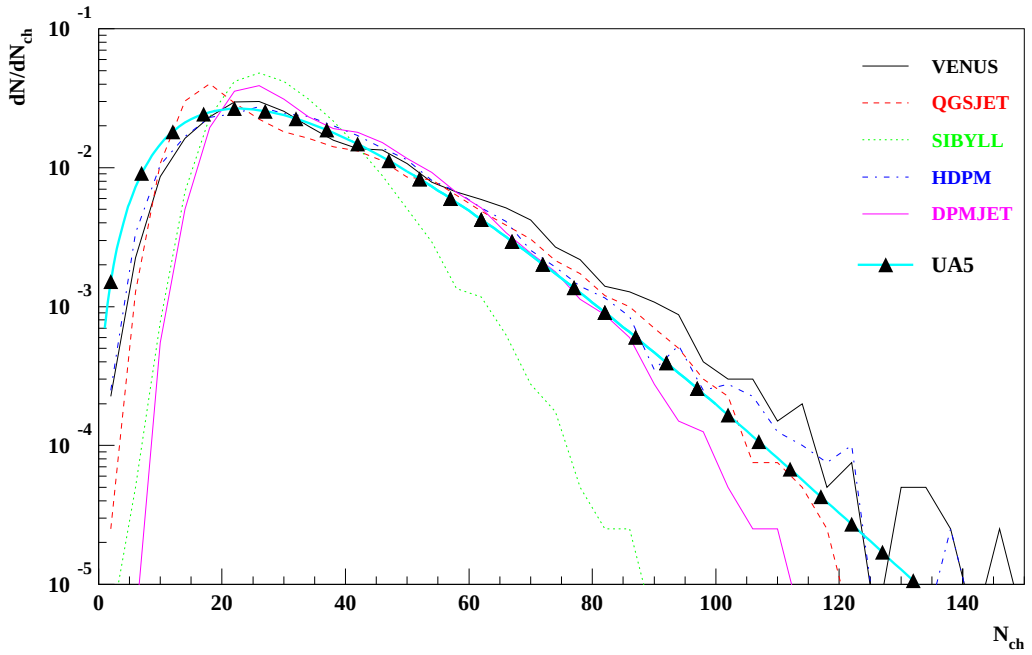

Figure 3: Multiplicity distributions of charged particles from non-diffractive collisions of $\bar{p}$ on p with $E_{cm} = 540$ GeV. The blue solid curve and the triangles give the negative binomial distribution with parameterization from UA5 for k [4] and $\langle n_{ch} \rangle = 31.3$.

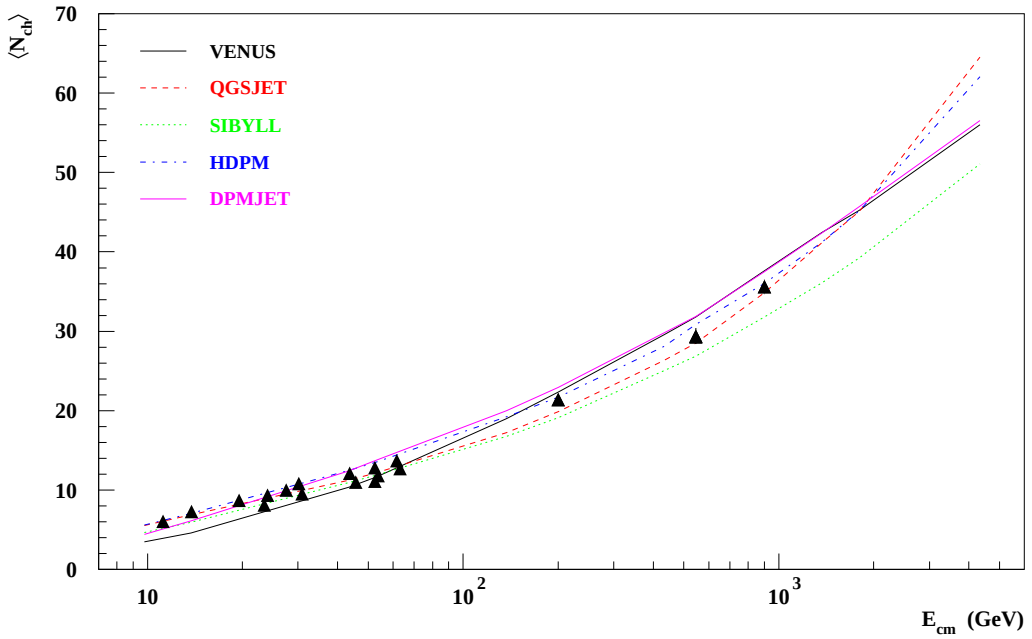

Figure 4: Average charged multiplicities from non-diffractive collisions of $\bar{p}$ on p as a function of the cm energy. The triangles give experimental values from refs. [5, 8, 18, 20].

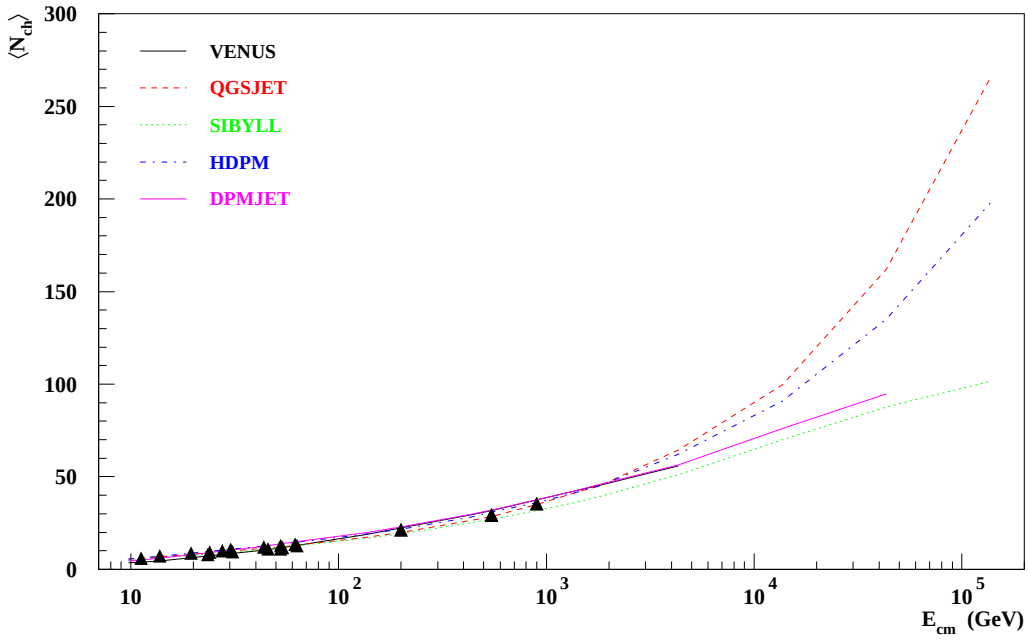

Figure 5: Average charged multiplicities from non-diffractive collisions of $\bar{p}$ on p as a function of the cm energy. The plot includes values up to $E_{lab} = 10^{19}$ eV corresponding to $E_{cm} = 1.4 \times 10^5$ GeV.

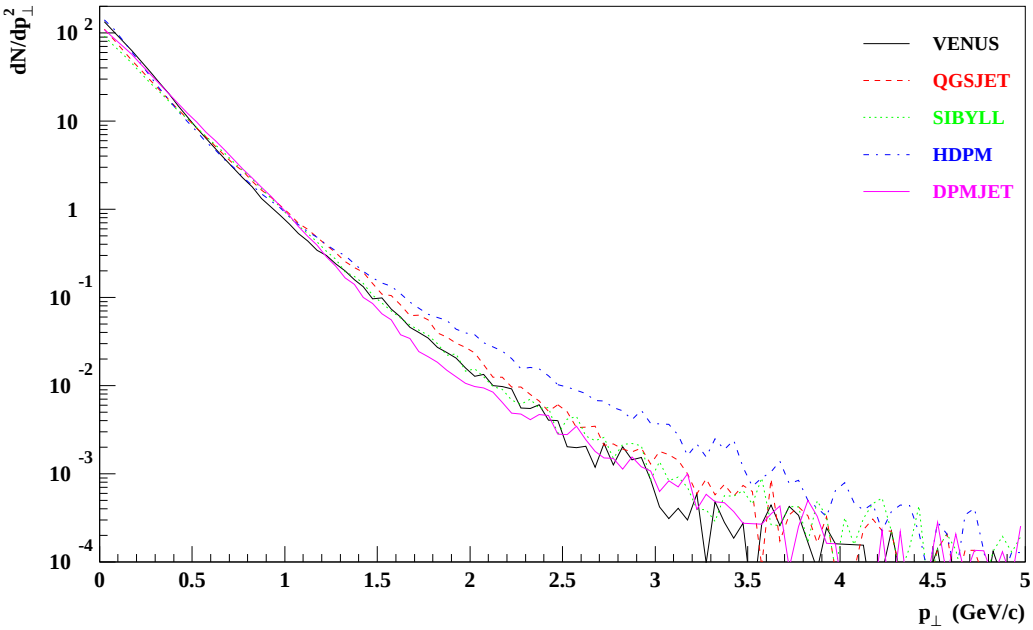

Figure 6: Transverse momentum distributions of charged particles from non-diffractive collisions of $\bar{p}$ on p at $E_{cm} = 540$ GeV.

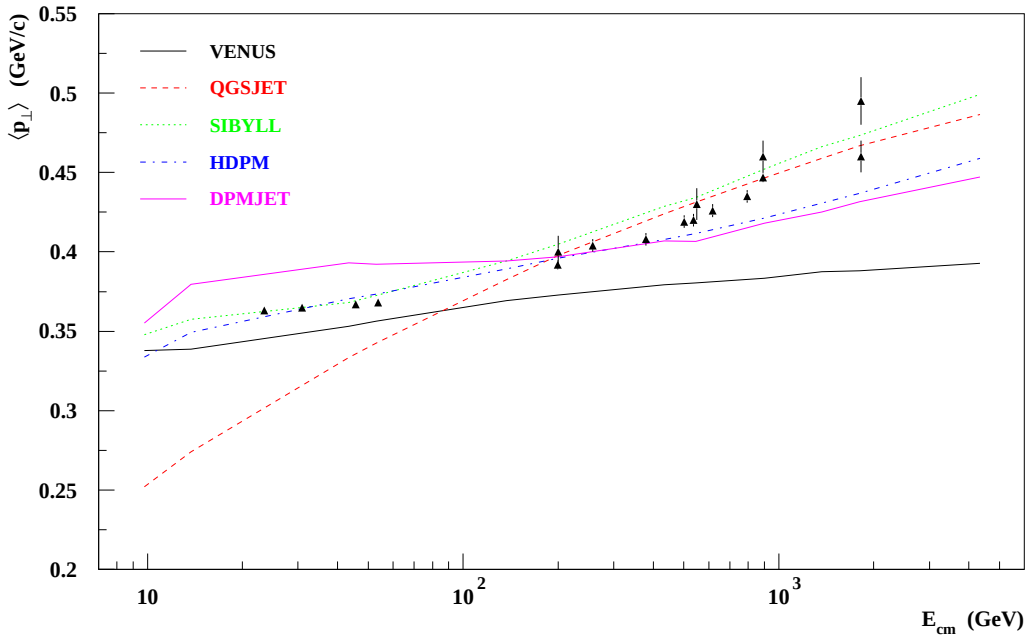

Figure 7: Average transverse momenta of charged particles from non-diffractive collisions of $\bar{p}$ on p as a function of the cm energy. The triangles give experimental values from refs. [2, 5].

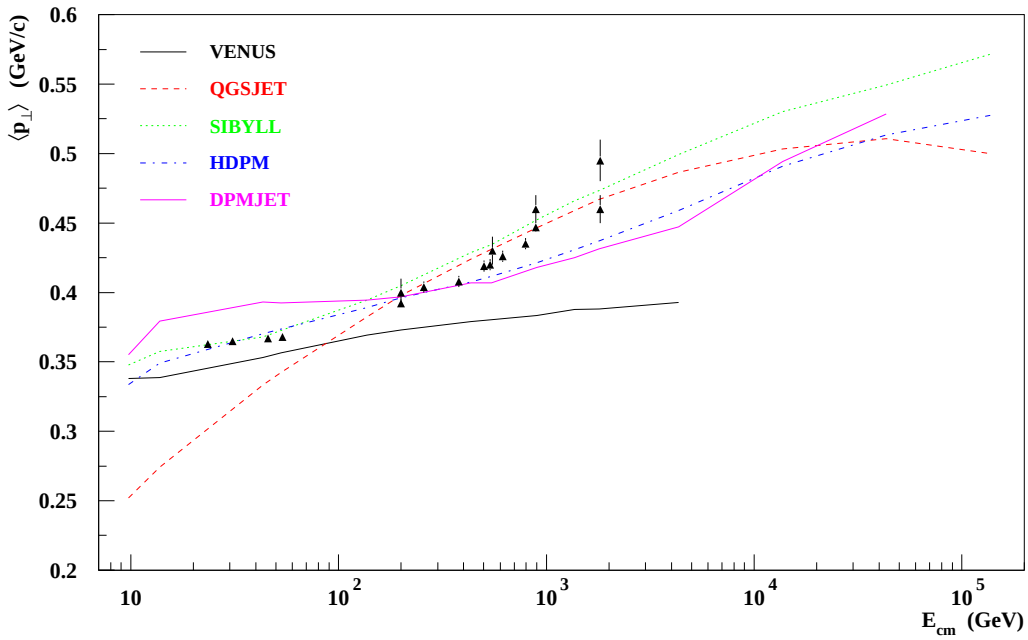

Figure 8: Average transverse momenta of charged particles from non-diffractive collisions of $\bar{p}$ on p as a function of the cm energy. The plot includes values up to $E_{lab} = 10^{19}$ eV.

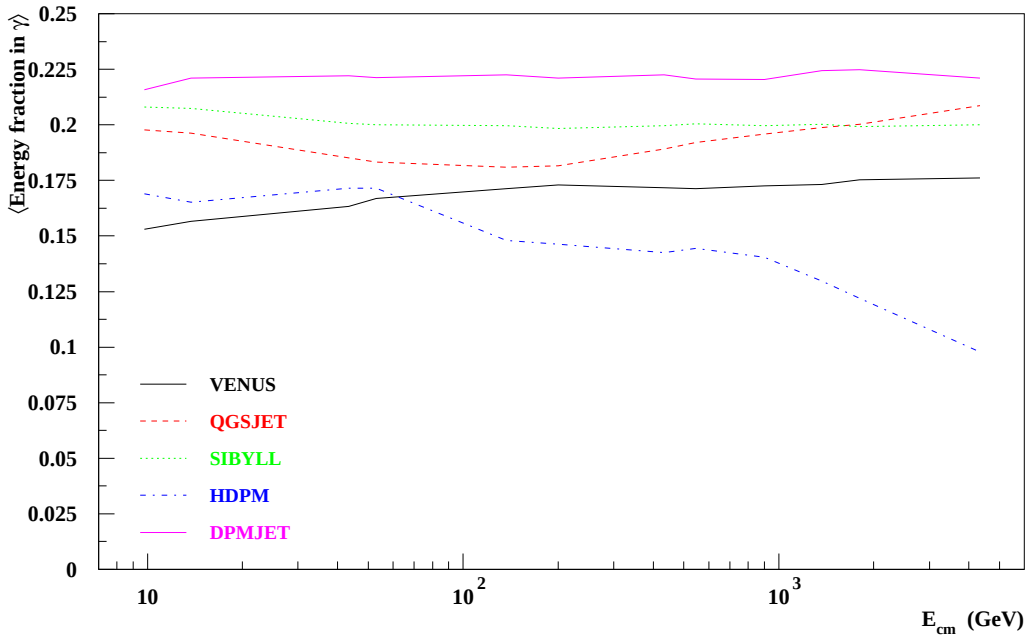

Figure 9: Average energy fraction going into photons from non-diffractive collisions of $\bar{p}$ on p as a function of the cm energy.

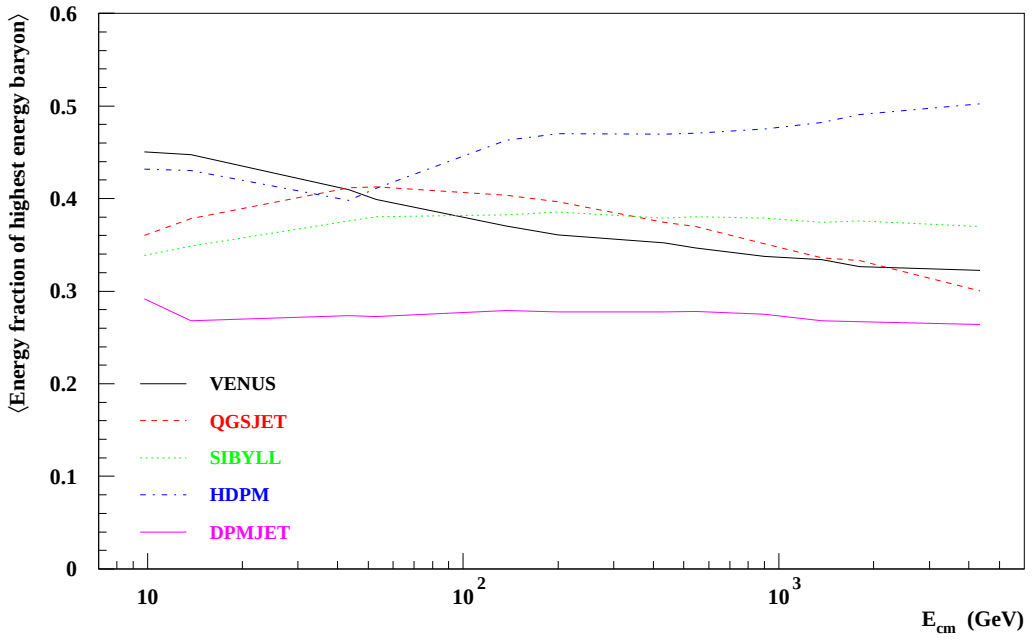

Figure 10: Average energy fraction of the highest energy baryon from non-diffractive collisions of $\bar{p}$ on p as a function of the cm energy.

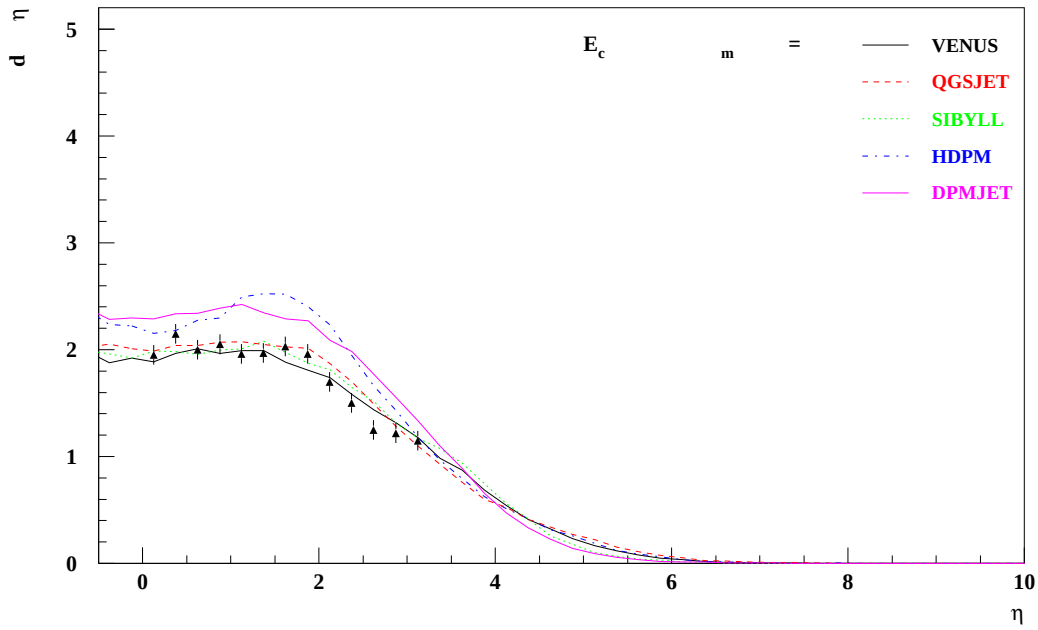

Figure 11: Pseudo rapidity distributions of charged particles from non-diffractive collisions of $\bar{p}$ on p at $E_{cm} = 53$ GeV. The triangles give experimental values from ref. [6].

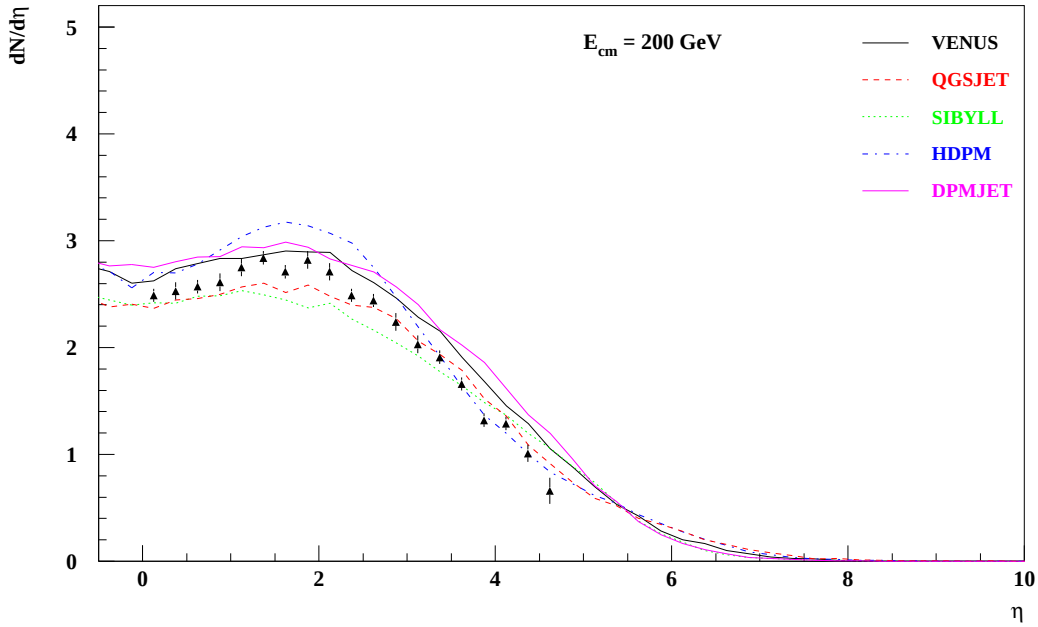

Figure 12: Pseudo rapidity distributions of charged particles from non-diffractive collisions of $\bar{p}$ on p at $E_{cm} = 200$ GeV. The triangles give experimental values from ref. [3].

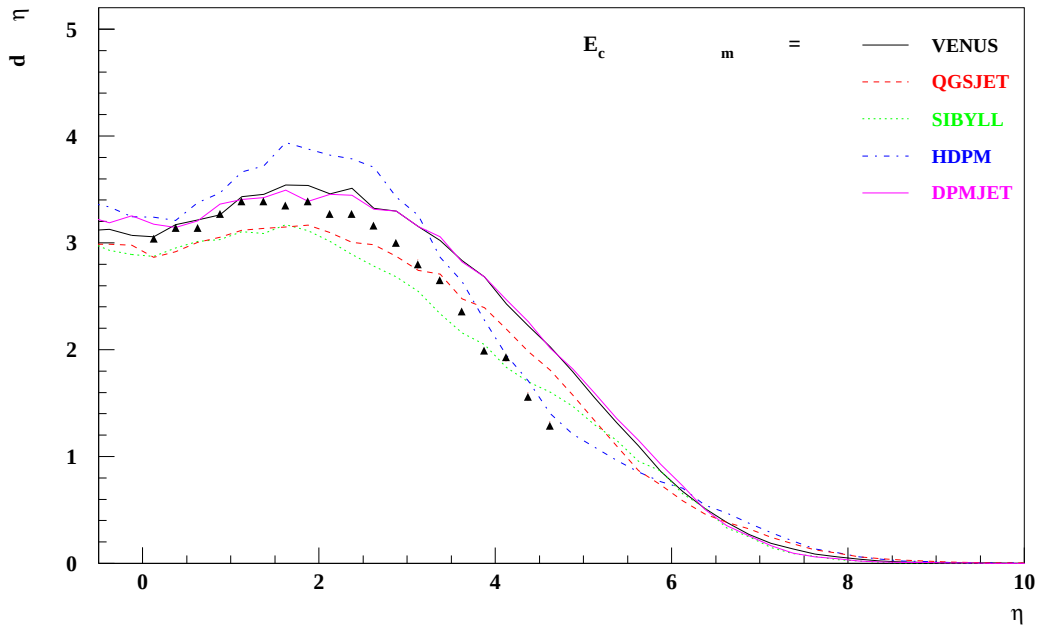

Figure 13: Pseudo rapidity distributions of charged particles from non-diffractive collisions of $\bar{p}$ on p at $E_{cm} = 540$ GeV. The triangles give experimental values from ref. [5].

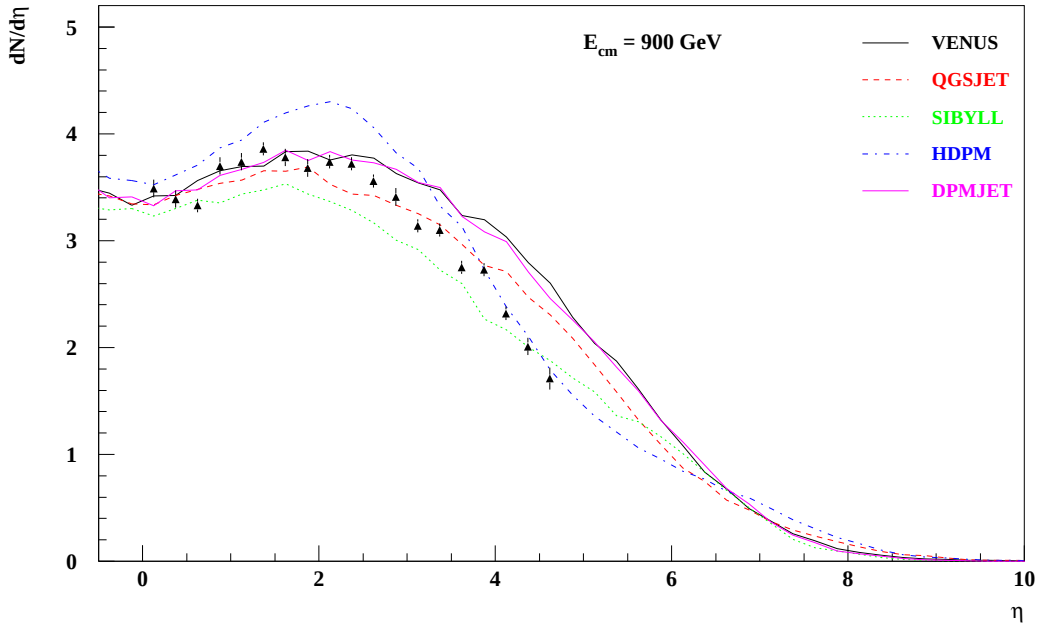

Figure 14: Pseudo rapidity distributions of charged particles from non-diffractive collisions of $\bar{p}$ on p at $E_{cm} = 900$ GeV. The triangles give experimental values from ref. [3].

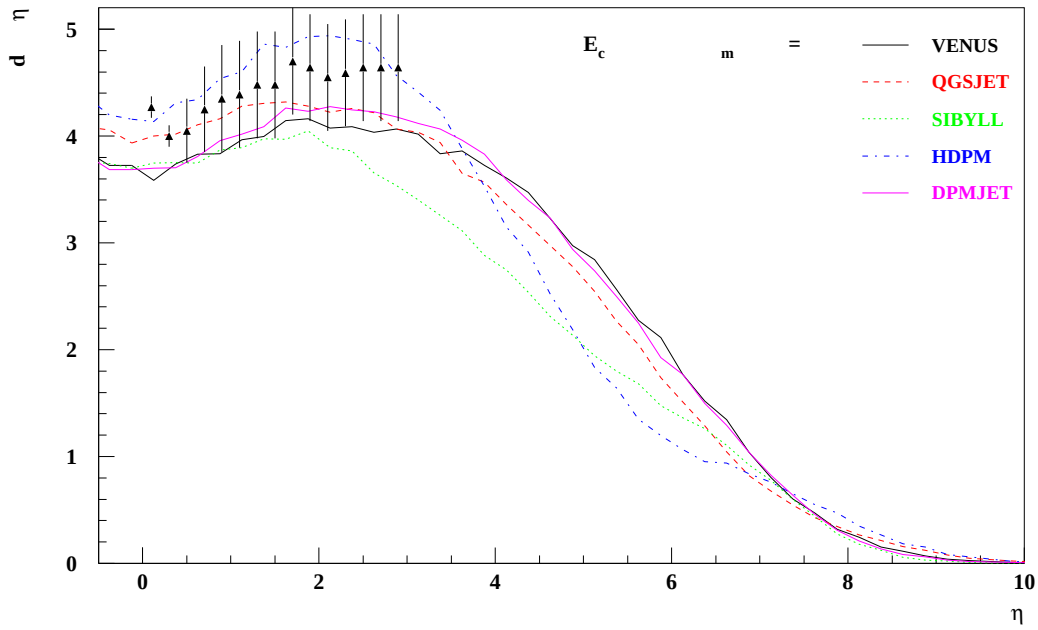

Figure 15: Pseudo rapidity distributions of charged particles from non-diffractive collisions of $\bar{p}$ on p at $E_{cm} = 1800$ GeV. The triangles give experimental values from ref. [1].

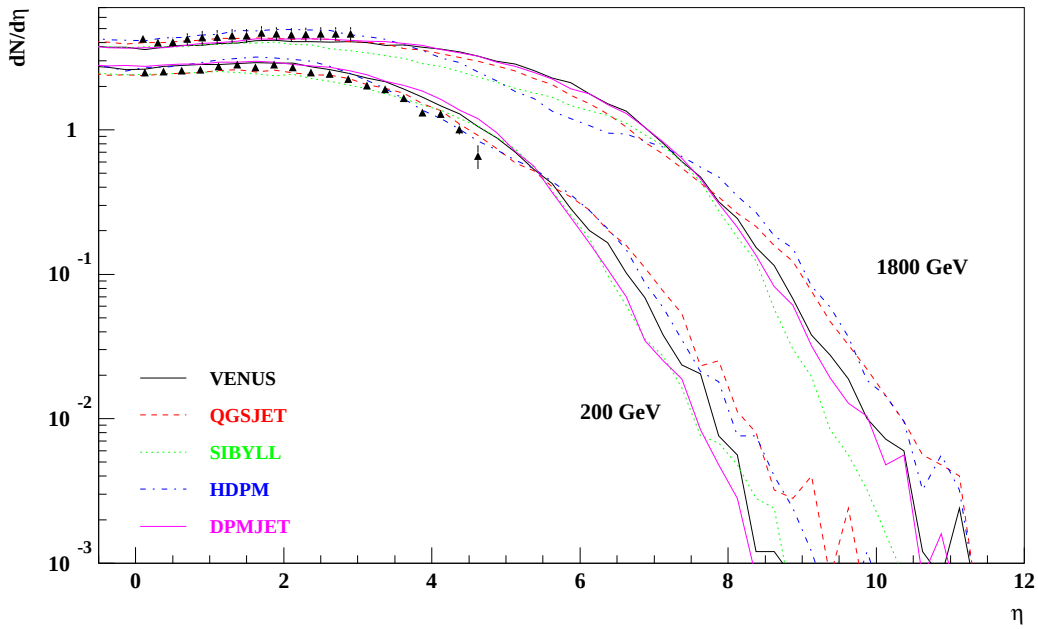

Figure 16: Pseudo rapidity distributions of charged particles from non-diffractive collisions of $\bar{p}$ on p at $E_{cm} = 200$ and 1800 GeV on a logarithmic $dN/d\eta$ scale. The triangles give experimental values from refs. [1, 3].

2.2 p-N Collisions

A more important reaction for air shower development is the p-N collision. For the model comparison we have used both diffractive and non-diffractive events in a mixture as given by the respective models. Again, we show the tables of average particle numbers (Tab. 7), energy flow into particle groups (Tab. 8), and the most energetic secondary particles (Tab. 9) for $E_{lab} = 10^{14}$, 10^{15}, and 10^{16} eV protons. VENUS produces the largest number of nucleons. This is due to the secondary interactions of strings before they hadronize (VENUS is the only model taking secondary interactions into account). Some of the target nucleons are not participants of the initial reaction but collide during the secondary interactions and, thus, get a small amount of energy and $p_\perp$ and are, consequently, no longer regarded as spectators. All models produce more photons than charged pions, indicating that not just decaying π^0 are responsible for the photons. The ratio $n_\gamma/n_{\pi^\pm}$ amounts to about 1.17 for VENUS, 1.20 for DPMJET and 1.35 for the other models. QGSJET shows the largest rise in particle numbers. At 10^{16} eV it produces more photons, pions, and kaons than the others.

In Tab. 8 the energy fraction going into the different secondary particles is tabulated for various energies. Here the leading particle effect gives rise to high energy p and n. Apart from this the situation is very similar to the $\bar{p}$-p case. HDPM puts least and DPMJET most energy into pions. Positive pions receive more energy than negative ones because they have the same charge as the projectile particle.

Tab. 9 shows the distribution of the highest energy particles. The numbers are very similar to the numbers of the $\bar{p}$-p reactions. In p-N collisions p and n are the most energetic particles in about 2/3 of the cases. Exceptions are HDPM with 85% and DPMJET with 50 to 55%. DPMJET more often has antinucleons as the highest energy particle (6% versus 2 to 3%) and more pions than the others. Only at 10^{16} eV has QGSJET more pions than DPMJET. HDPM shows by far the smallest number of highest energy pions and photons very similar to the situation in $\bar{p}$-p collisions. VENUS has more pions than HDPM but clearly less than the other models. All the models show a slightly increasing fraction of kaons as highest energy particles with about 8 to 9% for VENUS, 4% for HDPM and the other models in between.

In Figs. 17 to 19 the Feynman x_F distributions for $E_{lab} = 10^{14}$, 10^{15}, and 10^{16} eV are shown as for the $\bar{p}$-p case. Here the secondary interactions in VENUS lead to the high part of the x_F distributions at the target side. Diffractive events are included and are visible as peaks at $x_F \approx 1$. The heights of these peaks seem to agree quite well. In the forward part of these distributions ($0.4 < x_F < 0.95$), however, the models differ by factors of about 5 to 10 depending on energy. DPMJET exhibits much lower baryon distributions at $x_F = 0.7 \ldots 0.95$ than the other models. Furthermore, it shows together with SIBYLL and HDPM a much sharper diffraction peak than VENUS and QGSJET.

The x_F distributions for photons and mesons agree better. VENUS still shows some excess in backward directions due to the secondary interactions. In forward directions SIBYLL and DPMJET are slightly higher than the other models.

In Fig. 20 charged multiplicity distributions are presented. QGSJET, DPMJET, and SIBYLL exhibit peaks at very small multiplicities (diffractive events) well separated from the broad distribution of the non-diffractive events. This feature is due to the fact that these models have no or few non-diffractive events with small multiplicities (see Fig. 3). For the other models the distributions overlap and diffractive events tend to have higher multiplicities as well. The multiplicity distributions extend to much higher values than in $\bar{p}$-p collisions. Still SIBYLL and DPMJET have smaller fluctuations in the number of secondaries than the other models. In Fig. 21 the average charged multiplicity is shown as a function of energy, being roughly two times larger than in the $\bar{p}$-p collision. The energy shown at the x-axis is the center of mass energy of the incoming p with one nucleon of the target. The models agree with each other within about 10%, apart from SIBYLL, which is 30% lower for cm energies above 100 GeV.

In Fig. 22 the $p_\perp$ distributions for 10^{15} eV protons on nitrogen nuclei are shown. HDPM exhibits a higher density at $p_\perp > 1$ GeV/c as in the $\bar{p}$-p collisions. The other models agree more or less with each other. The change of $\langle p_\perp \rangle$ with the energy is shown in Fig. 23. VENUS is low for higher energies, QGSJET is low for lower energies. The other models agree with each other on the level of 10%. Compared to the $\langle p_\perp \rangle$ plot for $\bar{p}$-p reactions (Fig. 7) VENUS appears to have 10% larger values for all energies and HDPM gives the same $\langle p_\perp \rangle$ at low energies but a 10% higher value at $E_{cm} = 4 \times 10^4$ GeV. The other models yield unchanged $\langle p_\perp \rangle$ with energies.

Fig. 24 gives the energy fraction going into photons as a function of energy. The picture is almost identical to Fig. 9 with DPMJET showing the largest and VENUS showing the lowest fraction, being almost constant with energy. The values are 0.15 to 0.22 with a spread of about 0.04. HDPM is the only model changing with energy and dropping by 40% to about 0.1 only. All models give practically the same values for $\bar{p}$-p and p-N reactions apart from DPMJET whose electromagnetic inelasticity is about 10% smaller for p-N than for $\bar{p}$-p reactions at $E_{cm} \approx 10 \ldots 100$ GeV. At higher energies the difference reduces to about 5%.

Elasticity as a function of energy is represented in Fig. 25. All models but HDPM show a slight decrease with energy. DPMJET is the lowest one of the decreasing models with elasticities from 0.35 to 0.25 and SIBYLL is the highest with values from 0.4 to 0.36. HDPM changes from 0.4 at low energies to 0.5 at high energies. The functions look very much like the ones for $\bar{p}$-p reactions. VENUS and DPMJET differ at low energies only.

Fig. 26 shows the average number of target nucleons hit by the incident proton as a function of cm energy and Fig. 27 gives the distribution of it for collisions at $E_0 = 10^{15}$ eV. The differences in the average values (about 25 to 40%) originate from the different shapes of the tails of the distributions. These reflect different assumptions on the nuclear densities of projectile and target nuclei. Usually, the measured charge density is taken (e.g. in VENUS and QGSJET). In the HDPM model a density is adopted that has been obtained by unfolding the finite charge distribution of the proton. Since the charge diameter of the proton is about 1.6 fm, this results in a smaller and, hence, denser nucleus. As a consequence, the calculated number of projectile or target nucleons participating in the collision is larger. We should like to point out that we consider the HDPM procedure more realistic. QGSJET obviously contains projectile diffraction events which do not affect the target at all and, thus, lead to zero interacting target nucleons.

$E_0 = 10^{14}$ eV					
	VENUS	QGSJET	SIBYLL	HDPM	DPMJET
p	4.6 ± 2.9	2.5 ± 1.9	1.9 ± 1.2	3.1 ± 2.1	2.7 ± 1.7
$\bar{p}$	1.4 ± 1.5	1.0 ± 1.3	0.5 ± 0.7	1.3 ± 1.5	1.1 ± 1.2
n	4.2 ± 2.9	2.2 ± 1.9	1.5 ± 1.3	2.5 ± 2.0	2.3 ± 1.7
$\bar{n}$	1.3 ± 1.4	1.0 ± 1.3	0.5 ± 0.7	1.2 ± 1.4	1.0 ± 1.2
γ	44.9 ± 33.4	45.5 ± 39.9	37.8 ± 27.0	47.8 ± 36.3	46.3 ± 31.5
π^-	19.4 ± 14.0	17.0 ± 15.0	13.9 ± 9.8	18.2 ± 14.1	19.1 ± 12.9
π^+	19.4 ± 13.8	17.2 ± 15.0	14.2 ± 9.8	18.5 ± 14.1	19.3 ± 12.9
K^{0L}	2.2 ± 2.4	1.9 ± 2.0	1.4 ± 1.6	1.7 ± 1.7	1.9 ± 2.0
K^{0S}	2.2 ± 2.4	2.0 ± 2.1	1.4 ± 1.6	1.7 ± 1.7	1.9 ± 2.0
K^-	2.2 ± 2.3	1.8 ± 2.0	1.3 ± 1.5	1.7 ± 1.8	1.8 ± 1.9
K^+	2.5 ± 2.5	2.0 ± 2.1	1.5 ± 1.5	1.7 ± 1.8	2.0 ± 1.9
$E_0 = 10^{15}$ eV					
	VENUS	QGSJET	SIBYLL	HDPM	DPMJET
p	5.4 ± 3.5	3.4 ± 2.8	2.3 ± 1.5	4.3 ± 3.1	3.3 ± 2.1
$\bar{p}$	2.2 ± 2.2	1.9 ± 2.1	0.8 ± 1.1	2.4 ± 2.5	1.7 ± 1.7
n	4.9 ± 3.4	3.0 ± 2.6	1.9 ± 1.6	3.5 ± 3.0	3.0 ± 2.1
$\bar{n}$	2.0 ± 2.0	1.7 ± 2.0	0.8 ± 1.0	2.3 ± 2.4	1.6 ± 1.6
γ	66.9 ± 51.1	73.3 ± 68.2	59.7 ± 44.5	75.8 ± 62.2	70.0 ± 46.6
π^-	28.8 ± 21.2	27.3 ± 25.5	22.0 ± 16.2	27.4 ± 22.8	29.1 ± 19.2
π^+	28.7 ± 21.0	27.4 ± 25.4	22.2 ± 16.2	27.6 ± 22.9	29.4 ± 19.2
K^{0L}	3.4 ± 3.4	3.2 ± 3.4	2.4 ± 2.4	2.9 ± 2.8	2.9 ± 2.7
K^{0S}	3.5 ± 3.4	3.4 ± 3.4	2.3 ± 2.4	2.9 ± 2.8	2.9 ± 2.7
K^-	3.4 ± 3.4	3.2 ± 3.4	2.3 ± 2.2	3.0 ± 3.0	2.9 ± 2.6
K^+	3.8 ± 3.6	3.4 ± 3.5	2.4 ± 2.3	3.0 ± 3.0	3.1 ± 2.7
$E_0 = 10^{16}$ eV					
	VENUS	QGSJET	SIBYLL	HDPM	DPMJET
p	6.7 ± 4.5	4.9 ± 4.3	2.9 ± 2.0	6.3 ± 5.0	4.1 ± 2.6
$\bar{p}$	3.4 ± 3.1	3.3 ± 3.5	1.3 ± 1.5	4.3 ± 4.4	2.4 ± 2.2
n	6.1 ± 4.2	4.3 ± 4.0	2.5 ± 2.1	5.5 ± 4.9	3.7 ± 2.6
$\bar{n}$	3.1 ± 2.9	3.0 ± 3.3	1.3 ± 1.5	4.2 ± 4.3	2.3 ± 2.1
γ	99.9 ± 79.0	120.3 ±118.9	94.1 ± 72.6	113.3 ±101.5	98.2 ± 65.2
π^-	42.5 ± 32.5	44.8 ± 44.6	34.7 ± 26.6	41.3 ± 37.4	41.0 ± 27.1
π^+	42.3 ± 32.3	44.9 ± 44.5	34.9 ± 26.5	41.5 ± 37.4	41.2 ± 27.0
K^{0L}	5.3 ± 5.0	5.5 ± 5.8	3.8 ± 3.6	5.0 ± 4.9	4.1 ± 3.5
K^{0S}	5.3 ± 5.0	5.7 ± 5.9	3.8 ± 3.6	5.0 ± 4.9	4.1 ± 3.6
K^-	5.3 ± 5.0	5.6 ± 5.8	3.8 ± 3.5	5.1 ± 5.1	4.1 ± 3.5
K^+	5.8 ± 5.3	5.7 ± 5.9	4.0 ± 3.6	5.1 ± 5.1	4.3 ± 3.5

Table 7: Average numbers of secondary particles and variances in collisions of 10^{14}, 10^{15}, and 10^{16} eV p on N.

$E_0 = 10^{14}$ eV					
	VENUS	QGSJET	SIBYLL	HDPM	DPMJET
p	25.46	25.50	31.08	36.36	22.13
n	12.96	13.78	10.04	11.70	9.59
$\bar{p}$	1.91	1.22	1.08	1.72	2.16
$\bar{n}$	1.64	1.22	1.11	1.60	2.13
γ	16.97	19.01	19.19	14.84	20.93
π^-	14.01	14.56	13.47	11.75	15.92
π^+	16.30	16.03	16.71	14.98	18.17
K^{0L}	2.60	1.99	1.83	1.68	2.24
K^{0S}	2.58	2.34	1.81	1.74	2.09
K^-	2.18	1.82	1.54	1.79	2.11
K^+	3.26	2.37	2.01	1.74	2.36
$E_0 = 10^{15}$ eV					
	VENUS	QGSJET	SIBYLL	HDPM	DPMJET
p	24.70	23.23	29.40	41.09	19.69
n	12.40	12.64	9.66	9.44	9.22
$\bar{p}$	1.88	1.30	1.07	1.97	2.32
$\bar{n}$	1.76	1.34	1.18	1.83	2.13
γ	16.98	20.15	19.78	13.21	21.57
π^-	14.62	15.25	14.06	10.41	16.88
π^+	16.46	16.83	17.04	14.68	18.73
K^{0L}	2.76	2.11	1.96	1.70	2.32
K^{0S}	2.65	2.52	1.99	1.83	2.23
K^-	2.30	2.01	1.67	1.83	2.27
K^+	3.33	2.47	2.06	1.91	2.46
$E_0 = 10^{16}$ eV					
	VENUS	QGSJET	SIBYLL	HDPM	DPMJET
p	22.95	20.93	28.08	42.81	18.81
n	12.01	11.68	8.98	10.28	8.45
$\bar{p}$	1.97	1.45	1.14	2.27	2.45
$\bar{n}$	1.86	1.39	1.20	2.10	2.28
γ	17.71	21.00	20.23	10.32	21.68
π^-	14.89	16.18	14.69	10.04	17.28
π^+	16.64	17.60	17.52	14.14	19.20
K^{0L}	2.89	2.20	2.00	2.03	2.30
K^{0S}	2.96	2.60	2.06	1.98	2.37
K^-	2.39	2.12	1.83	1.91	2.30
K^+	3.61	2.70	2.15	2.05	2.69

Table 8: Energy fraction going into secondary particles (in %) in collisions of 10^{14}, 10^{15}, and 10^{16} eV p on N.

$E_0 = 10^{14}$ eV					
	VENUS	QGSJET	SIBYLL	HDPM	DPMJET
p	42.84	41.14	50.63	62.10	36.22
$\bar{p}$	1.48	0.66	0.97	0.96	3.00
n	25.23	24.86	17.72	19.43	18.28
$\bar{n}$	1.26	0.66	1.04	1.02	2.96
γ	5.21	7.26	6.93	2.57	8.23
π^-	6.80	9.57	7.35	5.13	10.76
π^+	8.87	11.00	10.64	4.70	12.66
K^{0L}	1.92	1.26	1.31	1.10	2.14
K^{0S}	2.09	1.17	1.30	0.96	1.69
K^-	1.30	1.15	0.85	1.01	1.95
K^+	2.98	1.23	1.23	1.02	2.09
$E_0 = 10^{15}$ eV					
	VENUS	QGSJET	SIBYLL	HDPM	DPMJET
p	42.97	36.33	49.42	68.72	33.34
$\bar{p}$	1.51	0.82	0.83	1.17	2.92
n	25.00	21.65	17.49	15.48	17.78
$\bar{n}$	1.29	1.03	1.16	0.99	2.86
γ	4.76	9.20	7.27	1.80	9.33
π^-	7.34	12.00	8.06	3.92	11.91
π^+	8.95	13.17	10.81	4.08	13.44
K^{0L}	2.13	1.27	1.31	0.68	2.21
K^{0S}	1.93	1.51	1.48	1.04	1.93
K^-	1.54	1.33	0.87	1.00	1.98
K^+	2.53	1.65	1.24	1.11	2.22
$E_0 = 10^{16}$ eV					
	VENUS	QGSJET	SIBYLL	HDPM	DPMJET
p	40.64	31.70	49.19	68.65	32.70
$\bar{p}$	1.59	1.00	0.99	1.33	3.52
n	25.44	18.85	16.73	15.57	16.38
$\bar{n}$	1.32	1.00	1.21	1.14	3.13
γ	5.22	9.90	7.41	1.12	9.03
π^-	7.73	14.46	8.75	4.27	11.99
π^+	9.32	15.67	10.70	3.71	14.34
K^{0L}	2.24	1.60	1.30	1.15	2.12
K^{0S}	2.24	1.85	1.49	1.08	2.21
K^-	1.28	1.67	0.98	0.89	1.92
K^+	2.96	2.20	1.21	1.09	2.59

Table 9: Most energetic secondary particles (in %) in collisions of 10^{14}, 10^{15}, and 10^{16} eV p on N.

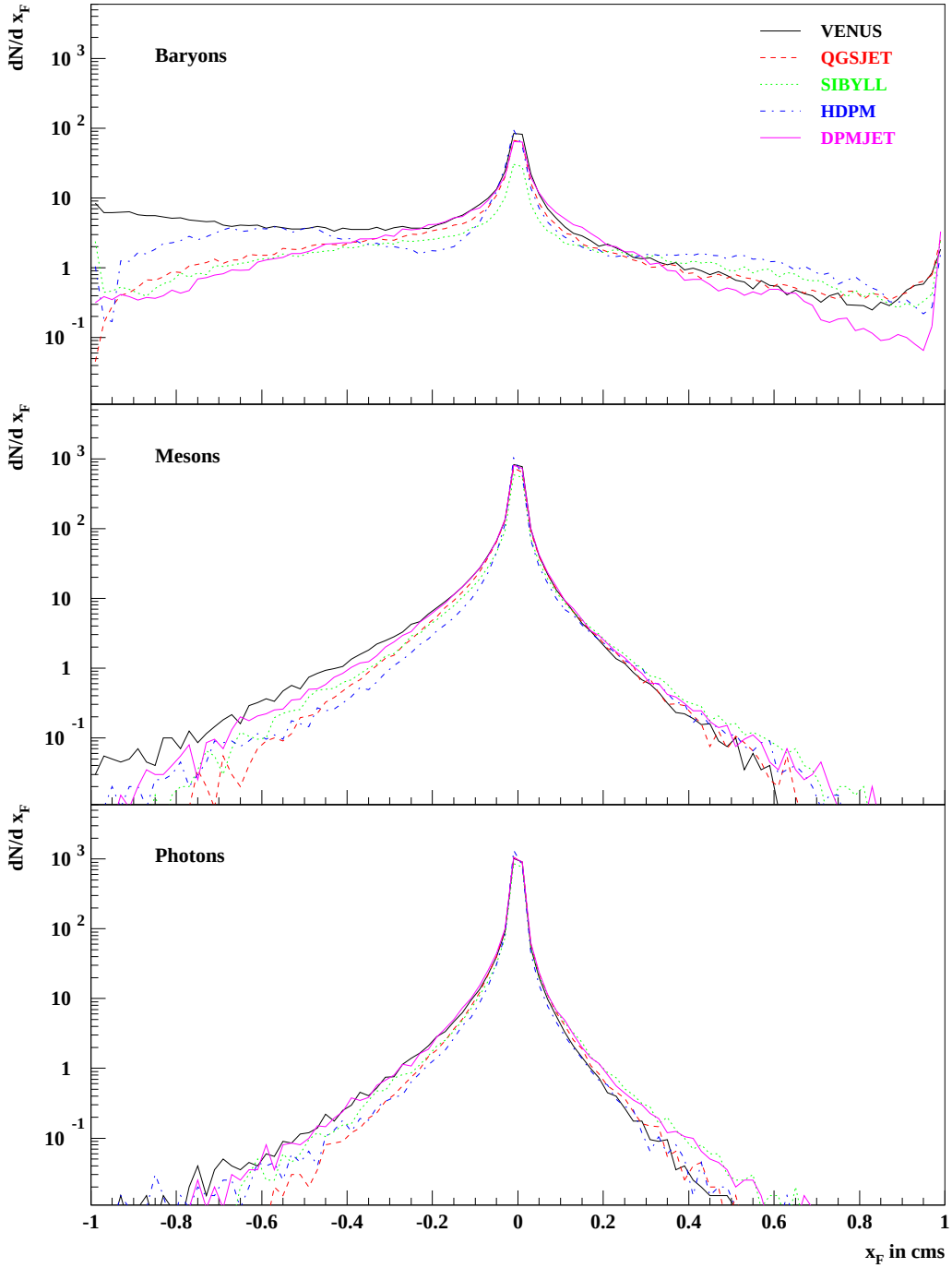

Figure 17: Feynman x_F distributions for baryons, mesons, and photons from collisions of 10^{14} eV p on N.

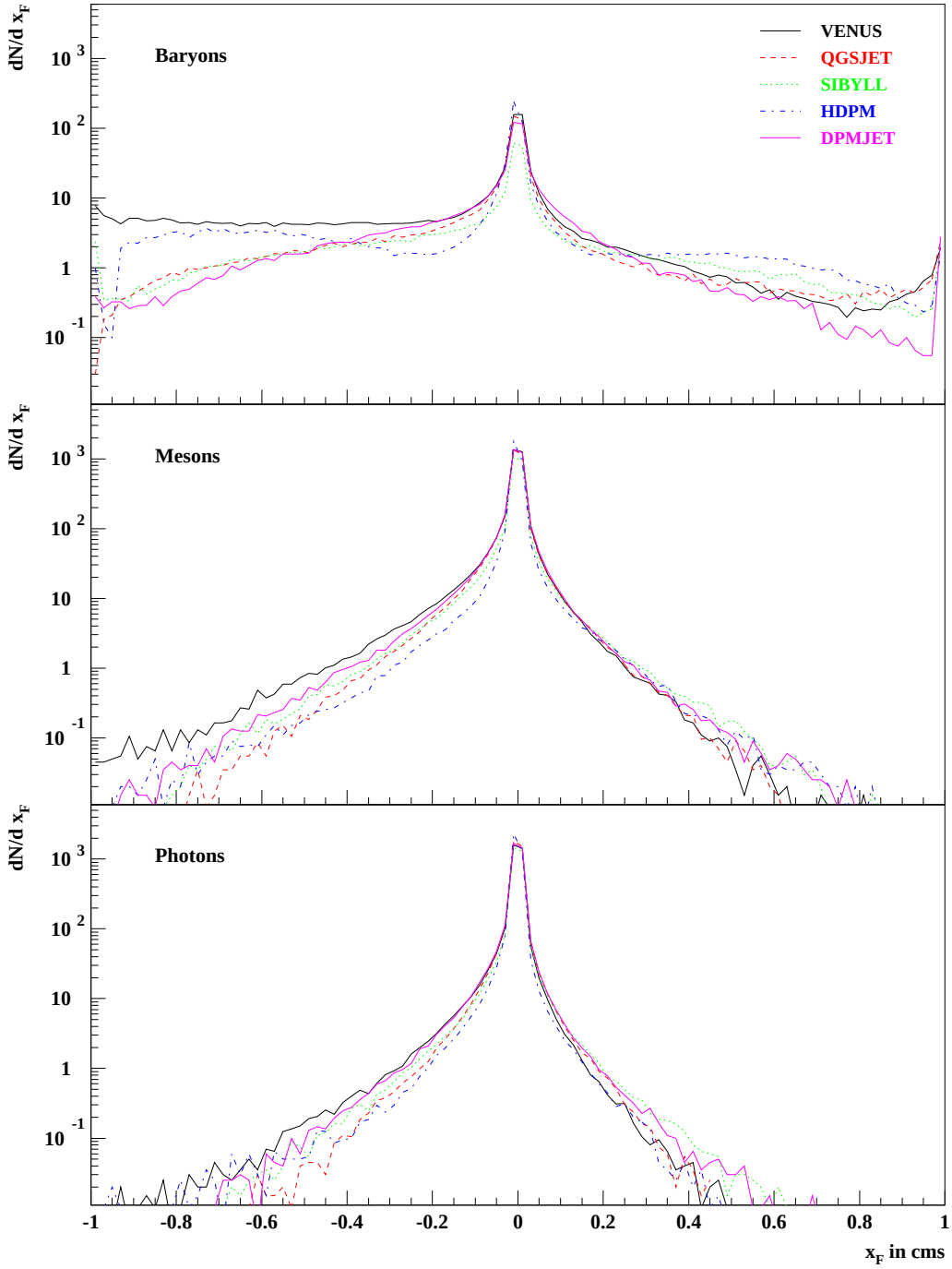

Figure 18: Feynman x_F distributions for baryons, mesons, and photons from collisions of 10^{15} eV p on N.

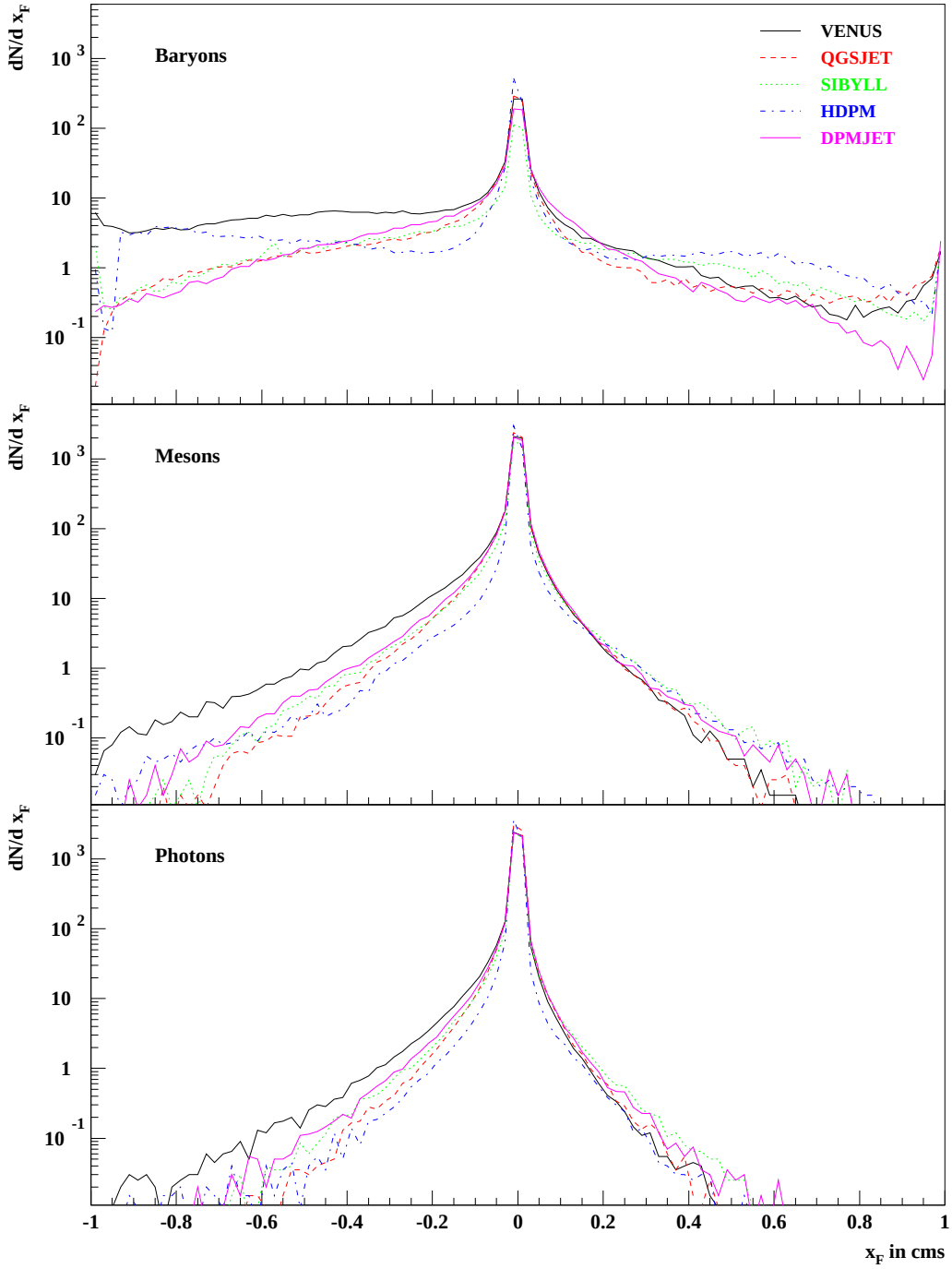

Figure 19: Feynman x_F distributions for baryons, mesons, and photons from collisions of 10^{16} eV p on N.

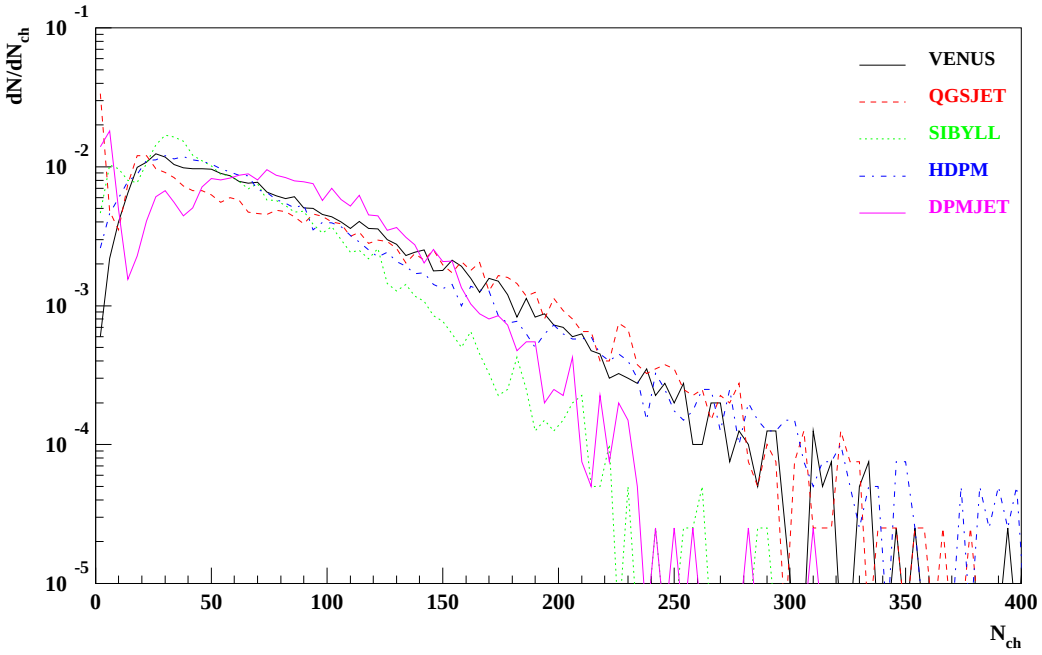

Figure 20: Multiplicity distributions of charged particles from collisions of 10^{15} eV p on N.

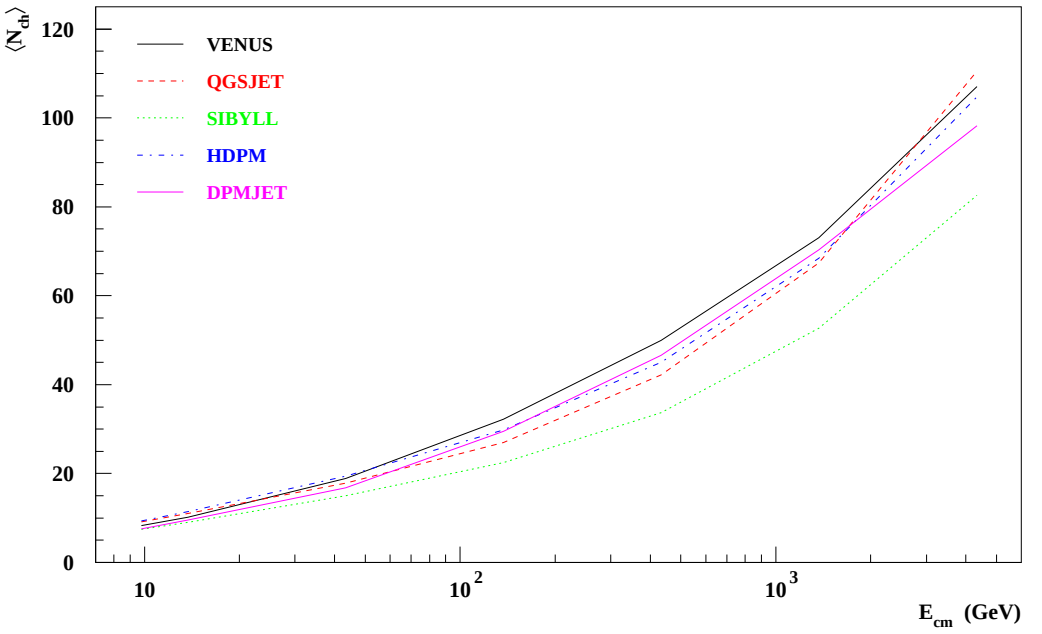

Figure 21: Average charged multiplicities from collisions of p on N as a function of the cm energy.

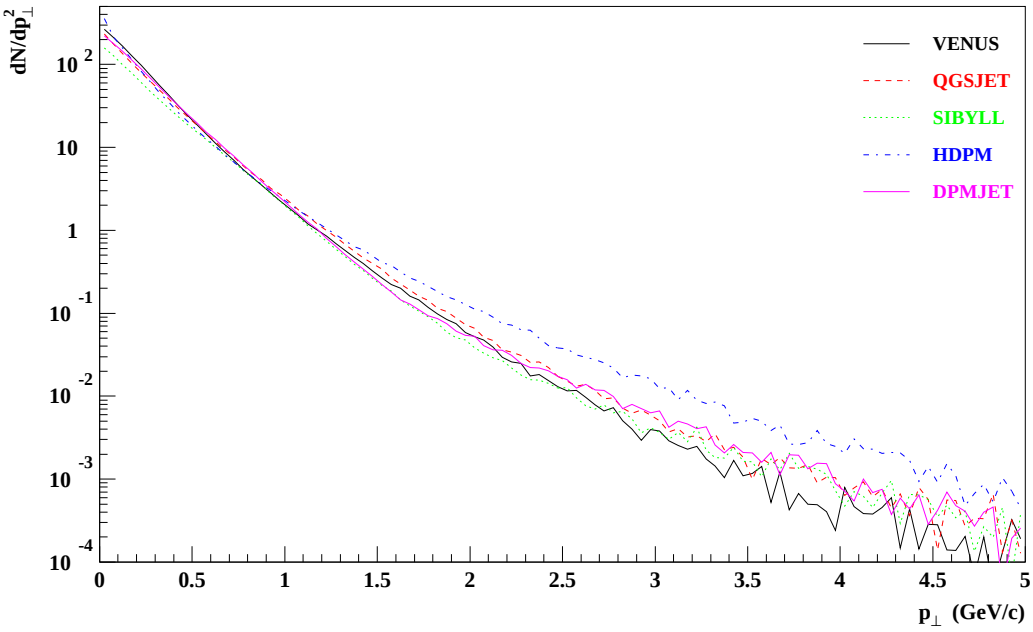

Figure 22: Transverse momentum distributions of charged particles from collisions of 10^{15} eV p on N.

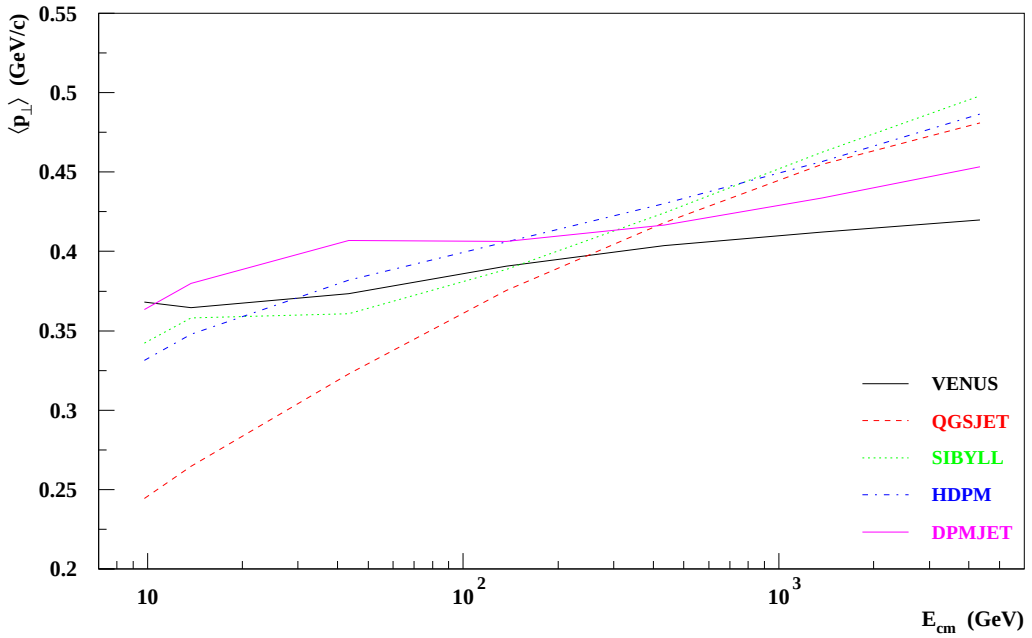

Figure 23: Average transverse momenta of charged particles from collisions of p on N as a function of the cm energy.

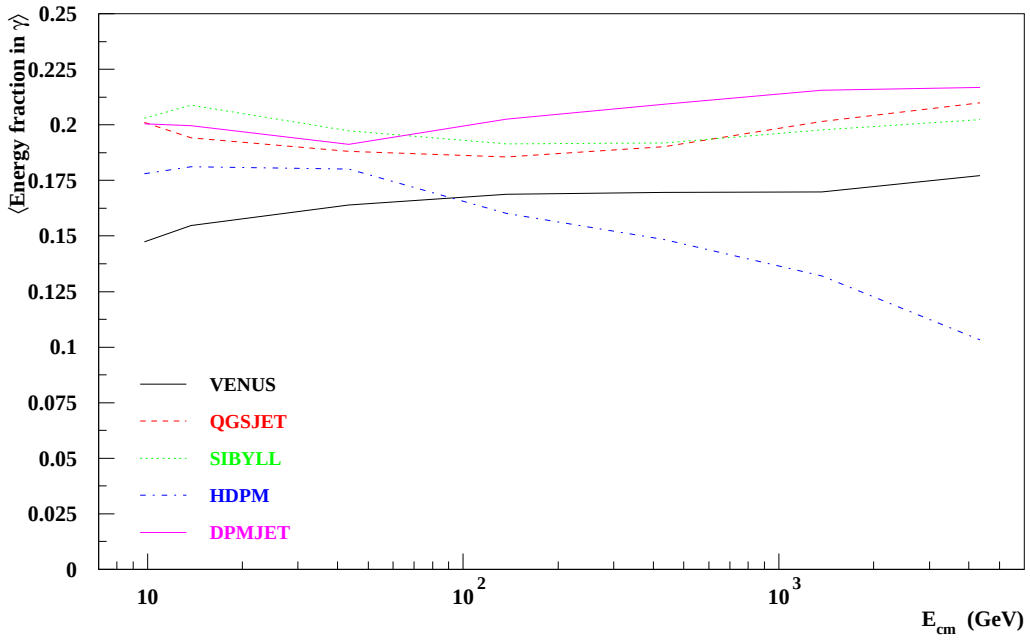

Figure 24: Average energy fraction going into photons from collisions of p on N as a function of the cm energy.

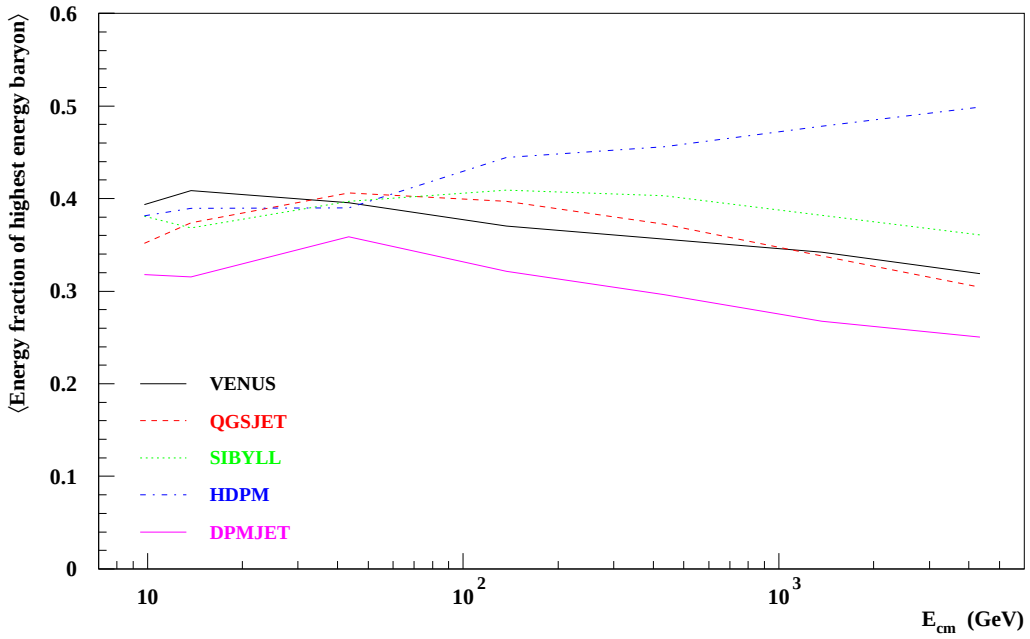

Figure 25: Average energy fraction of the highest energy baryon from collisions of p on N as a function of the cm energy.

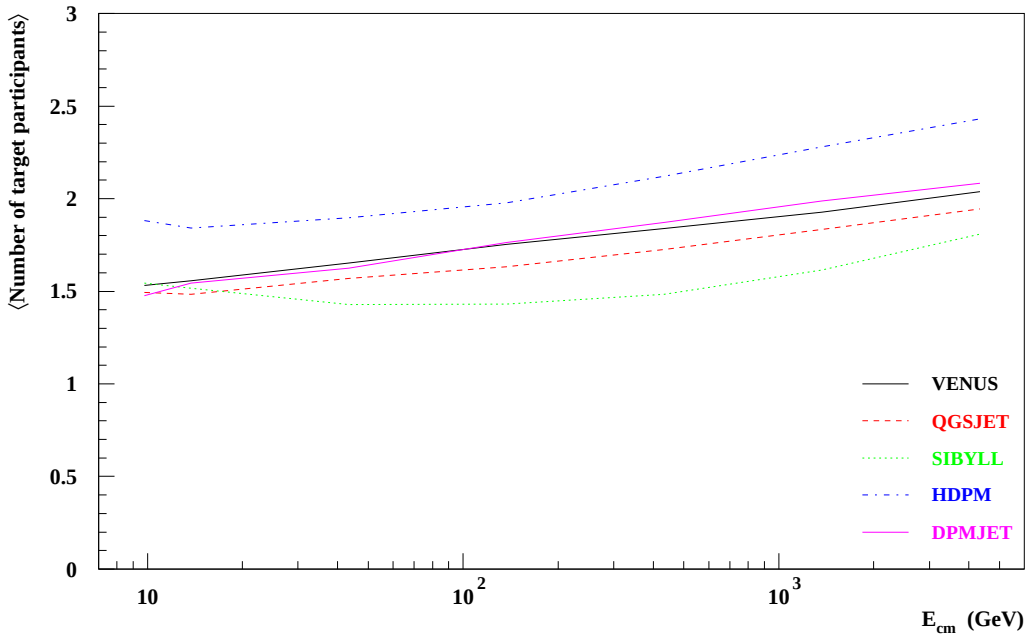

Figure 26: Average numbers of interacting target nucleons in collisions of p on N as a function of the cm energy.

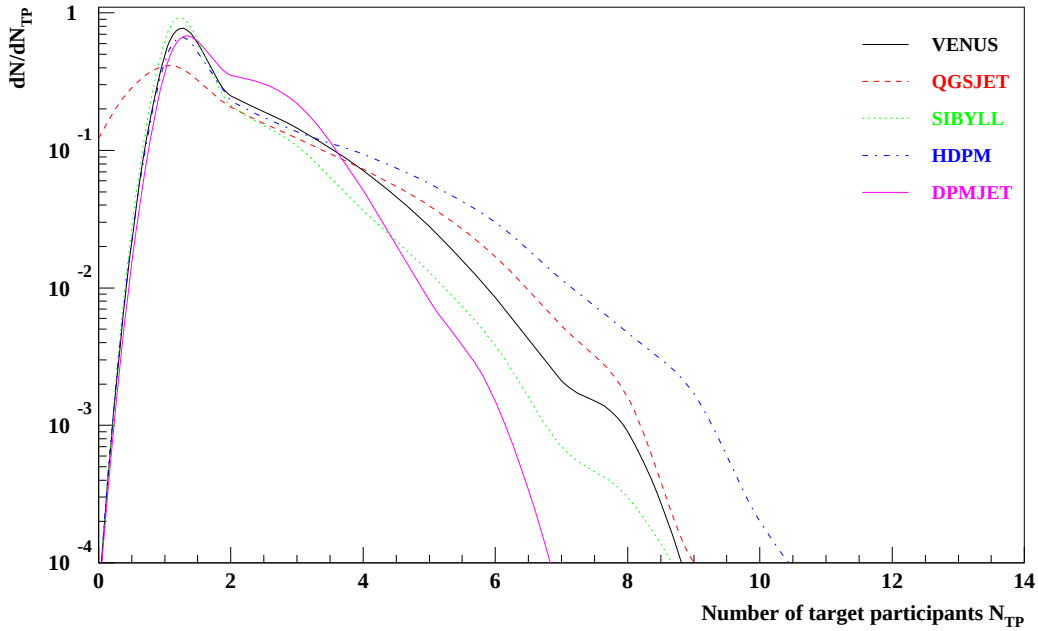

Figure 27: Distributions of the number of interacting target nucleons in collisions of 10^{15} eV p on N.

2.3 π^+-N Collisions

In an air shower many pions are produced, mainly at energies much lower than the primary energy. Therefore, we present some results on collisions of 10^{13} eV positive pions on nitrogen.

Tab. 10 gives the average number of secondary particles produced at this energy. Mostly pions are produced. The agreement between the models is quite good. VENUS produces most baryons and kaons and QGSJET more photons. Again, SIBYLL produces less particles and exhibits smaller fluctuations than all the other models.

In Tab. 11 the energy fraction going into various secondary particles is shown. Since π^+ are the projectiles, the energy fraction in pions is much larger than in the $\bar{p}$-p and p-N case. Between 80 and 90% of the energy goes to pions. Nucleons and antinucleons receive clearly less energy than kaons.

The most energetic particle is presented in Tab. 12, being, of course, the π^+ in about 45%. HDPM generates the highest fraction with 55% and DPMJET the lowest with 42%. DPMJET produces the largest fraction of highest energy baryons (15%) and VENUS has most highest energy kaons (17%).

Fig. 28 shows the Feynman x_F distributions of baryons, photons, and mesons emerging from collisions of 10^{13} eV pions on nitrogen. On the target side the effect of the secondary interactions in VENUS is clearly visible. Much more baryons are produced. On the projectile side VENUS is below the other models and none of the models gives an indication of diffractive events in the baryon distribution, as expected. Since the projectile is a meson, the meson distribution shows higher densities in the forward direction due to diffraction. Again, the VENUS curve is above QGSJET, DPMJET, and SIBYLL at $x_F \approx 0.9$ and shows a smoother rise to the diffractive peak than all other models.

The distribution of charged multiplicity as presented in Fig. 29 resembles very much the distributions shown in Fig. 20. SIBYLL and DPMJET show the smallest fluctuations and SIBYLL has the smallest mean values, as can also be seen from Fig. 30 where the average multiplicities are plotted versus the cm energy. E_{cm} is the center of mass energy of the incoming pion with one nucleon of the target. In the figure the rise of multiplicity due to mini-jet production in QGSJET is evident at about $E_{cm} > 1000$ GeV. QGSJET gives a higher multiplicity than in the p-N case, whereas all other programs give about 10% fewer particles than for the p-N collisions. SIBYLL stays below the others by 30% and no indication of a strong rise due to mini-jets can be seen.

The $p_\perp$ distribution (Fig. 31) is hardest for HDPM and the average $p_\perp$ as a function of energy (Fig. 32) looks much like the plots for $\bar{p}$-p and p-N reactions (Figs. 7 and 23) with VENUS being low at high energies and QGSJET at low energies. There is not much difference to Fig. 23, only the values for VENUS are lower by about 7%.

The fraction of energy going into photons as a function of energy (see Fig. 33) is larger than in $\bar{p}$-p and p-N collisions. The reason is that π^0s can be formed more easily as leading particles and, thus, more energy is transformed into photons. The models predict fractions between 0.25 (VENUS, DPMJET) and 0.30 (SIBYLL and QGSJET). HDPM gives a decrease to 0.2 for high energies. It is interesting to see that DPMJET yields lower values than SIBYLL and QGSJET, whereas it was the opposite in $\bar{p}$-p and p-N interactions (see Figs. 9 and 24).

Fig. 34 presents the energy fraction of the highest energy meson which is the elasticity in case of the incoming particle being a pion. All models but HDPM show a slight decrease with energy. The values are smaller by 10 to 20% than in the p-N case for all models except for DPMJET, which gives almost identical elasticities.

$E_0 = 10^{13}$ eV					
	VENUS	QGSJET	SIBYLL	HDPM	DPMJET
p	3.1 ± 2.4	1.2 ± 1.2	1.0 ± 0.9	1.4 ± 1.3	1.4 ± 1.2
$\bar{p}$	0.7 ± 0.9	0.5 ± 0.7	0.3 ± 0.5	0.6 ± 0.8	0.6 ± 0.8
n	3.0 ± 2.4	1.1 ± 1.2	0.8 ± 0.9	1.3 ± 1.2	1.3 ± 1.2
$\bar{n}$	0.6 ± 0.8	0.5 ± 0.7	0.3 ± 0.5	0.5 ± 0.8	0.6 ± 0.8
γ	24.1 ± 17.2	27.2 ± 21.5	23.3 ± 14.9	26.5 ± 17.0	26.2 ± 18.5
π^-	10.3 ± 7.2	10.1 ± 8.0	8.2 ± 5.3	10.9 ± 7.5	10.6 ± 7.5
π^+	11.1 ± 7.0	11.0 ± 8.0	9.2 ± 5.2	11.9 ± 7.5	11.4 ± 7.5
K^{0L}	1.2 ± 1.4	1.0 ± 1.2	0.8 ± 1.0	0.8 ± 0.9	1.0 ± 1.3
K^{0S}	1.1 ± 1.4	1.0 ± 1.2	0.7 ± 1.0	0.8 ± 0.9	1.0 ± 1.3
K^-	1.1 ± 1.3	0.9 ± 1.2	0.7 ± 0.9	0.9 ± 1.1	1.0 ± 1.2
K^+	1.3 ± 1.4	1.0 ± 1.2	0.8 ± 1.0	0.9 ± 1.1	1.1 ± 1.3

Table 10: Average numbers of secondary particles and variances in collisions of 10^{13} eV π^+ on N.

$E_0 = 10^{13}$ eV					
	VENUS	QGSJET	SIBYLL	HDPM	DPMJET
p	1.78	1.65	1.63	1.42	2.50
n	1.52	1.34	1.03	1.40	2.09
$\bar{p}$	1.80	1.24	0.97	1.47	2.05
$\bar{n}$	1.80	1.39	1.69	1.28	2.75
γ	25.20	29.65	30.39	28.19	25.70
π^-	15.30	18.73	15.52	16.75	16.55
π^+	39.17	36.60	37.42	43.10	37.31
K^{0L}	3.47	2.45	2.75	1.45	2.76
K^{0S}	3.38	2.11	2.78	1.37	2.68
K^-	2.99	2.15	2.07	1.64	2.59
K^+	3.37	2.45	3.53	1.69	2.82

Table 11: Energy fraction going into secondary particles (in %) in collisions of 10^{13} eV π^+ on N.

Fig. 35 shows the average number of target nucleons hit by the incident pion as a function of cm energy and Fig. 36 gives its distribution for collisions at $E_0 = 10^{13}$ eV. The differences in the average values amount to about 20% and originate, as in the p-N case, from the differently shaped tails of the distributions which are due to different assumptions on the nuclear density profiles of the target nucleus.

$E_0 = 10^{13}$ eV					
	VENUS	QGSJET	SIBYLL	HDPM	DPMJET
p	1.31	1.91	1.74	1.00	3.49
$\bar{p}$	1.43	1.10	0.87	1.17	2.85
n	1.01	1.45	0.69	1.37	2.70
$\bar{n}$	1.62	1.34	2.15	1.11	4.31
γ	19.85	22.42	23.57	23.95	18.20
π^-	12.61	19.19	13.12	12.34	14.42
π^+	45.19	43.94	45.60	54.87	41.55
K^{0L}	4.68	2.44	3.00	1.06	3.22
K^{0S}	4.60	1.88	2.94	0.89	3.05
K^-	3.48	1.93	1.80	1.04	2.83
K^+	4.12	2.27	4.36	1.01	3.31

Table 12: Most energetic secondary particles (in %) in collisions of 10^{13} eV π^+ on N.

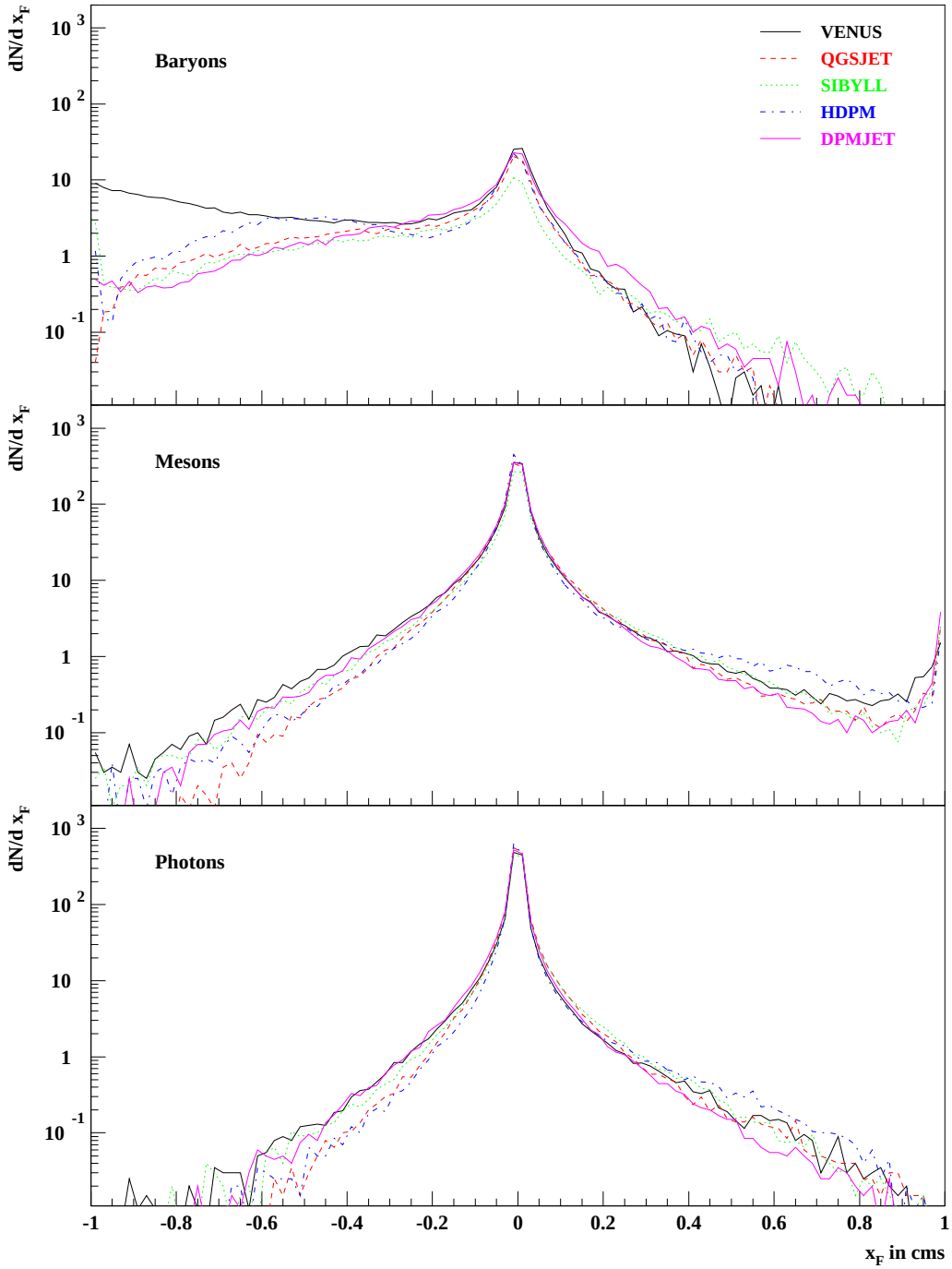

Figure 28: Feynman x_F distributions for baryons, mesons, and photons from collisions of 10^{13} eV π^+ on N.

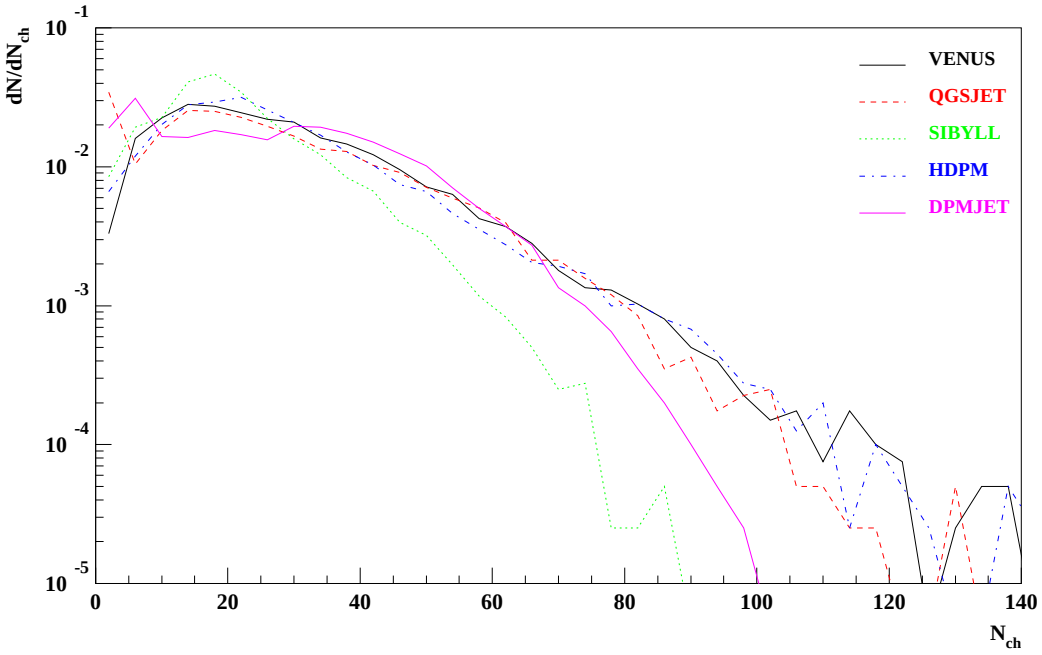

Figure 29: Multiplicity distributions of charged particles from collisions of 10^{13} eV π^+ on N.

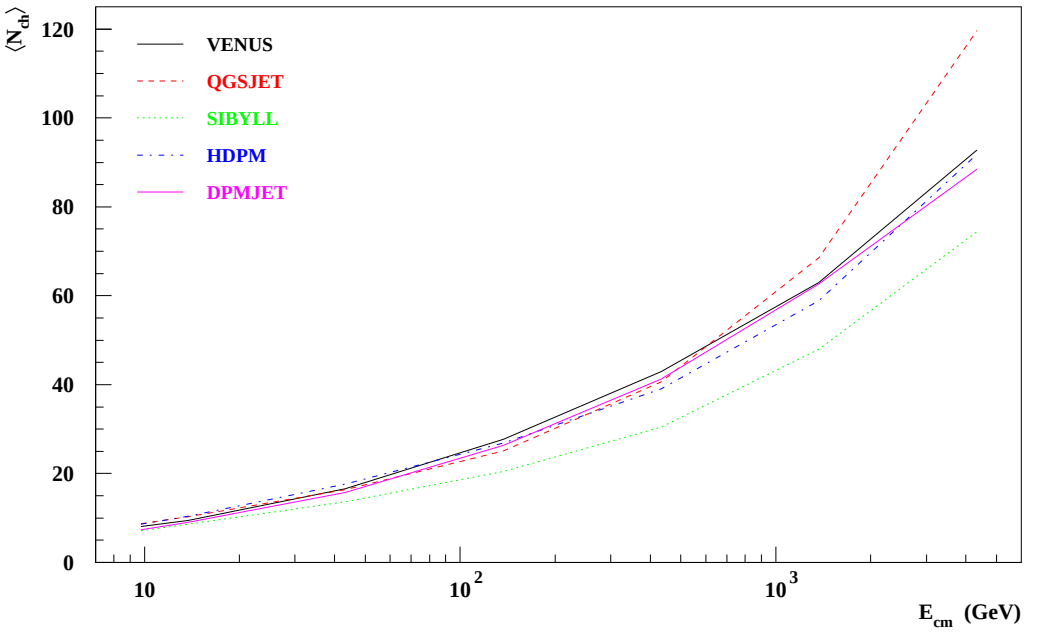

Figure 30: Average charged multiplicities from collisions of π^+ on N as a function of the cm energy.

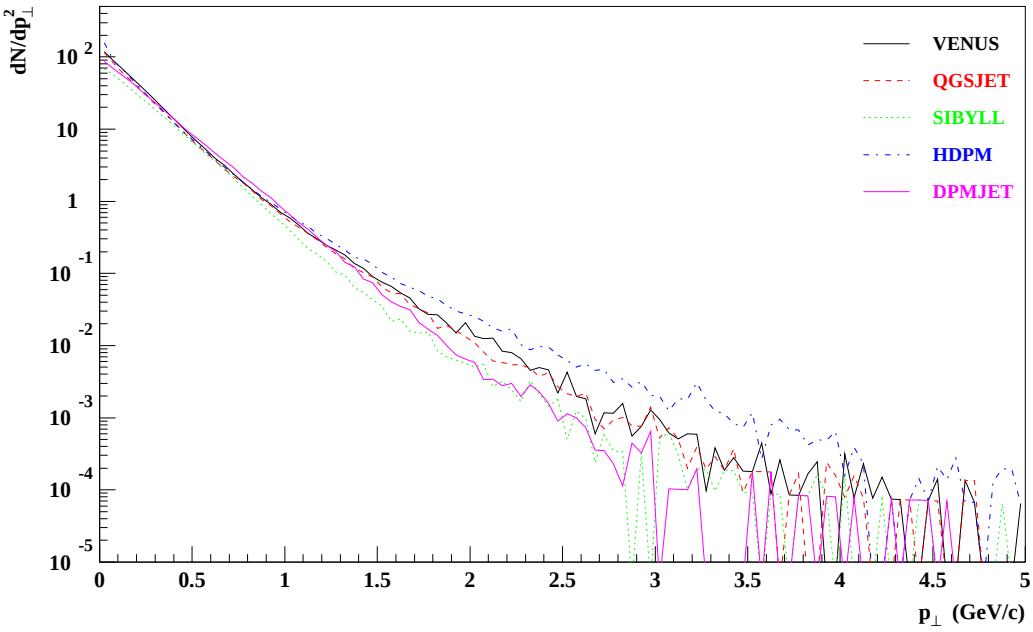

Figure 31: Transverse momentum distributions of charged particles from collisions of 10^{13} eV π^+ on N.

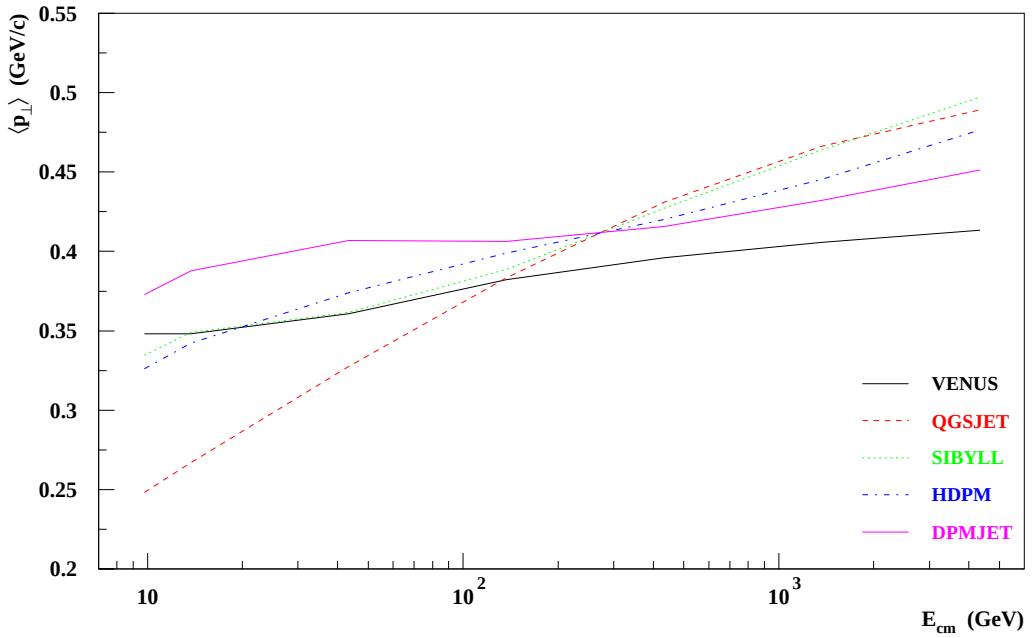

Figure 32: Average transverse momenta of charged particles from collisions of π^+ on N as a function of the cm energy.

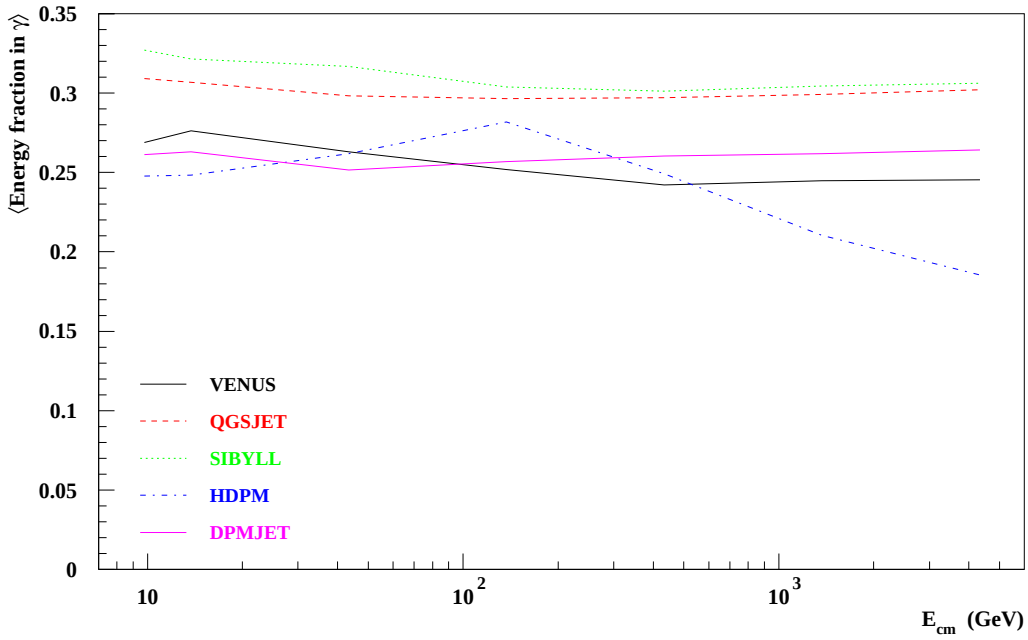

Figure 33: Average energy fraction going into photons from collisions of π^+ on N as a function of the cm energy.

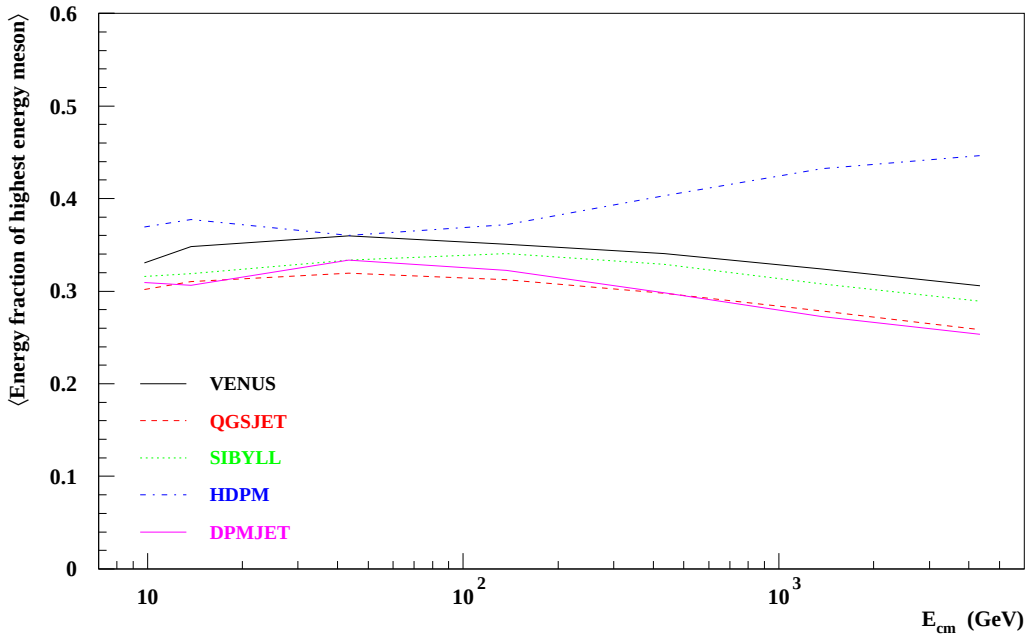

Figure 34: Average energy fraction of the highest energy meson from collisions of π^+ on N as a function of the cm energy.

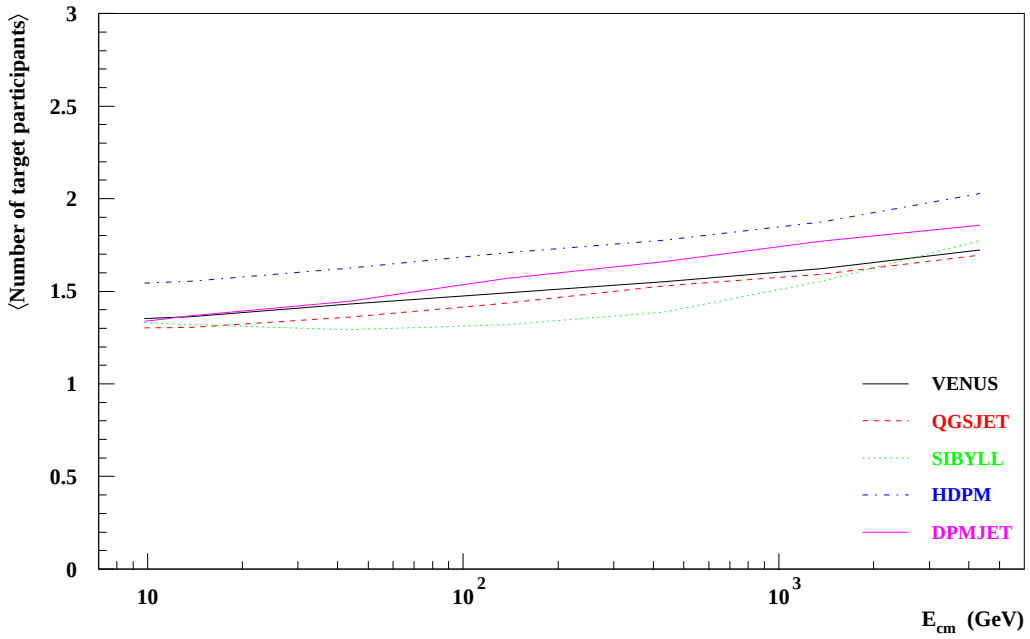

Figure 35: Average numbers of interacting target nucleons in collisions of π^+ on N as a function of the cm energy.

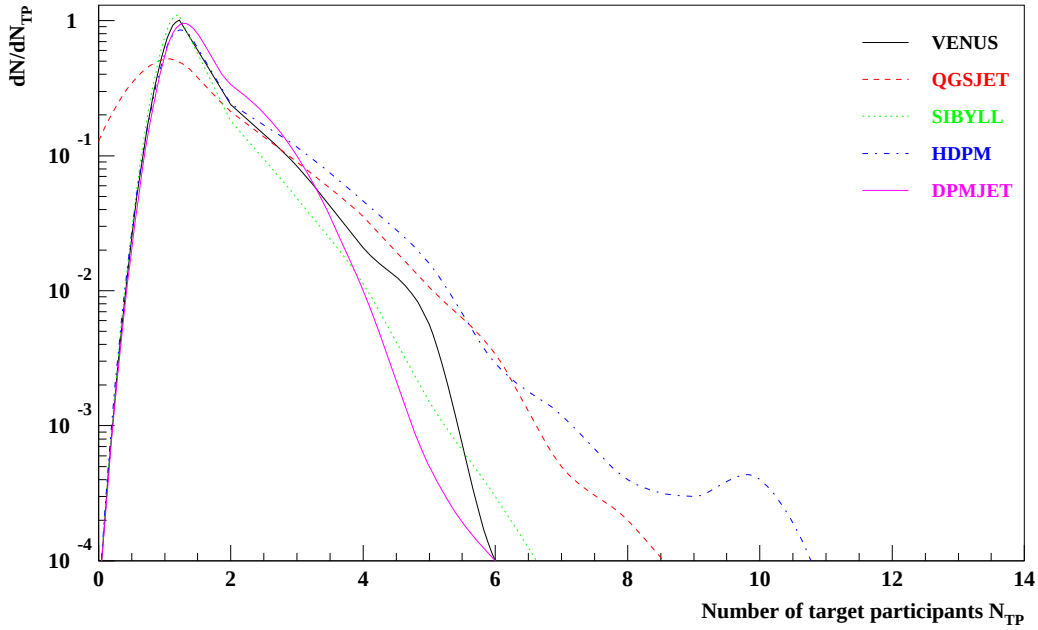

Figure 36: Distributions of the number of interacting target nucleons in collisions of 10^{15} eV π^+ on N.

2.4 Fe-N Collisions

We investigate nucleus-nucleus collisions with an iron nucleus as primary particle. Tab. 13 gives the average particle numbers produced in diffractive and non-diffractive Fe-N collisions at 10^{15} eV. HDPM produces 70 to 90% more photons and pions than all other models. The number of baryons and kaons is higher as well. SIBYLL no longer has less particles than the other models. The reason for the results of HDPM and SIBYLL is that the particle production is overestimated when using the simple superposition model for nucleus-nucleus collisions. A Fe-N collision is modeled by several p-N collisions which all produce more particles in the target region than in the projectile region. Therefore, the Fe-N collision generates, with these models, more particles in the backward region even though the projectile is larger than the target. The number of photons and pions of the other models agrees within 10 and 20%, respectively. VENUS produces two times more nucleons than QGSJET and still 60% more than DPMJET and more kaons than the others (apart from HDPM).

In Tab. 14 the energy fraction going into the different secondary particles is listed. The energy of the spectator nucleons is given in the last line. Since the projectile is a nucleus a major part (81 to 85%) of the energy remains with the spectator nucleons and does not contribute to particle production. In VENUS there are nucleons that undergo secondary interactions with not much energy and momentum exchange, transferring some of the spectator nucleons to secondary particles. Therefore, the VENUS numbers show a drastically lower energy fraction for spectators and a higher one for the nucleons. The models (except for VENUS) give 5 to 8% of their energy to nucleons and 4.5 to 6% to pions, 3 to 4% to photons and 1 to 3% to kaons, very much with the same pattern as for $\bar{p}$-p and p-N reactions.

The highest energy secondary generated with VENUS is a nucleon in 94% of the interactions. QGSJET and HDPM give similar numbers, as can be inferred from Tab. 15. SIBYLL predicts only 85% and DPMJET 71% for this number. DPMJET generates most pions (18%), photons (4%), and kaons (5%) as the highest energy particle.

The Feynman x_F distributions for baryons (Fig. 37) exhibit considerable differences. VENUS, due to the secondary interactions, produces more baryons than QGSJET and DPMJET both in forward and backward directions. The differences are 1 to 2 orders of magnitude. The distributions of VENUS, QGSJET, and DPMJET are asymmetric with more particles in the forward direction as one would expect with a Fe projectile on a N target. HDPM and SIBYLL are asymmetric as well, but with more particles in the backward region and with more baryons than VENUS in the target region. The wrong asymmetry and the particle excess are due to the superposition model, but since these are particles with a small laboratory energy this has not much influence on shower development.

The Feynman x_F distributions of photons and mesons are differing and show different asymmetries as well. VENUS exhibits most photons and mesons with $x_F \approx 1$ and QGSJET yields less by more than an order of magnitude. At the target side HDPM and SIBYLL are dominating.

In Fig. 38 the multiplicity distribution is shown for charged particles in Fe-N reactions at 10^{15} eV. There are events with more than 1000 charged secondaries. HDPM even reaches 1600 and more, due to the superposition model. For SIBYLL the increasing effect of the superposition model and the small intrinsic multiplicity compensate each other. This leads to a distribution similar to the ones of VENUS, QGSJET, or DPMJET.

The average charged multiplicity is displayed in Fig. 39. E_{cm} is taken as the center of mass energy of one nucleon in the projectile with one nucleon in the target and therefore reaches not as high values as in the $\bar{p}$-p or the p-N case. Here QGSJET is lowest, being 25% below VENUS. HDPM is conspicuously much higher than the other models, in clear contrast to the situation for p-N collisions (cf. Fig. 21). (The kink in the HDPM curve in Fig. 39 at $E_{cm} = 200$ GeV is a computational

artifact and the highest point should not been taken seriously.) We attribute this difference to different assumptions on nuclear density which lead to higher numbers of interacting nucleons (cf. Fig. 27 in section 2.2). This is reflected by Figs. 44 and 45 as well.

The $p_\perp$ distribution for 10^{15} eV Fe-N collisions of Fig. 40 again shows the higher multiplicity predicted by HDPM. The HDPM line lies two times higher than the other ones. VENUS and HDPM have a flatter distribution than the other models, which coincide quite well. $\langle p_\perp \rangle$ as a function of E_{cm} is shown in Fig. 41. Whereas the HDPM and SIBYLL curves match perfectly with the corresponding lines of Fig. 23, QGSJET and DPMJET lie 5 to 10% below the values for p-N collisions and VENUS is higher by the same amount.

In Fig. 42 the energy fraction going into photons is plotted as a function of energy. The fraction is calculated as the energy sum in photons divided by the energy of the projectile. In the VENUS model we have projectile nucleons that do not participate in the initial interaction, but lose a little energy and acquire some transverse momentum during the secondary interactions. Therefore, these nucleons are no longer counted as spectators and increase the energy sum of protons and neutrons considerably. Consequently, the energy fraction of the spectators is diminished by the same amount. The other models do not include secondary interactions and, therefore, have a higher energy fraction for spectators and a lower one for protons and neutrons. Since the spectators do not participate in the interaction, the numerical value of k_γ is much smaller than in the $\bar{p}$-p or the p-N case. DPMJET and QGSJET are the models with the highest and lowest k_γ value, respectively. They differ by about 40%. HDPM has a decreasing k_γ with energy, whereas all other models show a slight rise.

In Fig. 43 the energy fraction going into the highest energy secondary baryon is presented as a function of energy. Projectile spectators are not taken into account. Since in VENUS some of the spectators are identified as collision products due to secondary interactions, the energy fraction of the highest energy baryon is higher by a factor of 2 than for the other models. The spread amongst the other models amounts to about 40% and there is no energy dependence.

For nucleus-nucleus collisions it is interesting to plot the number of interacting projectile and target nucleons as a function of energy (see Figs. 44 and 46). The number of interacting projectile nucleons is calculated for all models according to Glauber calculations and, hence, should not vary much. HDPM, however, gives a 40% larger average number of interacting projectile nucleons than the other models. As mentioned above when discussing the multiplicity (see Fig. 38), we attribute this difference to different assumptions concerning the nuclear density distribution. The superposition models leads to an overestimation of the number of interacting target nucleons which in case of HDPM and SIBYLL results in numbers larger than 14, the total number of nucleons in the nitrogen target. Each target nucleon hit by n projectile nucleons, for instance, is counted n times in the HDPM model.

The distributions of the number of participating nucleons are shown in Figs. 45 and 47 for projectile and target, respectively. SIBYLL describes the distribution of the number of projectile nucleons to be in agreement with the GRT models, whereas it gives numbers of interacting target nucleons up to 70. For HDPM even 100 interacting target nucleons occur. The GRT models agree more or less with each other. DPMJET, for some funny reasons, never has 13 interacting target nucleons.

$E_0 = 10^{15}$ eV					
	VENUS	QGSJET	SIBYLL	HDPM	DPMJET
p	23.1 ± 16.2	10.9 ± 9.5	15.4 ± 15.7	29.2 ± 28.9	14.3 ± 10.8
$\bar{p}$	6.8 ± 7.0	4.0 ± 4.1	2.8 ± 3.3	9.8 ± 10.2	5.8 ± 5.0
n	23.4 ± 16.1	10.3 ± 9.1	11.6 ± 12.0	29.0 ± 28.5	14.1 ± 10.7
$\bar{n}$	6.1 ± 6.3	3.7 ± 3.9	2.9 ± 3.3	9.1 ± 9.4	5.5 ± 4.8
γ	246.0 ± 248.8	225.2 ± 218.1	240.5 ± 246.7	432.9 ± 425.9	249.6 ± 188.1
π^-	104.1 ± 103.1	87.5 ± 85.1	88.2 ± 90.3	173.5 ± 171.1	104.5 ± 78.7
π^+	101.6 ± 101.0	86.8 ± 84.5	90.3 ± 92.4	173.1 ± 170.8	103.5 ± 77.9
K^{0L}	13.5 ± 14.6	7.9 ± 7.9	8.3 ± 9.0	13.5 ± 13.7	10.3 ± 8.5
K^{0S}	13.6 ± 14.7	8.6 ± 8.4	8.3 ± 9.0	13.5 ± 13.7	10.3 ± 8.7
K^-	13.2 ± 14.4	8.0 ± 7.9	7.9 ± 8.6	14.5 ± 14.8	10.1 ± 8.4
K^+	15.3 ± 16.3	8.6 ± 8.4	9.0 ± 9.6	14.5 ± 14.8	10.9 ± 8.9

Table 13: Average numbers of secondary particles and variances in collisions of 10^{15} eV Fe on N.

$E_0 = 10^{15}$ eV					
	VENUS	QGSJET	SIBYLL	HDPM	DPMJET
p	15.28	3.01	5.19	3.75	2.43
n	16.95	2.98	1.65	4.04	2.45
$\bar{p}$	0.37	0.16	0.16	0.36	0.31
$\bar{n}$	0.33	0.15	0.18	0.34	0.30
γ	3.51	2.87	3.10	3.39	4.22
π^-	3.14	2.36	2.18	2.87	3.55
π^+	2.92	2.32	2.68	2.88	3.49
K^{0L}	0.67	0.26	0.29	0.36	0.44
K^{0S}	0.67	0.34	0.29	0.36	0.43
K^-	0.51	0.26	0.23	0.40	0.37
K^+	0.88	0.33	0.32	0.40	0.49
Spectators	54.77	84.98	83.74	80.85	81.53

Table 14: Energy fraction going into secondary particles (in %) in collisions of 10^{15} eV Fe on N.

$E_0 = 10^{15}$ eV					
	VENUS	QGSJET	SIBYLL	HDPM	DPMJET
p	44.51	46.14	74.44	40.30	35.81
$\bar{p}$	0.22	0.18	0.37	0.23	0.70
n	49.09	46.58	10.90	54.22	35.32
$\bar{n}$	0.31	0.10	0.62	0.27	0.62
γ	0.87	1.32	2.05	0.92	4.26
π^-	1.54	2.34	2.86	1.45	9.23
π^+	1.37	2.37	3.52	1.53	9.16
K^{0L}	0.61	0.29	0.21	0.20	1.46
K^{0S}	0.56	0.22	0.39	0.27	1.12
K^-	0.34	0.13	0.12	0.28	0.57
K^+	0.58	0.32	0.43	0.33	1.71

Table 15: Most energetic secondary particles (in %) in collisions of 10^{15} eV Fe on N.

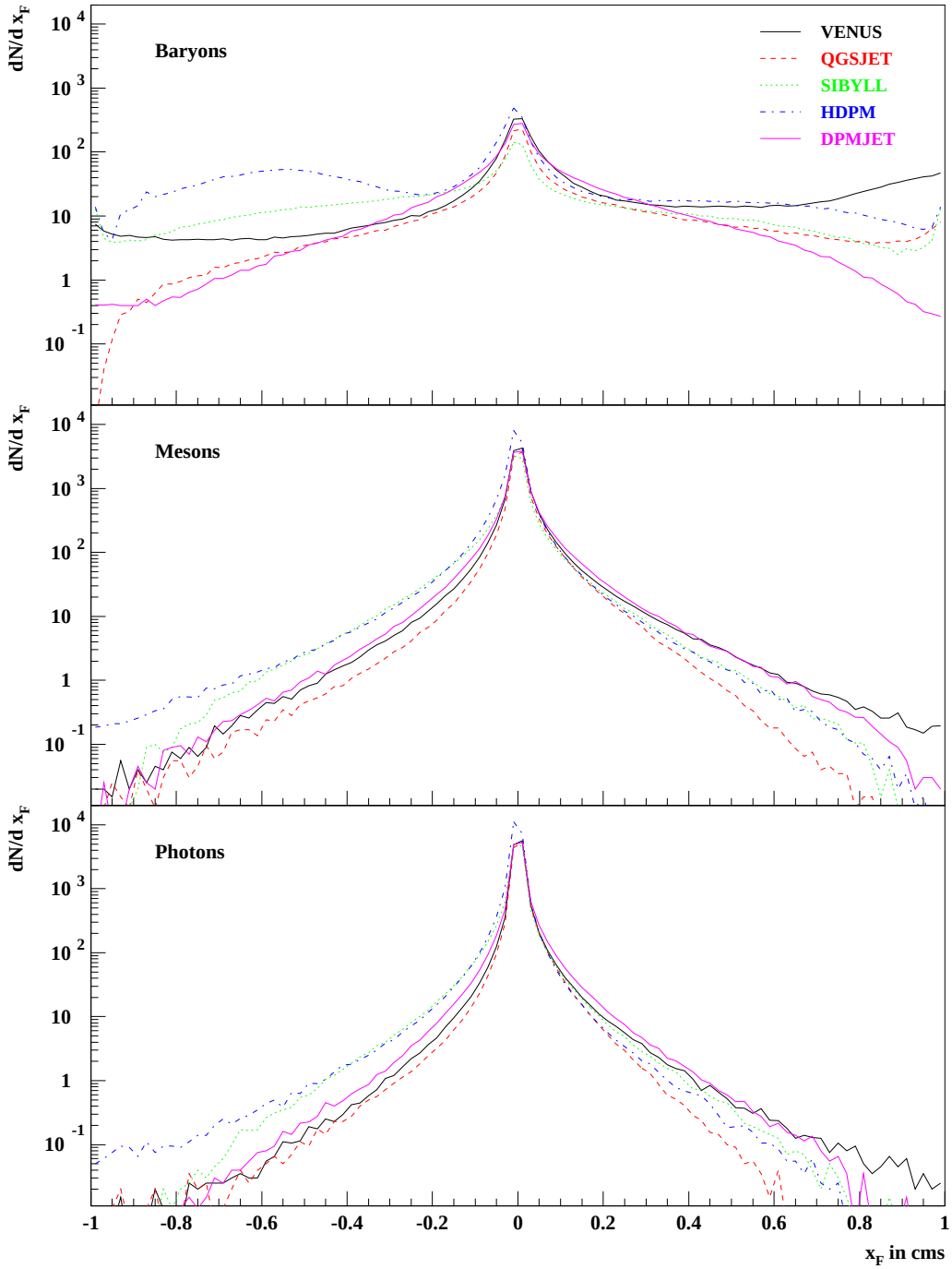

Figure 37: Feynman x_F distributions for baryons, mesons, and photons from collisions of 10^{15} eV Fe on N.

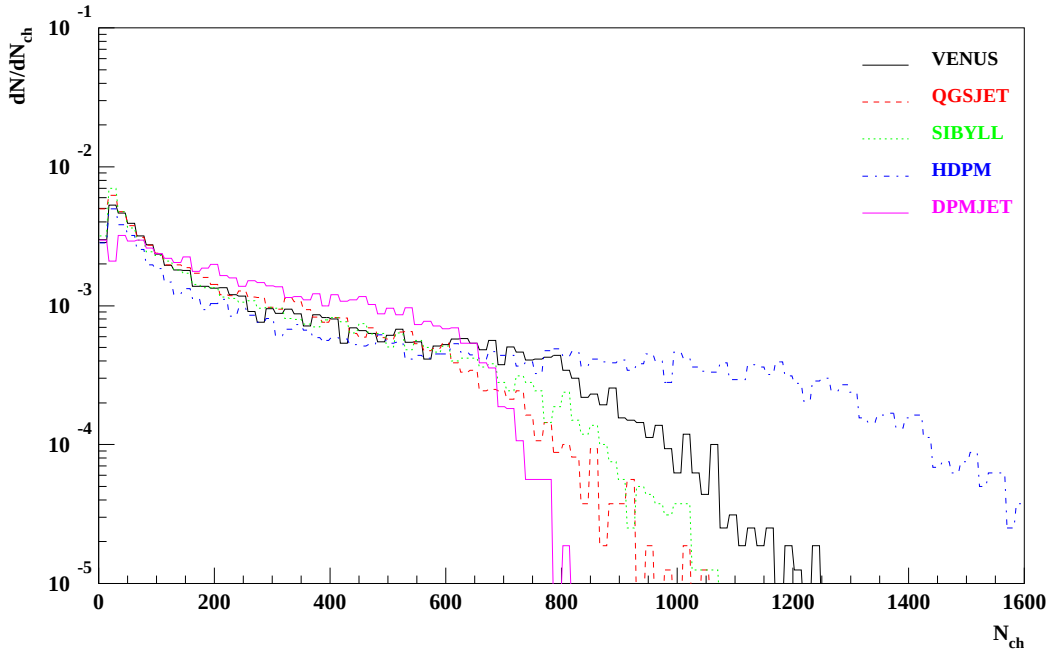

Figure 38: Multiplicity distributions of charged particles from collisions of 10^{15} eV Fe on N.

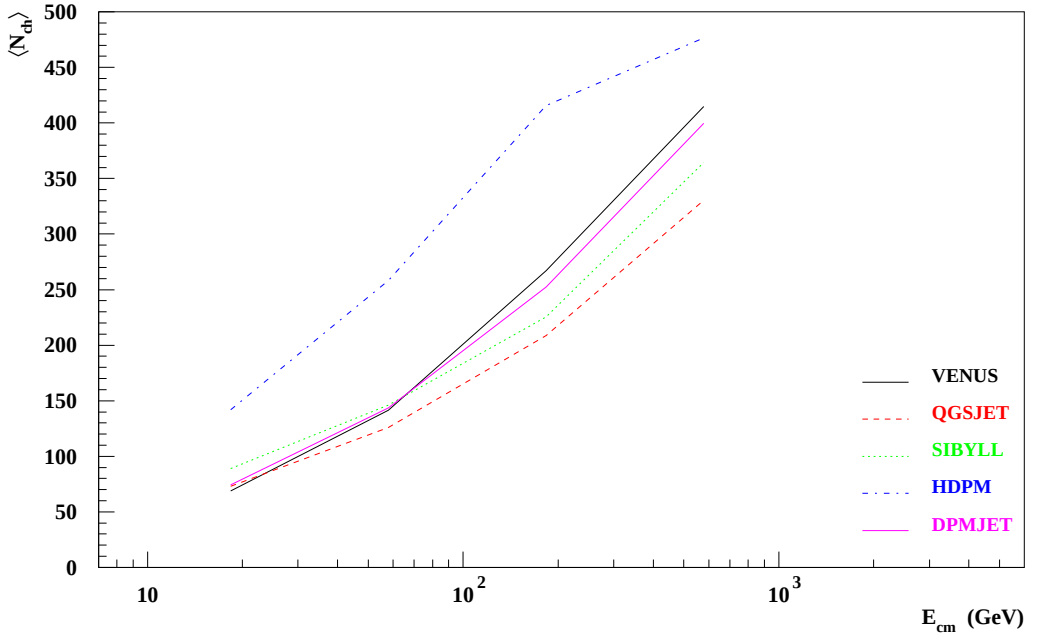

Figure 39: Average charged multiplicities from collisions of Fe on N as a function of the cm energy.

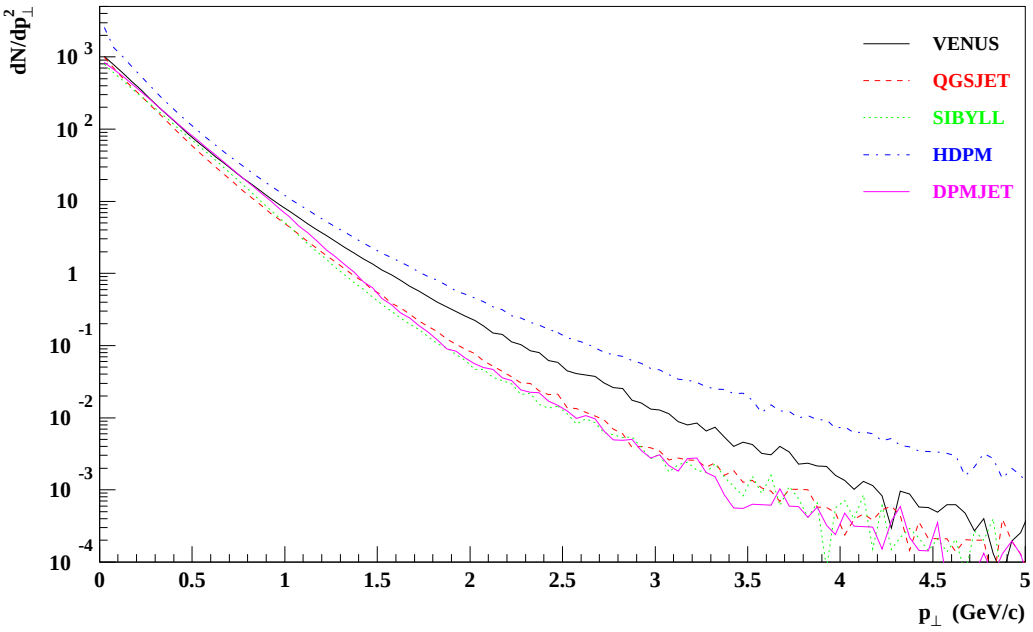

Figure 40: Transverse momentum distributions of charged particles from collisions of 10^{15} eV Fe on N.

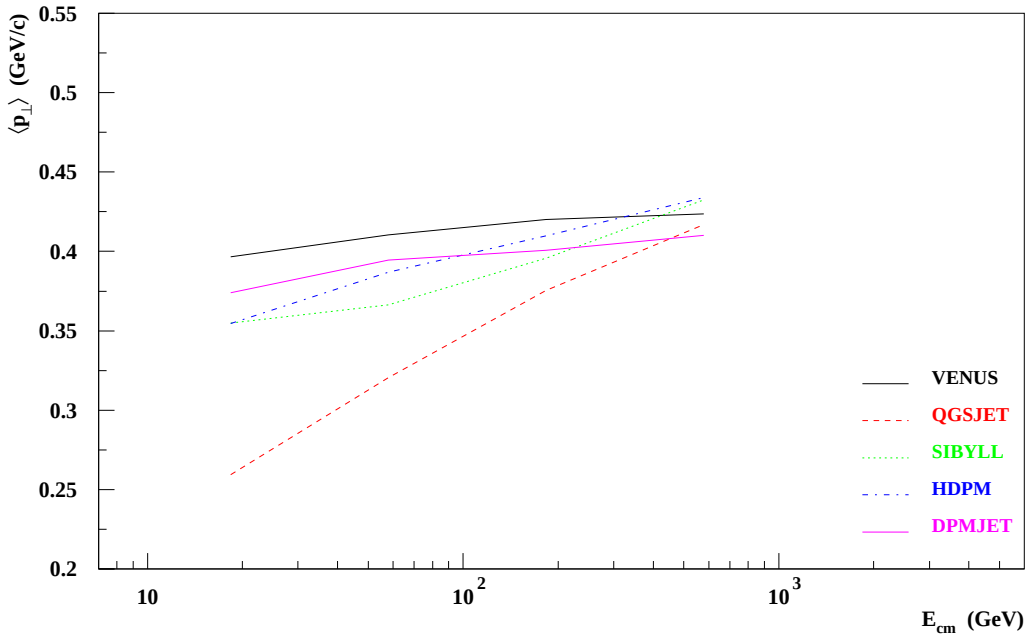

Figure 41: Average transverse momenta of charged particles from collisions of Fe on N as a function of the cm energy.

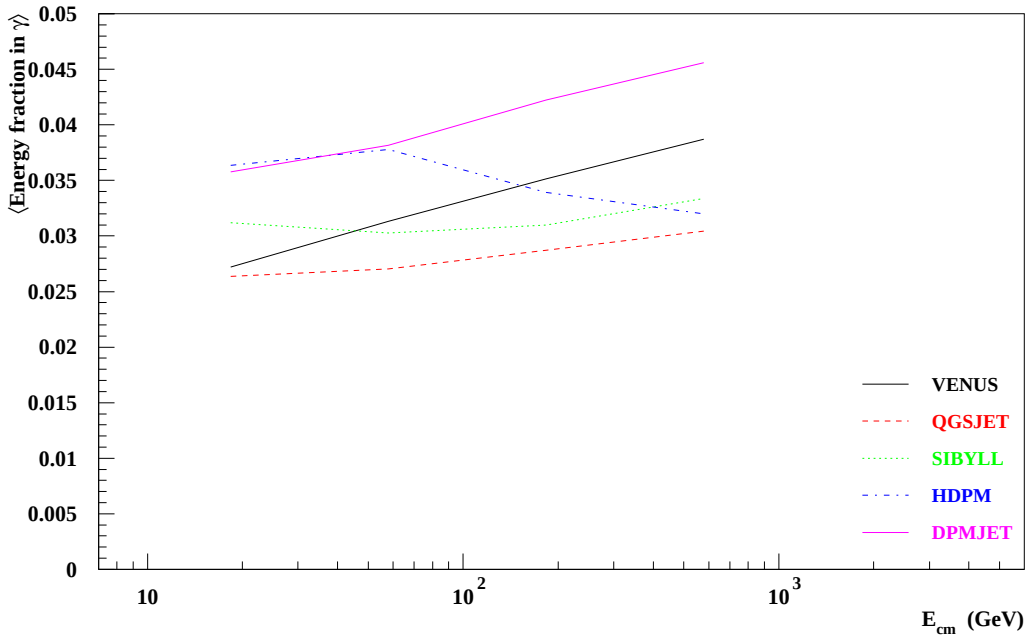

Figure 42: Average energy fraction going into photons from collisions of Fe on N as a function of the cm energy.

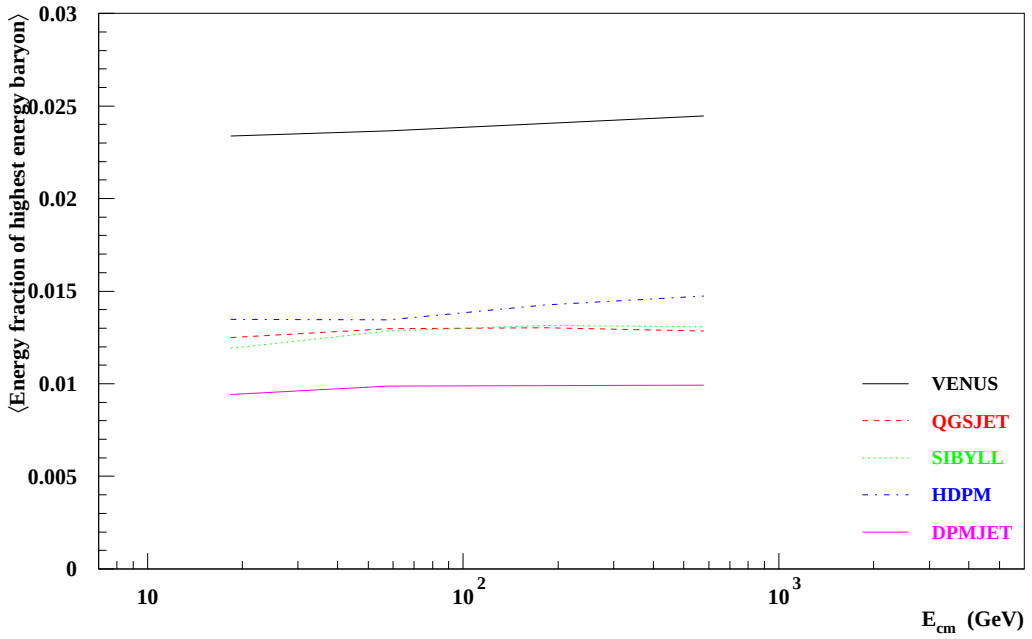

Figure 43: Average energy fraction of the highest energy baryon from collisions of Fe on N as a function of the cm energy.

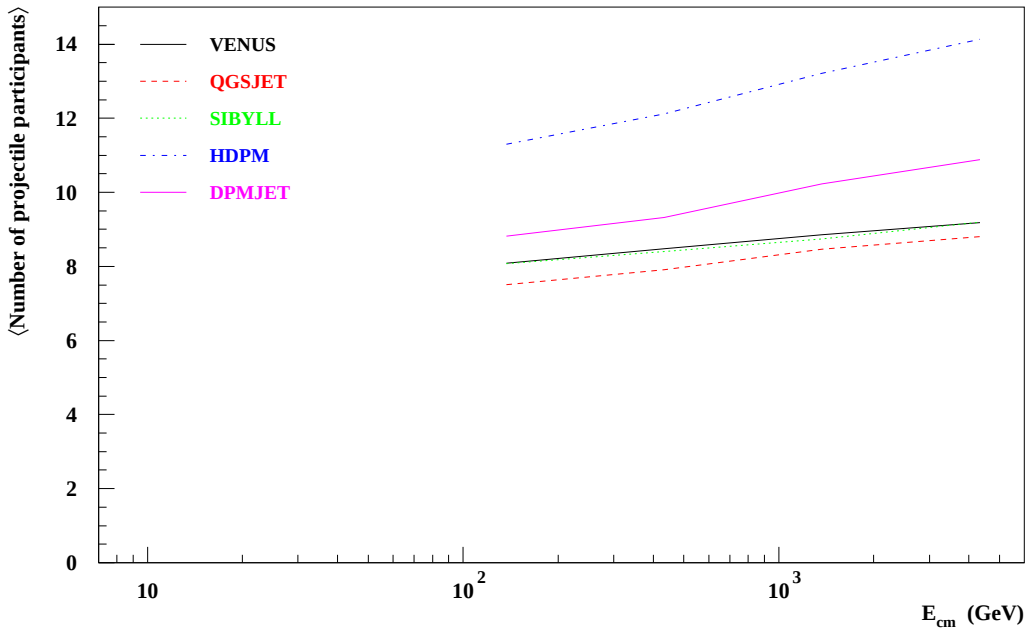

Figure 44: Average numbers of interacting projectile nucleons in collisions of Fe on N as a function of the cm energy.

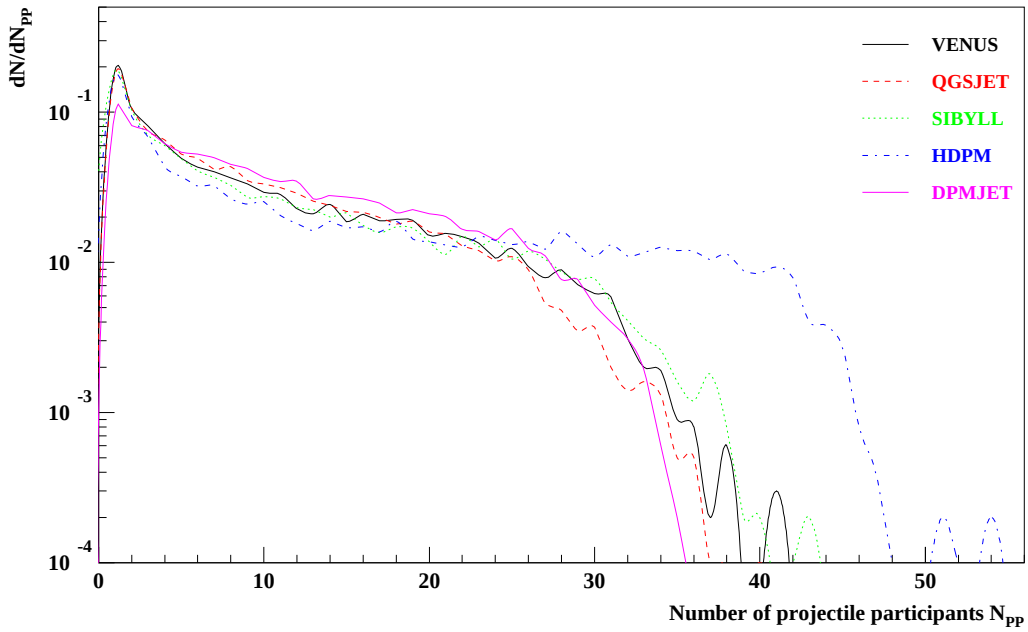

Figure 45: Distributions of the number of interacting projectile nucleons in collisions of 10^{15} eV Fe on N.

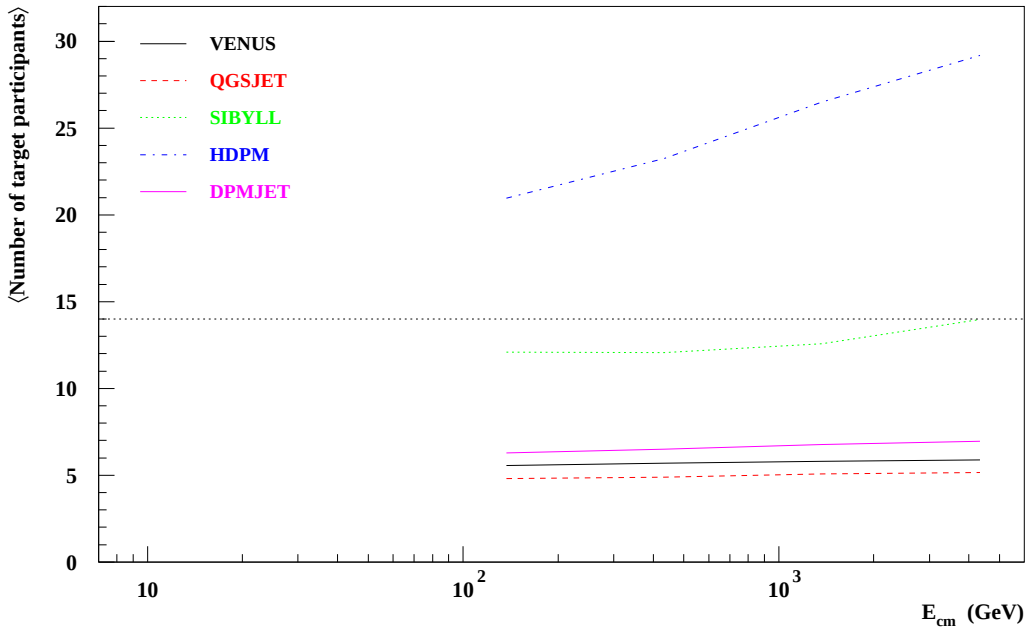

Figure 46: Average numbers of interacting target nucleons in collisions of Fe on N as a function of the cm energy.

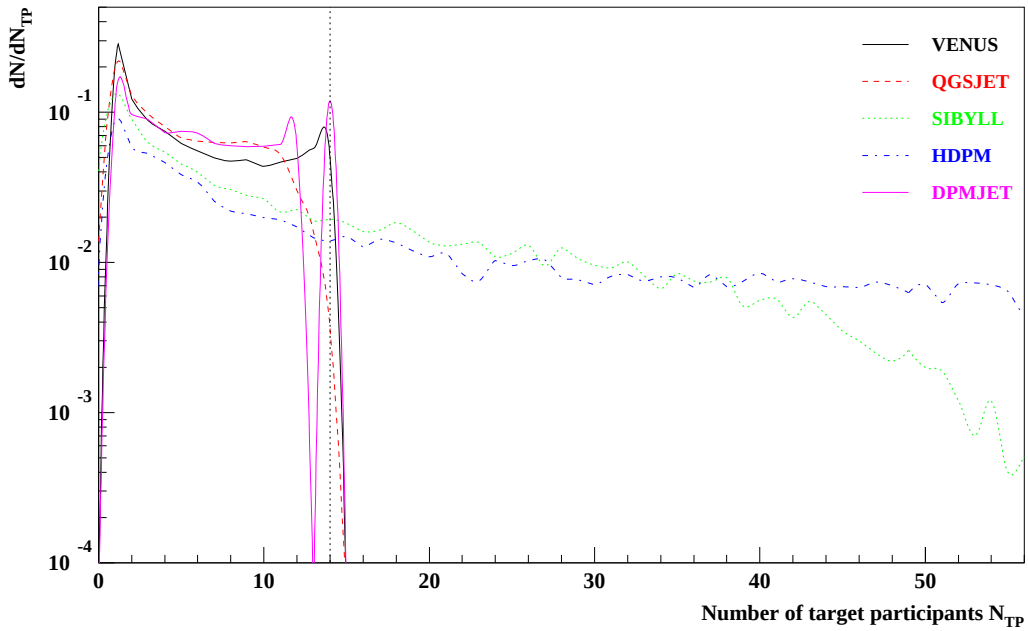

Figure 47: Distributions of the number of interacting target nucleons in collisions of 10^{15} eV Fe on N.

2.5 N-N Collisions

Finally, some results of nitrogen-nitrogen collisions are shown. In Tab. 16 the particle numbers produced in collisions of 10^{15} eV N on N are given.

Similar features as in Fe-N collisions can be observed. HDPM produces much more particles than the other models, VENUS creates many baryons and kaons, and SIBYLL produces less particles and smaller fluctuations than other models.

In Tab. 17 the energy fraction going into the different secondary particles is given. The numbers are similar to those of Fe-N collisions.

The most energetic secondaries are protons or neutrons, only SIBYLL and DPMJET produce highest energy pions in about 10 to 20% of the interactions as can be seen from Tab. 18.

N-N collisions represent a symmetric case of a nucleus-nucleus collision and, therefore, can be used to check the models in this respect. Fig. 48 shows the pseudo rapidity distributions of N-N collisions at $E_{lab} = 10^{15}$ eV. VENUS, QGSJET, and DPMJET create symmetric distributions as expected, because they firstly determine the number of interacting projectile and target nucleons depending on the impact parameter and then scatter these nucleons with each other. HDPM and SIBYLL use the superposition model and, hence, do not treat target and projectile in a symmetric way. This results in an overestimation of particles at the target side which is moderate for SIBYLL but large for HDPM. Since the particles produced by these two codes additionally have small energies in the laboratory system, their influence on the shower development is very small. This will be discussed in more detail in sec. 3.

Figs. 49, 50, 51, and 52 show the average number of interacting projectile and target nucleons in N-N collision versus the cm energy of a nucleon-nucleon subsystem and their distribution at $E_{lab} = 10^{15}$ eV.

$E_0 = 10^{15}$ eV					
	VENUS	QGSJET	SIBYLL	HDPM	DPMJET
p	12.0 ± 8.3	7.2 ± 6.1	7.9 ± 7.0	14.1 ± 11.7	8.5 ± 6.7
$\bar{p}$	4.9 ± 5.0	3.3 ± 3.4	1.8 ± 2.1	6.0 ± 5.7	3.9 ± 3.7
n	11.5 ± 7.8	6.7 ± 5.7	6.1 ± 5.6	13.7 ± 11.8	8.2 ± 6.4
$\bar{n}$	4.4 ± 4.4	3.0 ± 3.2	1.9 ± 2.1	5.8 ± 5.4	3.7 ± 3.6
γ	162.5 ± 156.1	151.6 ± 141.7	146.8 ± 132.4	235.0 ± 199.6	167.7 ± 131.8
π^-	69.2 ± 65.0	58.1 ± 54.5	54.0 ± 48.4	89.7 ± 76.4	70.3 ± 55.1
π^+	68.1 ± 64.2	57.6 ± 54.1	55.0 ± 49.2	89.8 ± 76.3	69.8 ± 54.9
K^{0L}	8.8 ± 9.3	6.0 ± 6.0	5.4 ± 5.4	8.1 ± 7.3	6.9 ± 6.2
K^{0S}	8.8 ± 9.4	6.4 ± 6.3	5.3 ± 5.5	8.1 ± 7.3	7.0 ± 6.2
K^-	8.7 ± 9.3	6.0 ± 6.0	5.2 ± 5.1	8.3 ± 7.6	6.9 ± 6.1
K^+	9.8 ± 10.1	6.4 ± 6.3	5.7 ± 5.6	8.3 ± 7.6	7.3 ± 6.3

Table 16: Average numbers of secondary particles and variances in collisions of 10^{15} eV N on N.

$E_0 = 10^{15}$ eV					
	VENUS	QGSJET	SIBYLL	HDPM	DPMJET
p	14.23	5.53	10.06	5.57	4.48
n	14.15	5.34	3.18	5.26	4.29
$\bar{p}$	0.67	0.34	0.32	0.63	0.60
$\bar{n}$	0.59	0.33	0.37	0.63	0.57
γ	6.03	5.53	6.04	5.09	7.53
π^-	5.42	4.53	4.29	4.27	6.32
π^+	5.18	4.45	5.27	4.27	6.26
K^{0L}	1.07	0.54	0.57	0.65	0.78
K^{0S}	1.12	0.68	0.57	0.64	0.79
K^-	0.85	0.53	0.47	0.64	0.71
K^+	1.40	0.67	0.65	0.63	0.89
Spectators	49.28	71.54	68.21	71.71	66.79

Table 17: Energy fraction going into secondary particles (in %) in collisions of 10^{15} eV N on N.

$E_0 = 10^{15}$ eV					
	VENUS	QGSJET	SIBYLL	HDPM	DPMJET
p	45.95	44.48	66.20	52.55	35.20
$\bar{p}$	0.61	0.22	0.51	0.34	0.88
n	44.61	43.15	13.72	39.69	33.24
$\bar{n}$	0.44	0.35	0.70	0.44	0.79
γ	1.27	2.44	2.61	1.27	5.29
π^-	2.06	4.01	3.05	2.10	10.05
π^+	2.15	3.62	5.07	2.15	9.61
K^{0L}	0.68	0.34	0.49	0.37	1.15
K^{0S}	0.80	0.48	0.47	0.21	1.18
K^-	0.45	0.44	0.28	0.44	0.87
K^+	0.97	0.47	0.39	0.43	1.73

Table 18: Most energetic secondary particles (in %) in collisions of 10^{15} eV N on N.

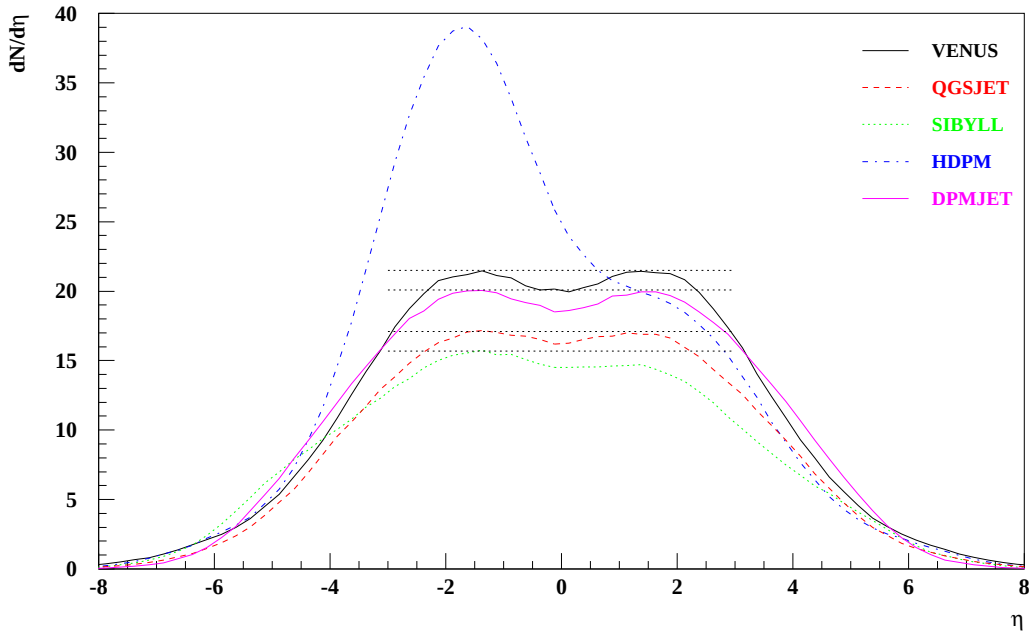

Figure 48: Pseudo rapidity distributions of charged particles from collisions of 10^{15} eV N on N.

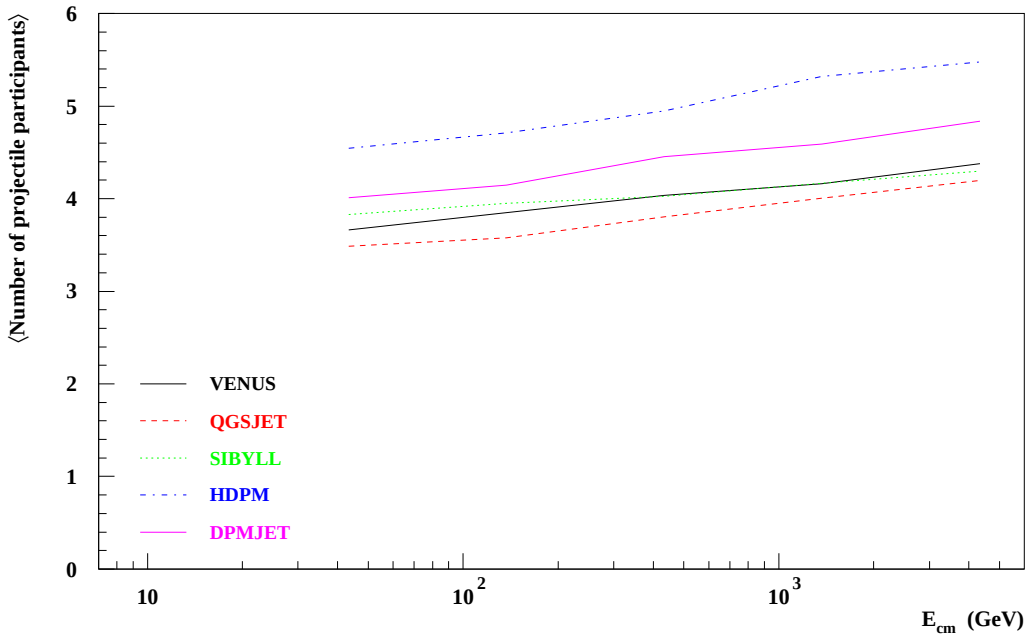

Figure 49: Average numbers of interacting projectile nucleons in collisions of N on N as a function of the cm energy.

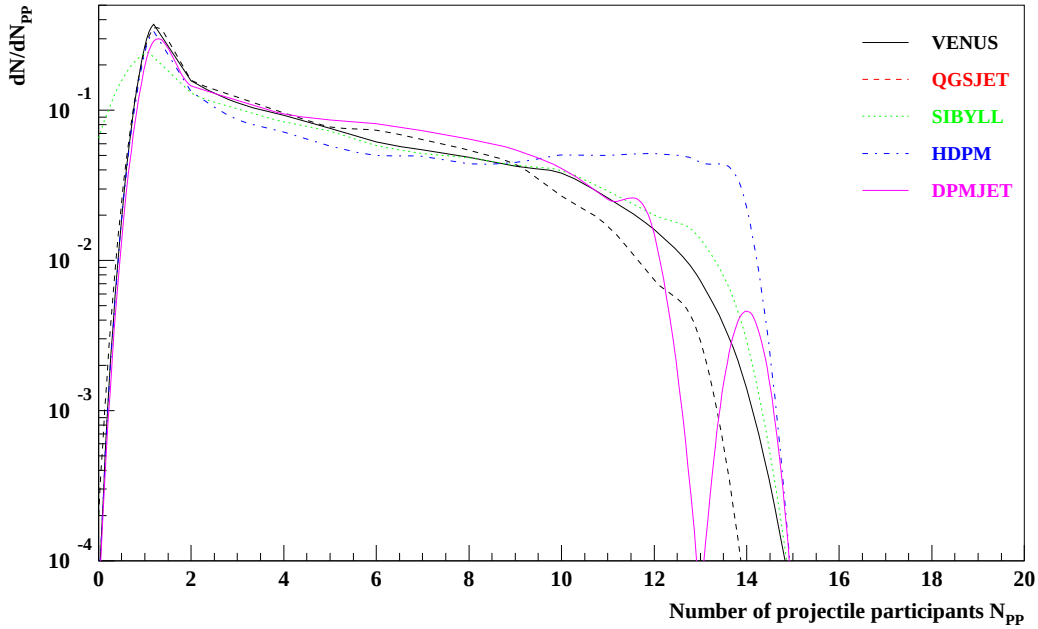

Figure 50: Distributions of the number of interacting projectile nucleons in collisions of 10^{15} eV N on N.

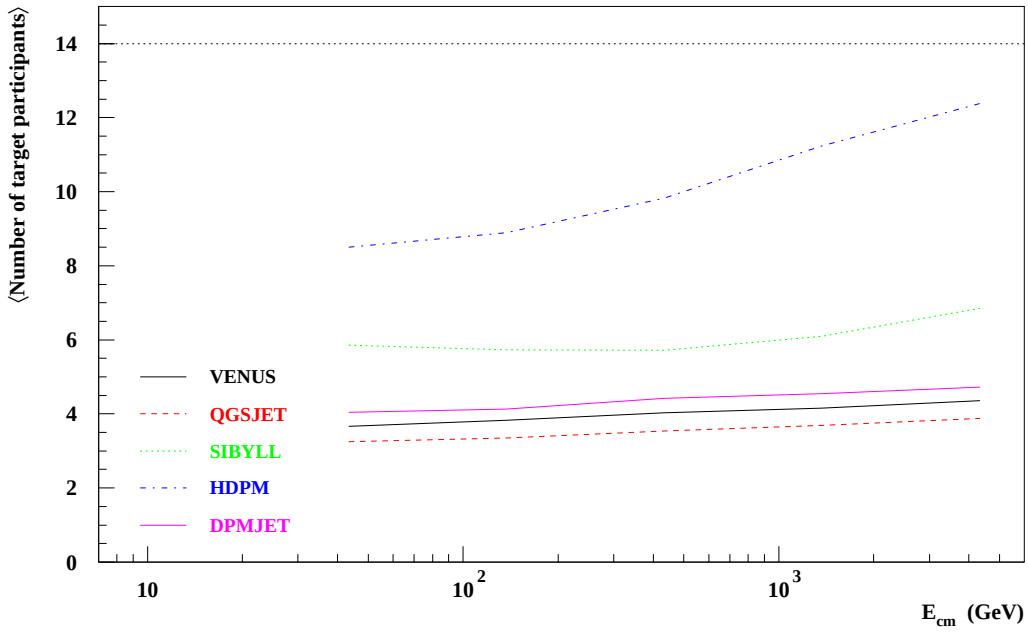

Figure 51: Average numbers of interacting target nucleons in collisions of N on N as a function of the cm energy.

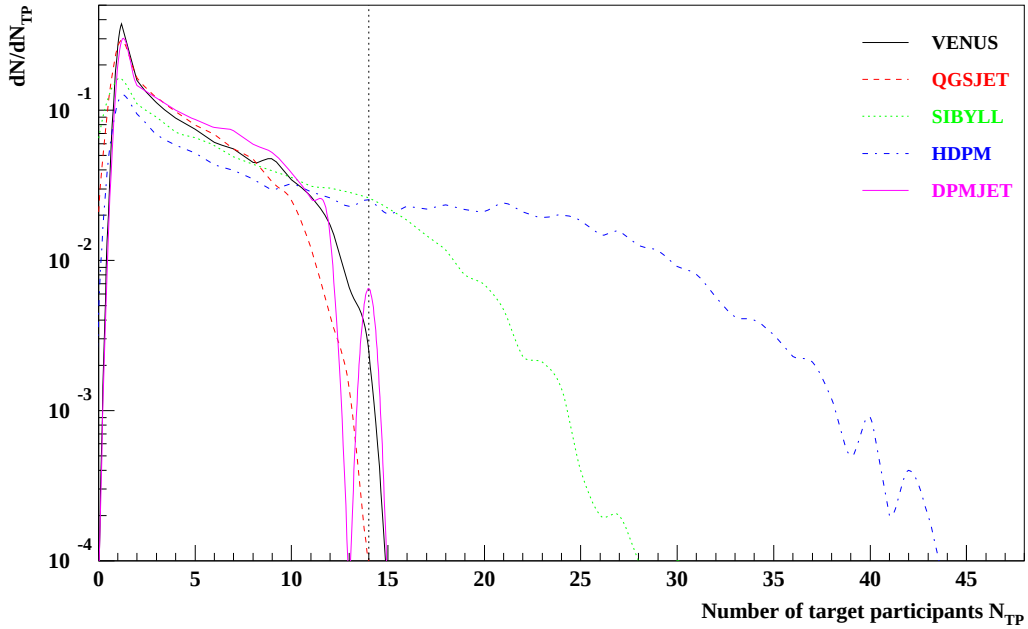

Figure 52: Distributions of the number of interacting target nucleons in collisions of 10^{15} eV N on N.

2.6 Conclusion

There are large differences between the models. Even those based on the same theory (GRT) show considerable variations which must be due to the different implementation of the theoretical ideas in a computer code. SIBYLL and HDPM base on simpler ideas and consequently show larger deviations in some of the variables. It is difficult to estimate which of the quantities discussed above are relevant to the air shower development and observables accessible by air shower experiments. The real test of the various models is the comparison with observable quantities in air showers.

3 Air Shower Calculations

All models were integrated into CORSIKA and for comparison air shower calculations were performed. In order to reveal their influence on observable quantities, all other conditions were kept as identical as possible.

The total inelastic cross sections for hadrons and nuclei are calculated in the way it is usually done by the CORSIKA program [10]. The cross sections for nucleons, pions, and kaons on air are shown in Fig. 53 and the nucleus-nucleus cross sections are presented in Fig. 54. The ratios between the different types of inelastic reactions are evaluated by the models themselves. The models were only used for reactions above $E_{lab} = 80$ GeV/n. Below this threshold the GHEISHA code [11] is used, as normally in CORSIKA. This program has been successfully applied in detector simulations for high energy physics experiments and has been checked repeatedly. It probably produces rather realistic results. Particle tracking with ionization and radiation losses, multiple scattering and decay of unstable particles are performed identically for all models. Electromagnetic sub-showers are simulated with a modified analytic NKG formalism giving the longitudinal shower development, the electron density as a function of core distance, and the total electron number for $E_e > 3$ MeV [9] at observation level. Hadrons and muons are tracked down to 300 MeV kinetic energy. Nuclei always fragment into free nucleons during their first interaction. All other parameters correspond to the CORSIKA default values [16].

With each interaction model, proton and iron induced showers of $E_0 = 10^{14}$ and 10^{15} eV primary energy and vertical incidence were calculated for the observation level of 110 m a.s.l. (Karlsruhe location). 500 showers have been simulated for each run.

3.1 Proton Induced Showers

In Tab. 20 the average particle numbers at observation level are listed for 10^{14} and 10^{15} eV proton showers. The quoted uncertainties are the r.m.s. values of the distributions. (To obtain the error of the means, they should be divided by $\sqrt{500} = 22.4$.) There are clear differences between the models in the mean numbers of particles at observation level. These differences are no artifacts caused by different starting heights as can be inferred from Tab. 19 in which the average heights of the first interaction are listed. At both energies DPMJET showers show the largest number of protons and neutrons but the smallest number of electrons and pions. HDPM has the largest number of electrons, muons, and pions. This can be explained by the fact that DPMJET has the smallest elasticity and, thus, the shower develops faster in the atmosphere than in the other models. HDPM on the other hand has the largest elasticity and, therefore, the shower reaches its maximum deeper in the atmosphere and more particles penetrate to the ground (cf. Tab. 22). Generally, the number of electrons at ground level scales with inelasticity. The inelasticity rises from DPMJET - VENUS - QGSJET - SIBYLL - HDPM and in the same sequence the number of electrons at ground level rises, too. The spread of the electron numbers is 30% at 10^{14} eV and 45% at 10^{15} eV. SIBYLL

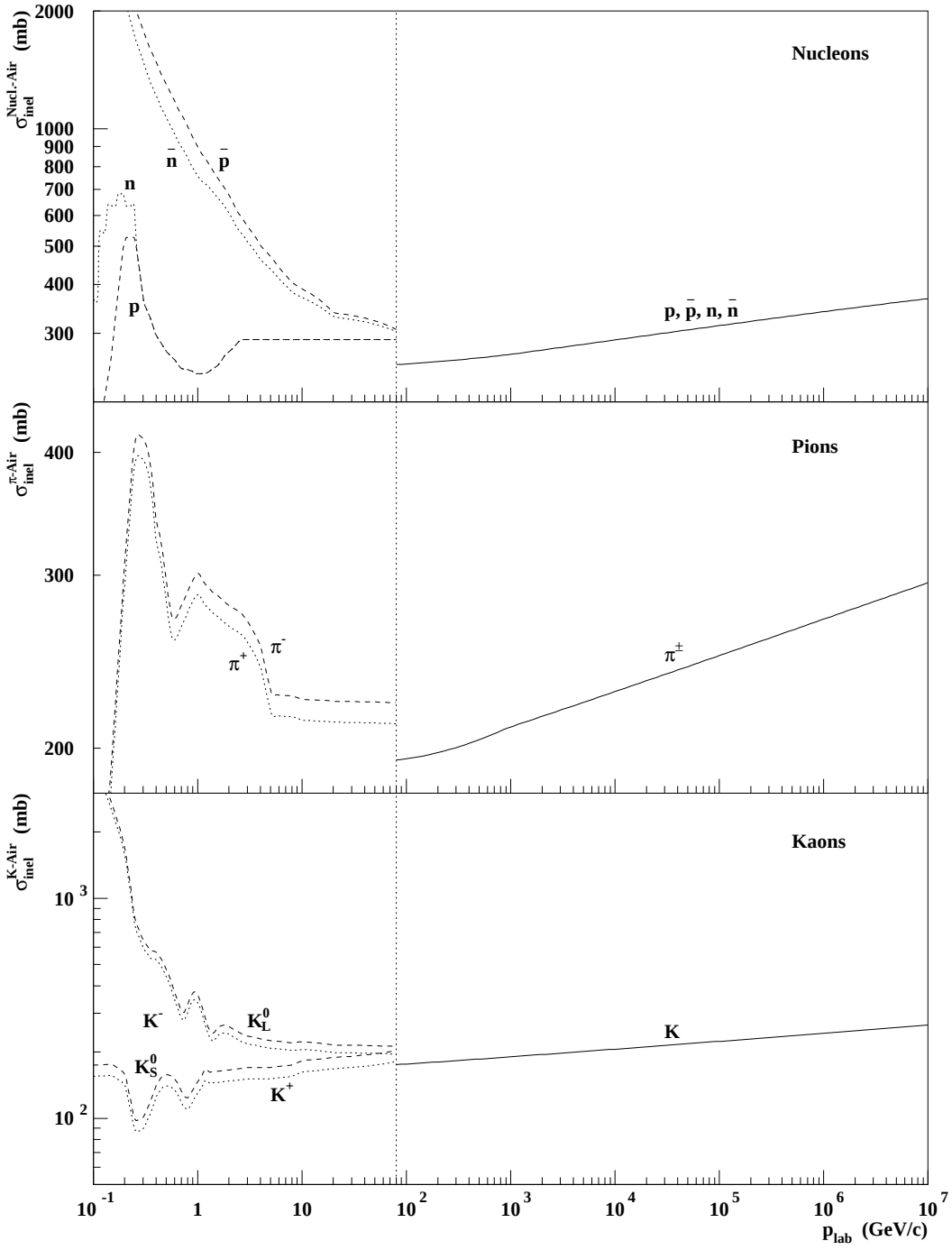

Figure 53: Inelastic cross sections for proton, pion, and kaon collisions with air as used in CORSIKA. For $E < 80$ GeV (vertical dotted line) the cross sections are taken from the GHEISHA program. There are discontinuities in the cross sections at the interface.

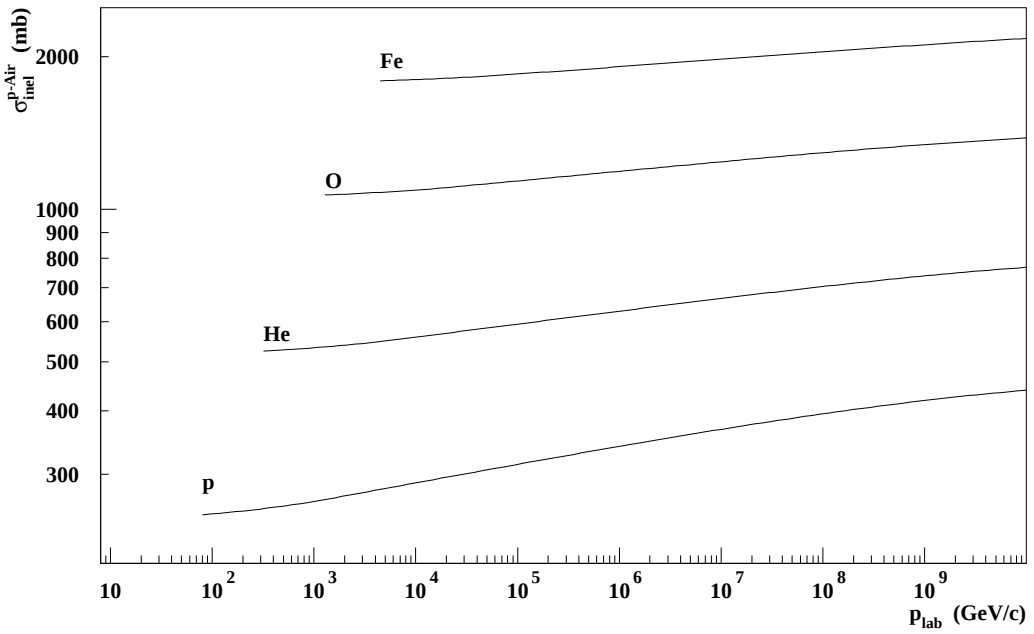

Figure 54: Inelastic cross sections for collisions of protons, helium, oxygen and iron nuclei on air as used in CORSIKA.

tends to produce showers with the smallest number of muons, a consequence of the small number of secondaries produced in each interaction. At high altitudes SIBYLL generates not enough pions that could decay into muons. The difference between SIBYLL and HDPM in the muon number is 60% and still 50% to the VENUS model. QGSJET and VENUS differ by 45% in the number of nucleons and by 20% in the muon and pion number but agree within 4% in the electron number. DPMJET and VENUS agree remarkably well in the nucleon and muon numbers but disagree in the electron number by about 20%.

Tab. 21 gives the average number of muons above several energy thresholds. VENUS produces most high energy muons (see Fig. 57). There are about 25% more muons than in the other models for $E > 1$ TeV. SIBYLL persists to give least muons even up to highest energies.

Figs. 55, 56, and 57 show the energy spectra of baryons, pions, and muons in proton induced showers of 10^{14} and 10^{15} eV. The spectra are normalized to the number of showers. The energy distributions of baryons decrease monotonously. The peaks at low energies are due to the cut-off and contain mainly neutrons which increase steeply with falling energy and dominate the hadrons below 3 GeV. The slight discontinuity in the hadron energy spectra at $E = 80$ GeV (corresponding to $\log_{10} E = 1.9$) is caused by the transition from the high energy interaction model to the GHEISHA model (see Fig. 53). In correspondence with the numbers of Tab. 20, VENUS and DPMJET produce most baryons. In the plot it can be noted that DPMJET is highest for $E < 20$ GeV, VENUS dominates for $20 < E < 200$ GeV and above HDPM produces most hadrons. The difference between the baryon spectra of VENUS and QGSJET is about a factor of 2.

The pion and muon energy spectra attain their maximum at about 10 GeV. Here the differences are largest, whereas the curves approach each other at higher energies. Therefore, lower energy pions account for most of the differences apparent from Tab. 20. Bearing in mind that interactions below 80 GeV are calculated by the same model in all cases, it must be concluded that this is

an indirect effect. The energy spectra scatter by a factor 2 or more. HDPM gives most pions, followed by VENUS, QGS, SIBYLL, and DPMJET. The muon energy spectrum illustrates the deficit of SIBYLL in the number of muons. HDPM produces most muons below about 10 GeV, above VENUS has the highest density.

In Fig. 58 the lateral distributions of pions produced in proton showers of 10^{14} and 10^{15}eV are presented. HDPM produces most pions for $r < 100$ m. DPMJET has the flattest distribution with a central density two times lower than the other models.

Fig. 59 gives the lateral distributions of electrons at observation level in 10^{14} and 10^{15} eV proton showers. The lines indicate the results of a fit of the form

$$\rho(r) = a \left(\frac{r}{b}\right)^{c-2} \left(1 + \frac{r}{b}\right)^{4.5-d}$$

to the points obtained from CORSIKA where r is the core distance and a, b, c, and d are the fit parameters. The lateral distribution is flattest for DPMJET showers, because they develop rapidly due to the large inelasticity and is steepest for the low inelasticity models HDPM and SIBYLL in correspondence with the longitudinal development. VENUS and QGSJET generate electron densities in between. The fit parameters are given in Tab. 23. At large radii the models approach each other more and more, indicating only a small model dependence of the electron density for large core distances. Here the electron densities are dominated by multiple scattering, which is the same for all calculations, rather than by the hadronic interaction model.

The lateral distribution of muons in p induced showers is shown in Fig. 60. The variation for different models is about a factor of 2 up to $r = 2$ km. SIBYLL gives the smallest muon densities.

The average longitudinal development of the electron number in 10^{14} and 10^{15} eV proton showers is represented in Fig. 61. The dots indicate the electron numbers in steps of 100 g/cm^2 and the lines represent fits of the form

$$N(t) = N_{max} \left(\frac{t - t_0}{t_{max} - t_0}\right)^{\frac{t_{max}-t}{a+bt+ct^2}} \quad ,$$

where t is the atmospheric depth in radiation lengths and N_{max}, t_0, t_{max}, a, b, and c are fit parameters. The values of the fitted t_{max}, the position of the shower maximum, are shown for $E = 10^{14}$ and 10^{15} eV in Tab. 22. Obviously DPMJET showers reach the maximum first and subsequently die out quicker, leading to small electron numbers at observation level. This follows directly from the high inelasticity of the DPMJET generator in single interactions. HDPM and SIBYLL showers develop more slowly because of their small inelasticity and, therefore, have high electron numbers at ground level. SIBYLL in addition reaches the highest electron numbers at maximum which is reflected by the rather large energy fraction going into photons in π-N collisions. VENUS and QGSJET lie between these extremes. The elongation rate at these energies varies between 68 and 78 g/cm^2 per decade.

In Fig. 62 the N_e distributions are indicated for 10^{14} and 10^{15} eV proton showers. The distributions are similar in shape but differ in their mean value as indicated in Tab. 20. DPMJET showers have small and HDPM showers have high electron numbers. The widths of the distributions of different models in this log plot is roughly the same.

In Fig. 63 the N_μ distributions of 10^{14} and 10^{15} eV proton shower are displayed. It is conspicuous that SIBYLL showers show a stronger asymmetry and a longer tail to small muon numbers than the other models which do not differ much in the shape of their distributions. This may be of relevance for the question of discrimination between primary gammas and hadrons.

energy	HDPM	VENUS	SIBYLL	QGSJET	DPMJET
10^{14} eV	79.4 ± 83.8	77.3 ± 78.7	75.9 ± 77.2	80.3 ± 88.6	75.2 ± 75.4
10^{15} eV	66.0 ± 66.7	71.1 ± 72.2	69.6 ± 68.6	73.6 ± 69.4	77.1 ± 82.5

Table 19: Average atmospheric depths of first interaction and their standard deviations (in g/cm^2) for proton induced showers.

10^{14} eV					
	VENUS	QGSJET	SIBYLL	HDPM	DPMJET
p	58.9 ± 38.1	45.9 ± 33.0	50.2 ± 32.9	55.5 ± 37.1	64.6 ± 46.3
$\overline{p}$	1.8 ± 1.9	1.1 ± 1.6	1.1 ± 1.4	1.8 ± 2.0	1.8 ± 2.4
n	129.5 ± 69.0	102.2 ± 61.5	107.1 ± 60.1	120.7 ± 67.2	141.8 ± 81.3
$\overline{n}$	2.4 ± 2.5	1.4 ± 1.8	1.4 ± 1.8	2.0 ± 2.2	2.4 ± 2.9
μ^-	666.6 ± 171.6	630.8 ± 183.8	530.7 ± 158.4	743.5 ± 194.5	651.9 ± 192.1
μ^+	691.7 ± 178.4	648.3 ± 187.9	543.8 ± 160.9	765.8 ± 197.1	680.6 ± 198.9
π^-	9.7 ± 11.6	9.7 ± 13.2	9.9 ± 12.2	14.4 ± 17.5	8.7 ± 11.9
π^+	9.8 ± 11.4	9.9 ± 13.6	10.2 ± 12.2	15.1 ± 18.1	9.1 ± 12.3
K_L^0	0.5 ± 0.8	0.5 ± 0.9	0.4 ± 0.9	0.5 ± 0.9	0.4 ± 0.9
K_S^0	0.0 ± 0.0	0.0 ± 0.0	0.0 ± 0.0	0.0 ± 0.1	0.0 ± 0.0
K^-	0.2 ± 0.5	0.2 ± 0.5	0.2 ± 0.5	0.2 ± 0.6	0.2 ± 0.5
K^+	0.2 ± 0.6	0.1 ± 0.4	0.2 ± 0.5	0.2 ± 0.5	0.2 ± 0.5
$e^\pm$	7745 ± 6983	8530 ± 8855	9541 ± 8904	9644 ± 8235	6851 ± 6876
10^{15} eV					
	VENUS	QGSJET	SIBYLL	HDPM	DPMJET
p	647.9 ± 275.6	438.6 ± 223.3	448.7 ± 211.6	578.9 ± 230.1	666.1 ± 328.3
$\overline{p}$	23.5 ± 14.2	12.7 ± 8.9	11.7 ± 8.1	20.0 ± 11.8	19.5 ± 14.7
n	1360.2 ± 496.7	931.4 ± 407.5	915.8 ± 377.1	1206.5 ± 402.0	1407.7 ± 574.2
$\overline{n}$	28.6 ± 16.7	16.1 ± 11.3	14.3 ± 8.8	23.7 ± 13.3	25.2 ± 18.4
μ^-	5800.9 ± 1229.2	4942.0 ± 1241.3	3874.6 ± 1076.5	6207.4 ± 1146.3	5723.2 ± 1287.1
μ^+	5996.6 ± 1262.9	5076.2 ± 1262.4	3960.1 ± 1089.1	6383.4 ± 1167.3	5953.5 ± 1323.6
π^-	135.1 ± 97.7	113.2 ± 96.4	112.4 ± 87.7	178.8 ± 122.9	96.4 ± 89.5
π^+	139.3 ± 100.3	117.4 ± 100.6	116.4 ± 92.0	184.8 ± 127.8	100.5 ± 91.7
K_L^0	7.4 ± 6.6	5.7 ± 5.6	5.2 ± 5.0	5.9 ± 5.1	4.9 ± 5.5
K_S^0	0.0 ± 0.2	0.0 ± 0.2	0.0 ± 0.2	0.0 ± 0.1	0.0 ± 0.2
K^-	3.0 ± 3.3	2.3 ± 2.8	1.9 ± 2.4	2.6 ± 2.7	1.7 ± 2.3
K^+	2.9 ± 3.2	1.9 ± 2.5	2.3 ± 3.0	2.7 ± 2.8	1.7 ± 2.2
$e^\pm$	131093 ± 83842	136475 ± 89284	158902 ± 99441	162209 ± 91309	111533 ± 87445

Table 20: Average particle numbers and variances at observation level for proton induced showers at $E_0 = 10^{14}$ and 10^{15} eV.

energy	model	average number of muons above threshold energy				
		> 0.3 GeV	> 1GeV	> 10 GeV	> 100 GeV	> 1 TeV
10^{14} eV	VENUS	1358	1150	349	24.0	0.604
	QGSJET	1279	1085	316	20.5	0.588
	SIBYLL	1075	904	272	18.9	0.554
	HDPM	1509	1269	354	21.4	0.558
	DPMJET	1332	1124	332	21.1	0.650
10^{15} eV	VENUS	11798	9706	2653	155.0	4.156
	QGSJET	10018	8298	2207	124.9	3.240
	SIBYLL	7835	6415	1756	105.3	2.934
	HDPM	12591	10305	2576	136.2	3.186
	DPMJET	11677	9667	2603	133.6	3.372

Table 21: Average numbers of muons per shower above threshold energy in proton induced showers.

	depths of maximum at $E = 10^{14}$ eV (g/cm^2)	$E = 10^{15}$ eV (g/cm^2)	difference (g/cm^2)
VENUS	503	574	71
QGSJET	504	576	72
SIBYLL	519	592	73
HDPM	521	599	78
DPMJET	492	560	68

Table 22: Average depths of maximum for proton induced showers at 10^{14} and 10^{15} eV.

energy	model	a $\times 10^{-3}$	b (m)	c	d
10^{14} eV	VENUS	0.256	31.0	1.46	1.74
	QGSJET	0.341	27.5	1.46	1.81
	SIBYLL	0.303	31.6	1.38	1.77
	HDPM	0.238	34.3	1.33	1.86
	DPMJET	0.114	42.2	1.29	1.82
10^{15} eV	VENUS	2.55	42.2	1.22	1.59
	QGSJET	3.22	38.1	1.24	1.63
	SIBYLL	3.72	38.7	1.22	1.58
	HDPM	4.29	33.9	1.24	1.80
	DPMJET	2.73	35.6	1.29	1.77

Table 23: Parameters of lateral distributions of electrons at 110 m a.s.l. for proton induced showers at 10^{14} and 10^{15} eV.

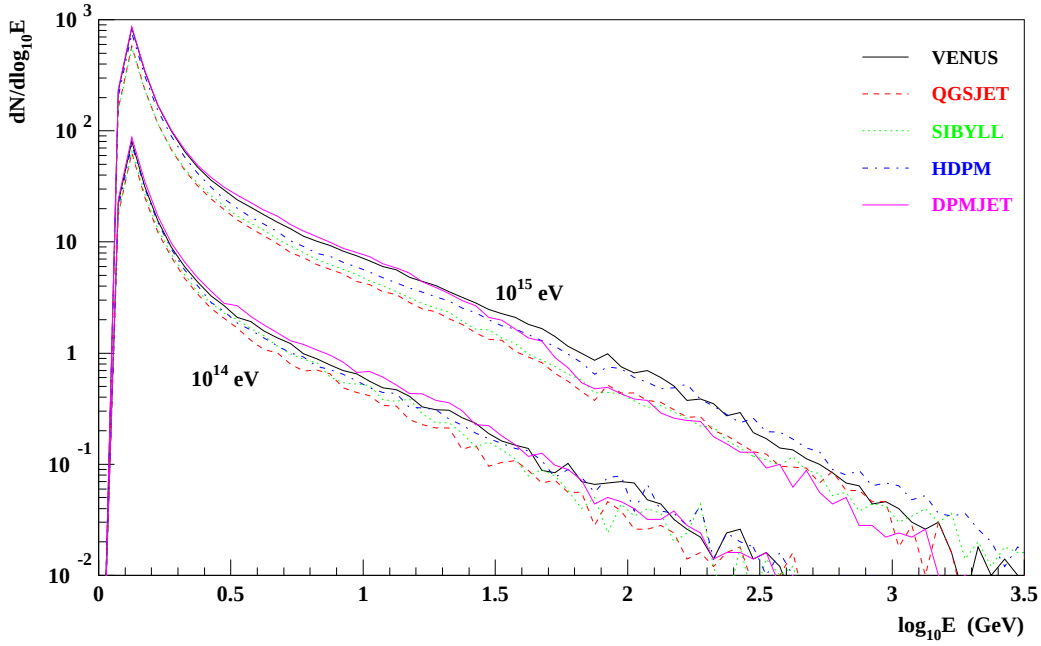

Figure 55: Energy spectra of all baryons at 110 m a.s.l. for proton induced showers with $E_0 = 10^{14}$ and 10^{15} eV.

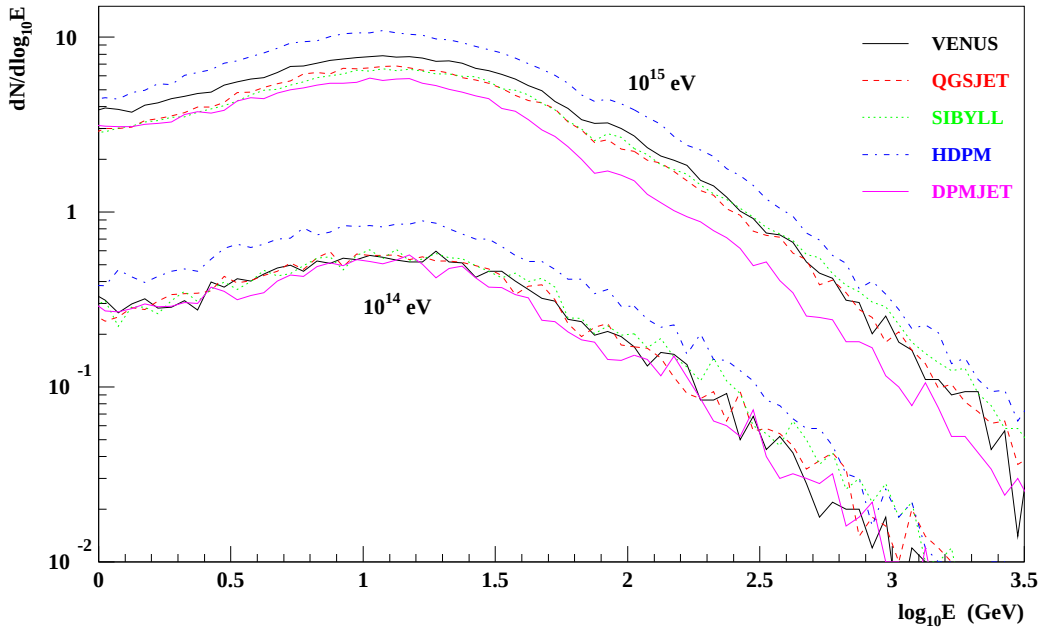

Figure 56: Energy spectra of charged pions at 110 m a.s.l. for proton induced showers with $E_0 = 10^{14}$ and 10^{15} eV.

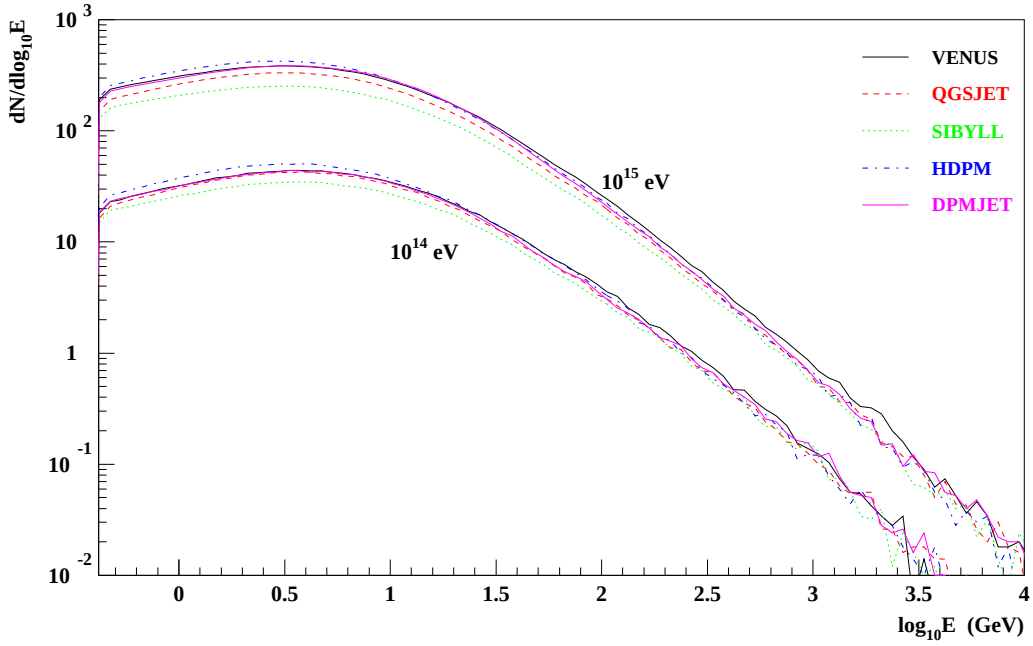

Figure 57: Energy spectra of muons at 110 m a.s.l. for proton induced showers with $E_0 = 10^{14}$ and 10^{15} eV.

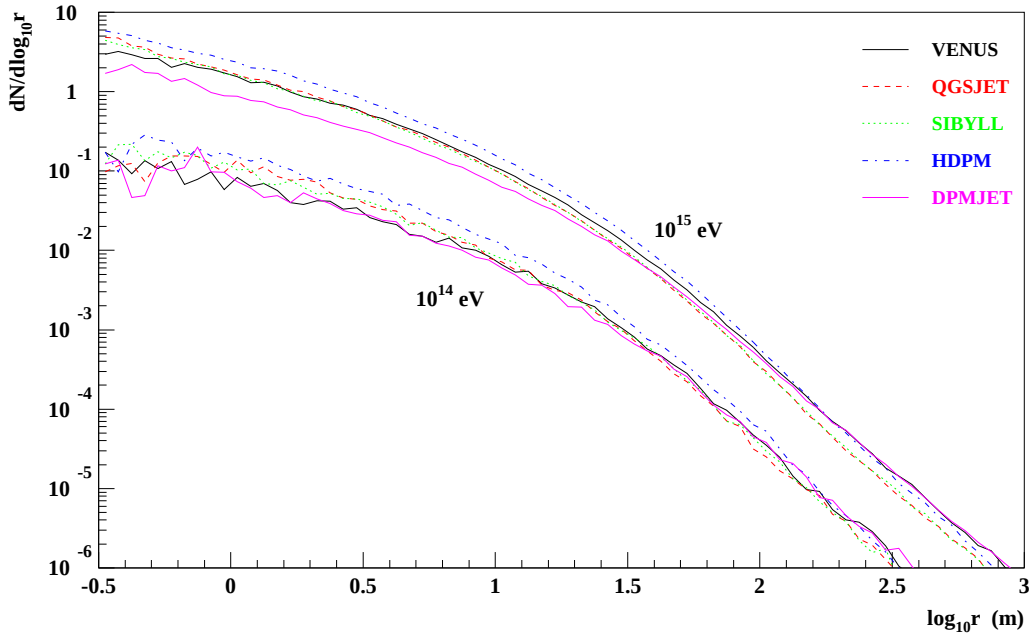

Figure 58: Lateral distributions of charged pions at 110 m a.s.l. for proton induced showers with $E_0 = 10^{14}$ and 10^{15} eV.

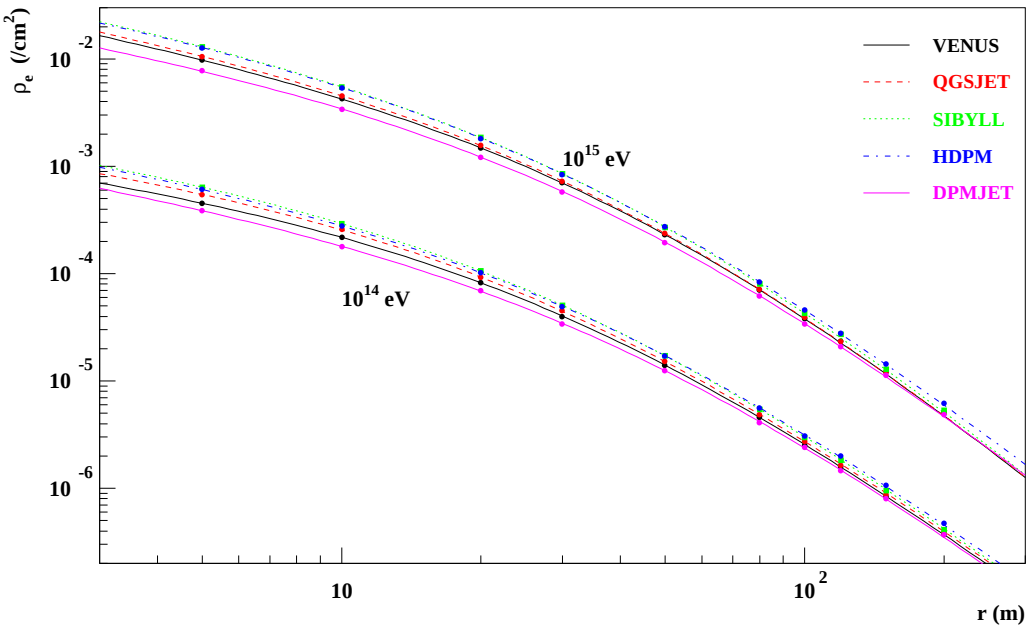

Figure 59: Lateral distributions of electrons at 110 m a.s.l. for proton induced showers with $E_0 = 10^{14}$ and 10^{15} eV. The lines are fits to the Monte Carlo data.

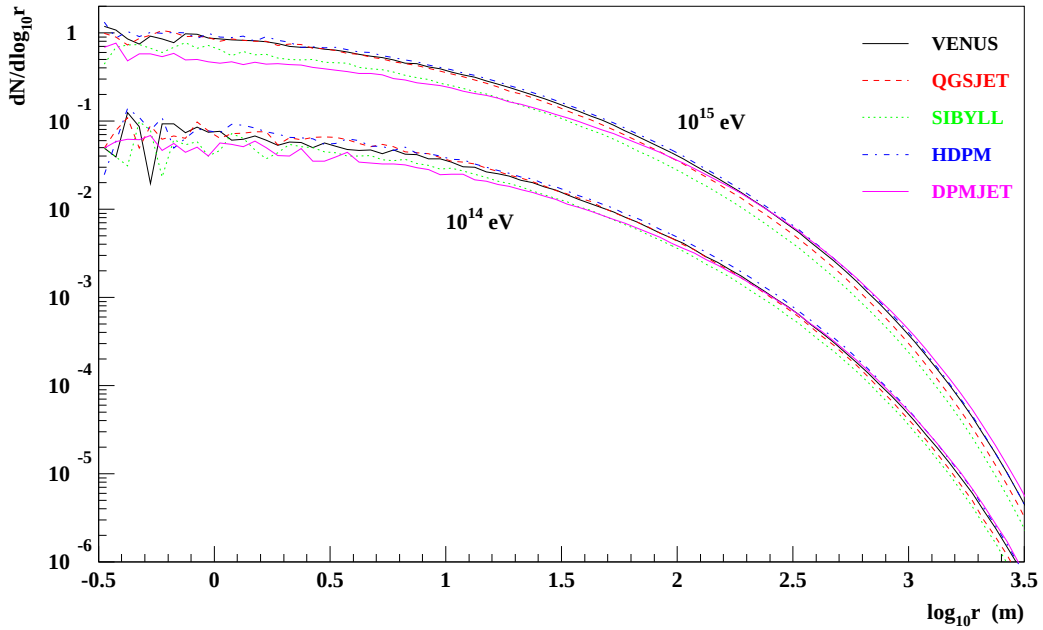

Figure 60: Lateral distributions of muons at 110 m a.s.l. for proton induced showers with $E_0 = 10^{14}$ and 10^{15} eV.

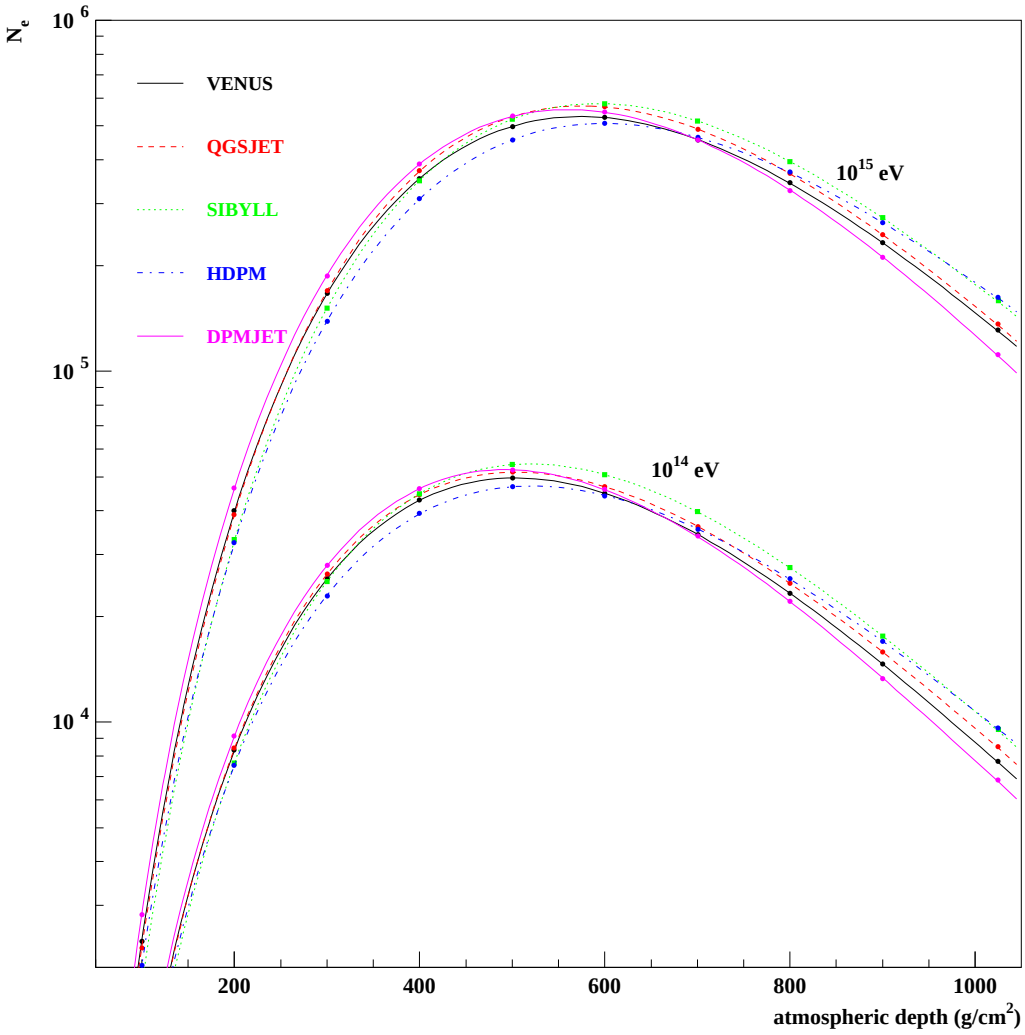

Figure 61: Longitudinal distributions of electrons for proton induced showers with $E_0 = 10^{14}$ and 10^{15} eV. The lines are fits to the Monte Carlo data.

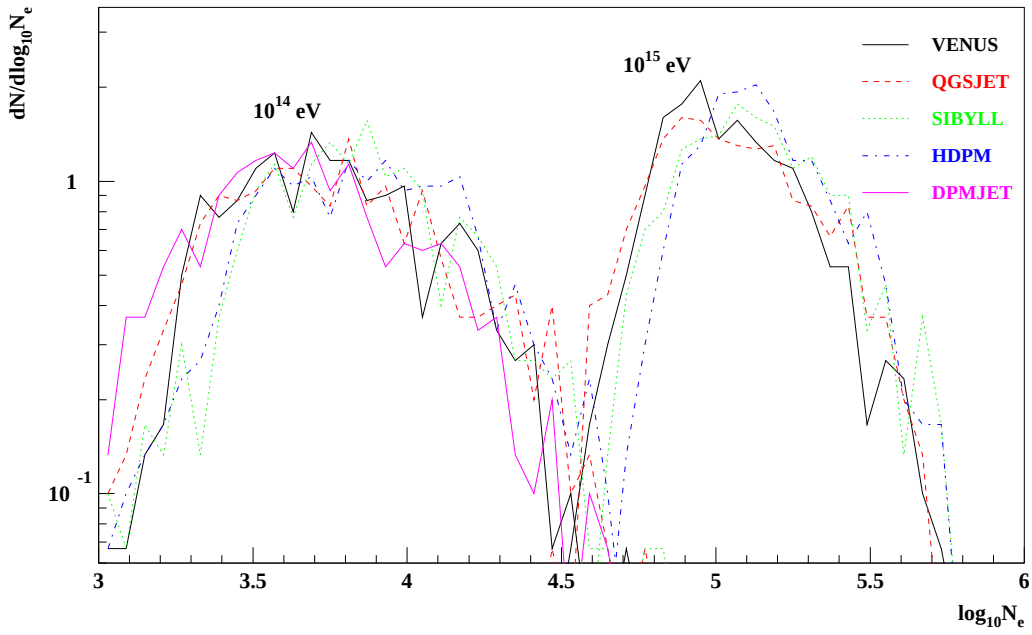

Figure 62: Distributions of electron number at 110 m a.s.l. for proton induced showers with $E_0 = 10^{14}$ and 10^{15} eV.

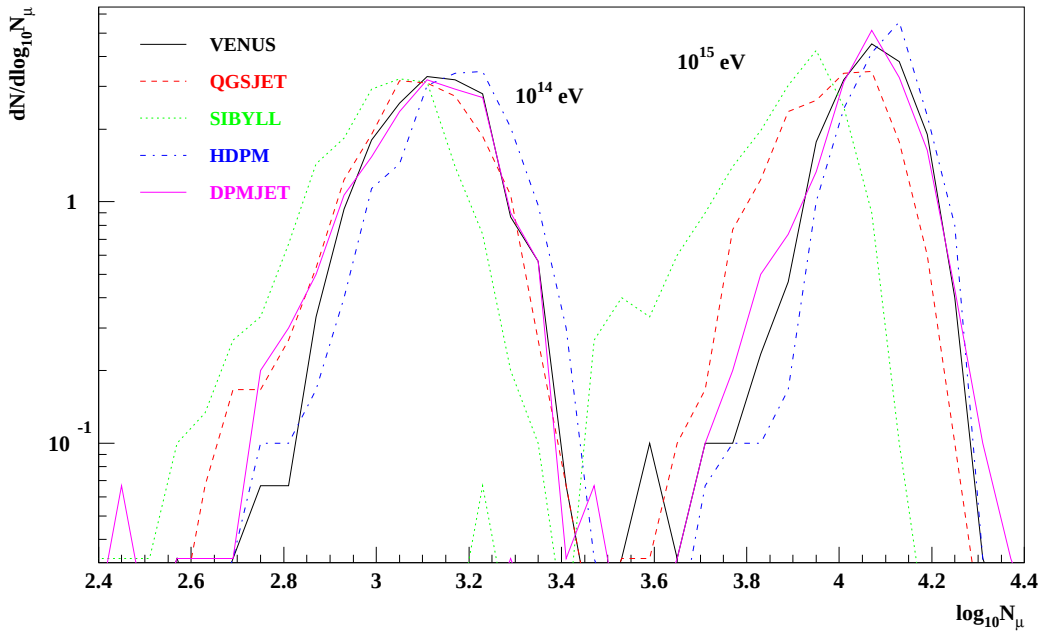

Figure 63: Distributions of muon number at 110 m a.s.l. for proton induced showers with $E_0 = 10^{14}$ and 10^{15} eV.

3.2 Iron Induced Showers

In Tab. 26 the average particle numbers registered in 10^{14} and 10^{15} eV iron showers at observation level are listed. The average height of the first interaction is nearly the same for all models as in the case of the proton induced showers (see Tab. 24). Here the situation is more complicated as the numbers reflect a convolution of the particle production properties of the models and the treatment of the nucleus-nucleus interaction. The spread of electron numbers is 15% at 10^{14} eV and 40% at 10^{15} eV. For the muon numbers the models give differences of 20% and 30%, respectively. The GRT based models agree better with each other, the spread being about 10% for the electron and 5% for the muon numbers. At both energies DPMJET showers show the smallest number of electrons and pions. HDPM has the largest number of muons and is followed by VENUS, DPMJET, and QGSJET. As for proton showers SIBYLL produces the smallest number of muons. It gives the largest number of electrons at observation level. VENUS and QGSJET agree in electron and muon number to better than 5%. Compared to the numbers for protons the models predict about a third of the number of electrons but 50 to 70% more muons.

Tab. 27 presents the average muon number above various energy thresholds. The spread of the number of muons with $E_\mu > 1$ TeV at $E_0 = 10^{15}$ eV is 11% only, whereas for p induced showers it is 42%. The numbers for 10^{14} eV Fe showers are close to zero, as 10^{14} iron corresponds to 1.78 TeV/n and, consequently, the chance is low to create TeV muons at all. DPMJET produces TeV muons relatively easily, as it transfers most energy to secondary pions and turns easiest the leading particles into a pion in $\bar{p}$-p collisions.

The energy spectra for baryons, pions, and muons in Figs. 64, 65, and 66 show a shape similar to the spectra for proton induced showers. There are less high energy baryons in iron showers, whereas their total number is almost the same. In proton showers there is twice the number of pions and the spectrum is slightly harder. Muons in iron showers are slightly more energetic than in proton showers. The differences between the models are clearly smaller for iron showers in all spectra.

The lateral distribution of pions in Fe induced showers is shown in Fig. 67. Above 10 GeV the spectrum decreases steeply with energy. The spread between the models at radii $r < 10$ m is about 100%, and at $r = 100$ m 30%.

Fig. 68 gives the lateral distribution of electrons at observation level in 10^{14} and 10^{15} eV iron showers. The lines again indicate the results of a fit of the form

$$\rho(r) = a \left(\frac{r}{b}\right)^{c-2} \left(1 + \frac{r}{b}\right)^{4.5-d}$$

to the density values obtained from CORSIKA where r is the core distance and a, b, c, and d are the fit parameters. The parameters obtained are listed in Tab. 29. As in the case of proton showers the models approach each other for large radii. SIBYLL predicts the largest electron density in the center and DPMJET the lowest one.

The lateral distribution of muons in Fe induced showers is shown in Fig. 69. The variation for different models is about a factor of 2 at small radii and shrinks to about 30% at $r = 2$ km.

Fig. 70 shows the longitudinal shower development for 10^{14} and 10^{15} eV iron showers. SIBYLL showers develop late and give the highest number of electrons at ground level due to reasons which have been discussed already for proton induced showers. DPMJET is the other extreme. The positions of the shower maxima and the elongation rates are listed in Tab. 28. The elongation rates at these energies vary for protons and iron (see Tab. 22) by about 15 g/cm^2 per decade. SIBYLL and HDPM yield the largest and DPMJET the smallest variation of the shower maximum with energy. The errors in the average depth of the shower maximum are about 20 g/cm^2 for all models.

In Fig. 71 the distribution of electron numbers at 110 m a.s.l. is shown. The distributions have the same form, their average value reflects the electron numbers from Tab. 26. The widths of the distributions of different models in this logarithmic plot are about the same.

The distributions of the number of muons are displayed in Fig. 72. The Gribov-Regge type models agree rather well with each other, HDPM predicts more muons and SIBYLL less (see Tab. 26). The distributions are symmetric and do not display long tails as SIBYLL did in the proton case.

In Fig. 73 the distributions of simulated events are represented in the $\log_{10} N_e$-$\log_{10} N_\mu$ plane for primary protons and iron nuclei of 10^{14} and 10^{15} eV primary energy. The contours are drawn at half maximum of the respective distributions. In this graph it becomes very obvious that SIBYLL differs most from the other models in the muon-to-electron ratio. The extension of the Fe contours is much smaller than the corresponding proton contour. All models agree roughly in the separation of events of different primary mass.

In Fig. 74 averages for both energies are plotted in the $\log_{10} N_e$-$\log_{10} N_\mu$ plane. The averages for the two energies are connected by lines according to

$$\log N_\mu = \alpha \log N_e + c$$

and their slopes α are listed in Tab. 25. The slopes differ by about 10%, DPMJET giving the steepest rise and SIBYLL the flattest. SIBYLL has the largest distance to the other models. The slopes for the iron showers are flatter than the proton slopes by about 0.1.

energy	HDPM	VENUS	SIBYLL	QGSJET	DPMJET
10^{14} eV	12.7 ± 12.5	12.6 ± 13.6	12.5 ± 13.0	14.0 ± 13.3	12.8 ± 12.8
10^{15} eV	13.0 ± 12.0	12.5 ± 11.9	12.2 ± 11.7	13.0 ± 12.7	12.6 ± 12.5

Table 24: Average atmospheric depths of first interaction (in g/cm^2) for iron induced showers.

	p	Fe
VENUS	0.76	0.66
QGSJET	0.74	0.64
SIBYLL	0.71	0.60
HDPM	0.75	0.65
DPMJET	0.78	0.67

Table 25: Slopes of the energy dependence in the $\log_{10} N_e$-$\log_{10} N_\mu$ plane between 10^{14} and 10^{15} eV.

10^{14} eV					
	VENUS	QGSJET	SIBYLL	HDPM	DPMJET
p	60.8 ± 14.0	46.4 ± 14.6	48.7 ± 12.9	47.2 ± 12.3	56.4 ± 14.6
$\overline{p}$	0.7 ± 0.9	0.4 ± 0.7	0.5 ± 0.7	0.4 ± 0.7	0.7 ± 0.9
n	145.1 ± 27.1	111.6 ± 27.9	117.1 ± 24.2	112.8 ± 22.6	139.5 ± 27.9
$\overline{n}$	1.0 ± 1.0	0.6 ± 0.8	0.6 ± 0.8	0.6 ± 0.8	0.9 ± 1.0
μ^-	979.5 ± 78.1	974.6 ± 123.5	862.3 ± 67.9	1019.3 ± 82.4	926.7 ± 68.9
μ^+	1015.0 ± 81.8	1001.7 ± 125.0	890.4 ± 66.7	1050.0 ± 87.6	966.5 ± 73.2
π^-	3.5 ± 3.0	3.6 ± 3.3	3.5 ± 3.2	3.7 ± 2.9	3.1 ± 2.6
π^+	3.7 ± 3.1	3.5 ± 3.5	3.5 ± 3.2	3.9 ± 3.4	2.9 ± 2.7
K_L^0	0.1 ± 0.3	0.1 ± 0.3	0.1 ± 0.4	0.1 ± 0.3	0.1 ± 0.3
K_S^0	0.0 ± 0.0	0.0 ± 0.0	0.0 ± 0.0	0.0 ± 0.0	0.0 ± 0.0
K^-	0.0 ± 0.2	0.0 ± 0.2	0.0 ± 0.1	0.0 ± 0.2	0.0 ± 0.2
K^+	0.0 ± 0.2	0.0 ± 0.2	0.1 ± 0.2	0.0 ± 0.2	0.0 ± 0.2
$e^\pm$	2075 ± 634	2078 ± 892	2145 ± 707	2019 ± 654	1868 ± 620
10^{15} eV					
	VENUS	QGSJET	SIBYLL	HDPM	DPMJET
p	546.0 ± 91.3	407.6 ± 81.1	464.0 ± 73.0	457.5 ± 78.9	571.3 ± 91.2
$\overline{p}$	14.3 ± 4.7	8.2 ± 3.5	8.5 ± 3.3	11.3 ± 4.5	13.2 ± 4.8
n	1253.3 ± 180.1	950.6 ± 168.1	1047.7 ± 142.2	1063.1 ± 155.4	1318.5 ± 177.9
$\overline{n}$	18.6 ± 5.7	10.9 ± 4.5	11.0 ± 3.9	13.7 ± 4.6	17.2 ± 5.8
μ^-	7512.8 ± 534.2	7210.6 ± 664.7	6265.4 ± 423.0	8193.8 ± 560.8	7290.7 ± 473.9
μ^+	7795.4 ± 554.7	7423.4 ± 688.0	6441.1 ± 434.0	8451.0 ± 574.2	7612.1 ± 493.2
π^-	70.0 ± 22.7	62.9 ± 24.0	68.3 ± 22.4	83.0 ± 27.1	58.4 ± 21.7
π^+	72.7 ± 22.5	64.8 ± 23.9	70.3 ± 22.5	85.3 ± 28.1	61.4 ± 22.5
K_L^0	3.3 ± 2.1	2.6 ± 2.0	2.7 ± 2.0	2.3 ± 1.7	2.5 ± 2.1
K_S^0	0.0 ± 0.1	0.0 ± 0.1	0.0 ± 0.1	0.0 ± 0.1	0.0 ± 0.1
K^-	1.1 ± 1.1	0.9 ± 1.1	0.8 ± 1.0	0.9 ± 1.1	0.8 ± 1.0
K^+	1.1 ± 1.1	0.9 ± 1.0	1.1 ± 1.2	1.0 ± 1.1	0.8 ± 1.0
$e^\pm$	46010 ± 10174	47073 ± 11772	56741 ± 11324	50370 ± 11081	40611 ± 9458

Table 26: Average particle numbers and variances at observation level for iron induced showers at $E_0 = 10^{14}$ and 10^{15} eV.

energy	model	average number of muons above threshold energy				
		> 0.3 GeV	> 1 GeV	> 10 GeV	> 100 GeV	> 1 TeV
10^{14} eV	VENUS	1995	1767	633	37.0	0.012
	QGSJET	1976	1761	629	35.3	0.004
	SIBYLL	1753	1564	580	37.3	0.018
	HDPM	2069	1842	641	35.4	0.004
	DPMJET	1893	1681	602	36.7	0.036
10^{15} eV	VENUS	15308	13244	4399	342.2	6.732
	QGSJET	14634	12727	4129	309.9	6.370
	SIBYLL	12707	10984	3670	286.2	6.594
	HDPM	16645	14417	4515	322.3	6.258
	DPMJET	14903	12895	4194	310.1	6.934

Table 27: Average numbers of muons per shower above threshold energy in iron induced showers.

	depths of maximum at		difference
	$E = 10^{14}$ eV (g/cm^2)	$E = 10^{15}$ eV (g/cm^2)	(g/cm^2)
VENUS	355	439	84
QGSJET	355	442	87
SIBYLL	362	458	96
HDPM	352	444	91
DPMJET	353	428	75

Table 28: Average depths of maximum for iron induced showers at 10^{14} and 10^{15}eV.

energy	model	a $\times 10^{-3}$	b (m)	c	d
10^{14} eV	VENUS	0.0682	25.4	2.28	1.53
	QGSJET	0.0639	25.9	2.10	1.69
	SIBYLL	0.0428	41.8	1.92	1.40
	HDPM	0.0203	57.5	1.80	1.48
	DPMJET	0.0897	17.1	2.46	1.60
10^{15} eV	VENUS	2.09	24.8	1.75	1.76
	QGSJET	1.70	29.4	1.62	1.70
	SIBYLL	1.80	32.6	1.53	1.67
	HDPM	1.03	39.7	1.49	1.68
	DPMJET	0.98	33.2	1.55	1.88

Table 29: Parameters of lateral distributions of electrons for iron induced showers at 10^{14} a nd 10^{15} eV.

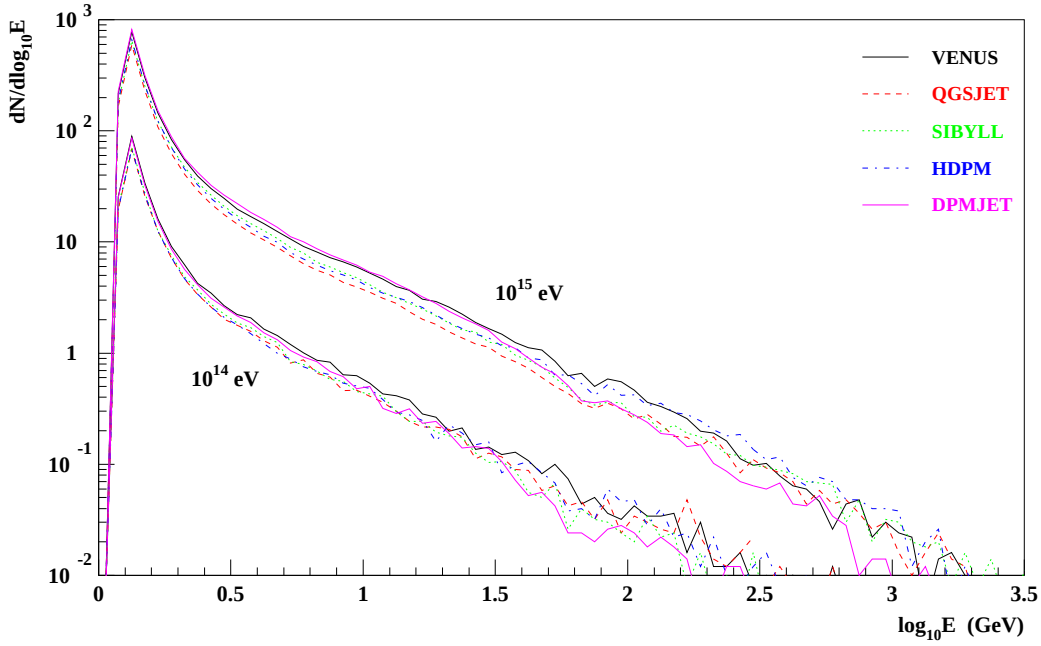

Figure 64: Energy spectra of all baryons at 110 m a.s.l. for iron induced showers with $E_0 = 10^{14}$ and 10^{15} eV.

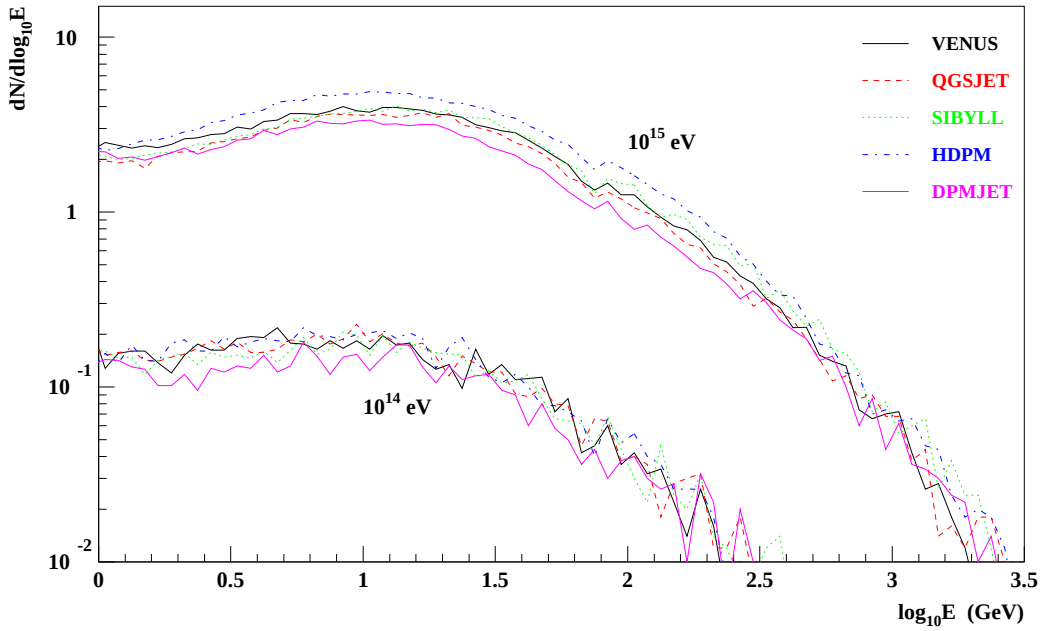

Figure 65: Energy spectra of charged pions at 110 m a.s.l. for iron induced showers with $E_0 = 10^{14}$ and 10^{15} eV.

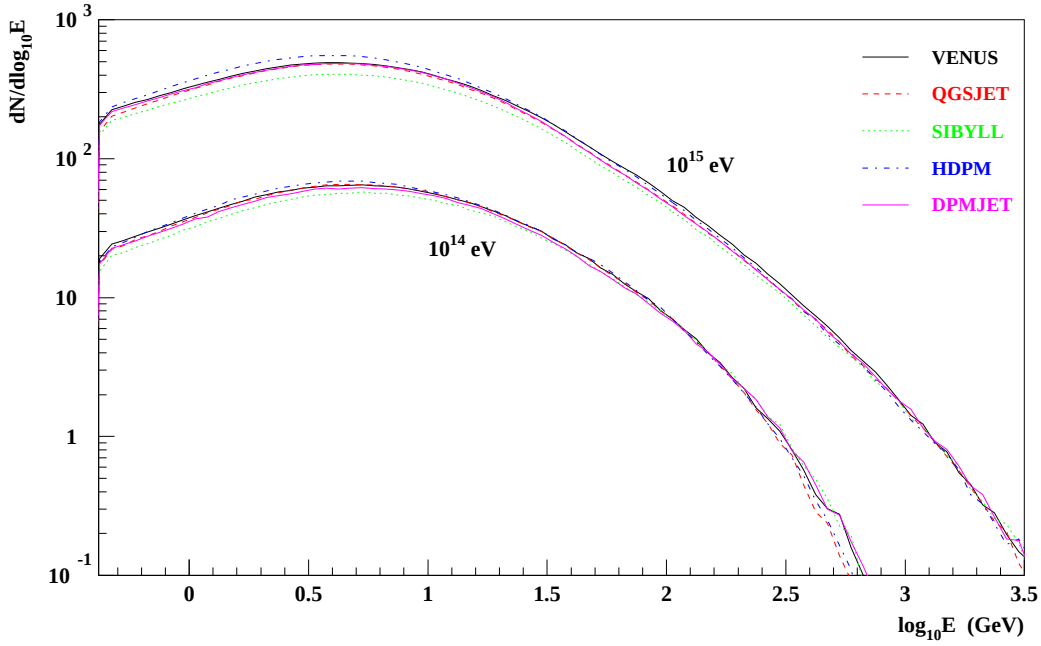

Figure 66: Energy spectra of muons at 110 m a.s.l. for iron induced showers with $E_0 = 10^{14}$ and 10^{15} eV.

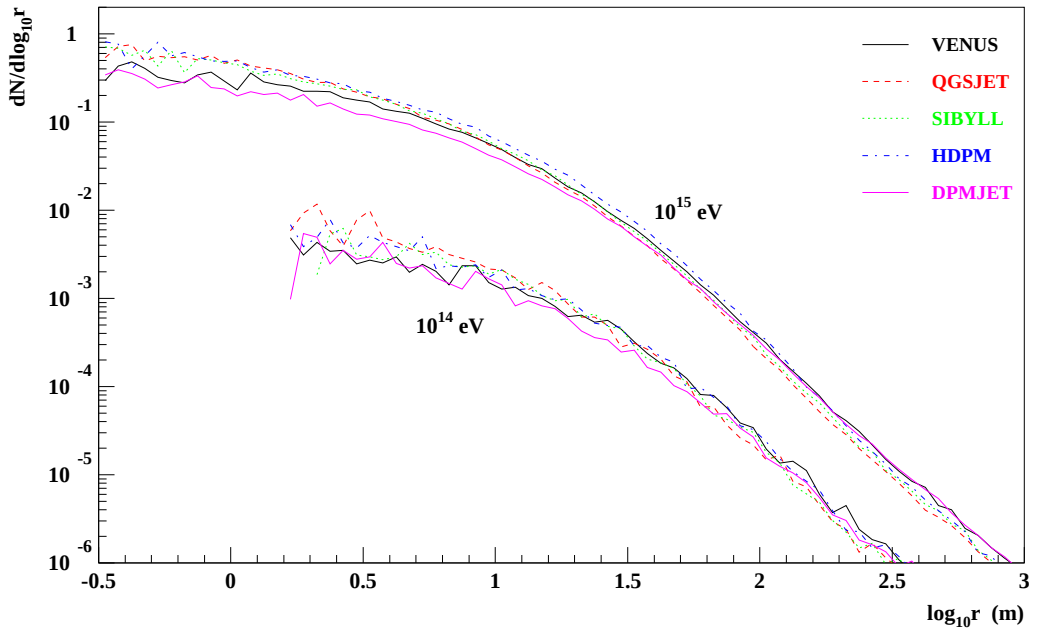

Figure 67: Lateral distributions of charged pions at 110 m a.s.l. for iron induced showers with $E_0 = 10^{14}$ and 10^{15} eV.

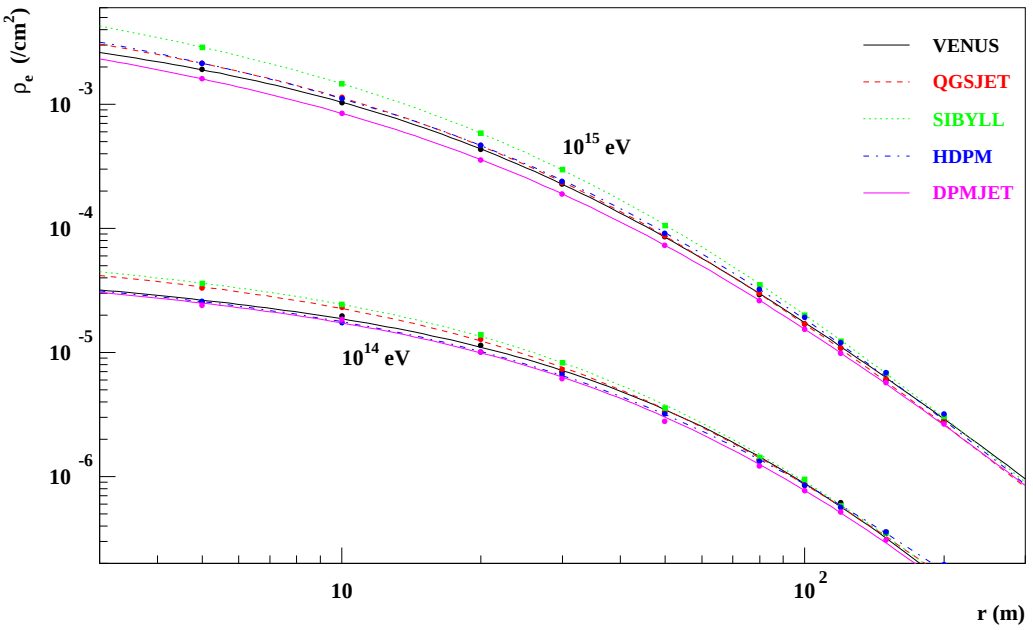

Figure 68: Lateral distributions of electrons at 110 m a.s.l. for iron induced showers with $E_0 = 10^{14}$ and 10^{15} eV. The lines represent fits to the Monte Carlo data.

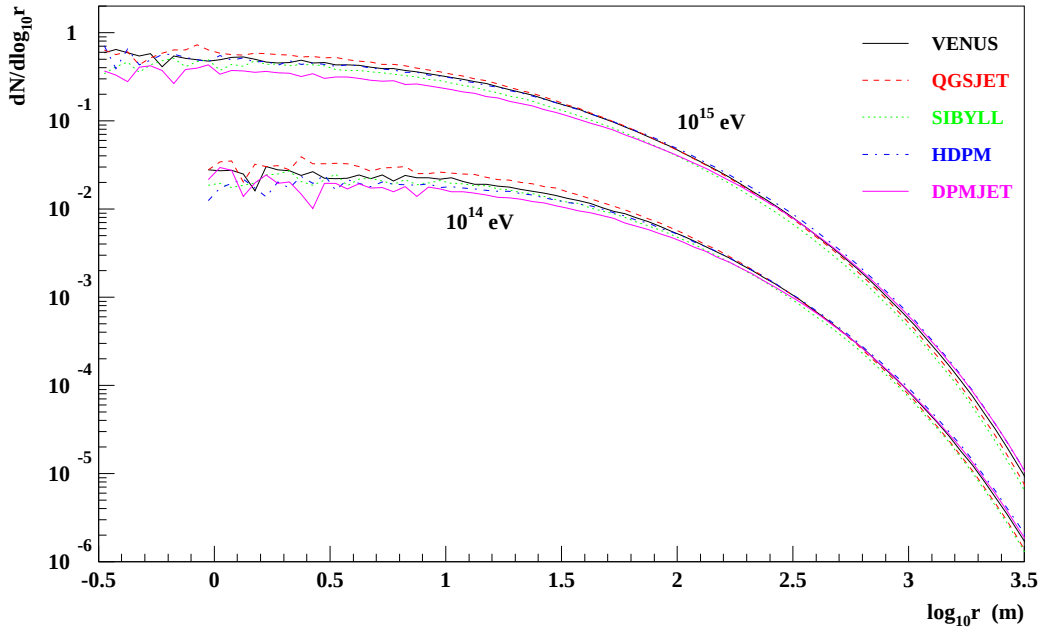

Figure 69: Lateral distributions of muons at 110 m a.s.l. for iron induced showers with $E_0 = 10^{14}$ and 10^{15} eV.

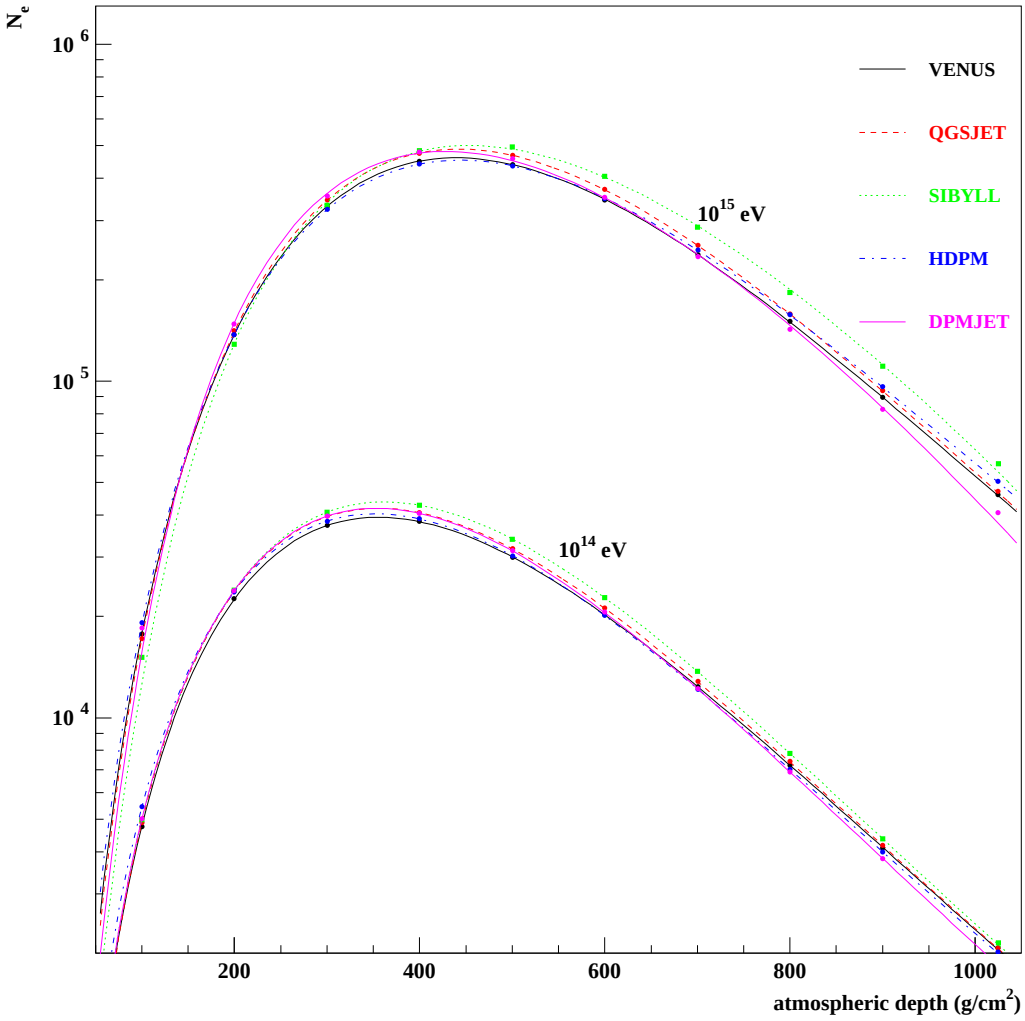

Figure 70: Longitudinal distributions of electrons for iron induced showers with $E_0 = 10^{14}$ and 10^{15} eV. The lines represent fits to the Monte Carlo data.

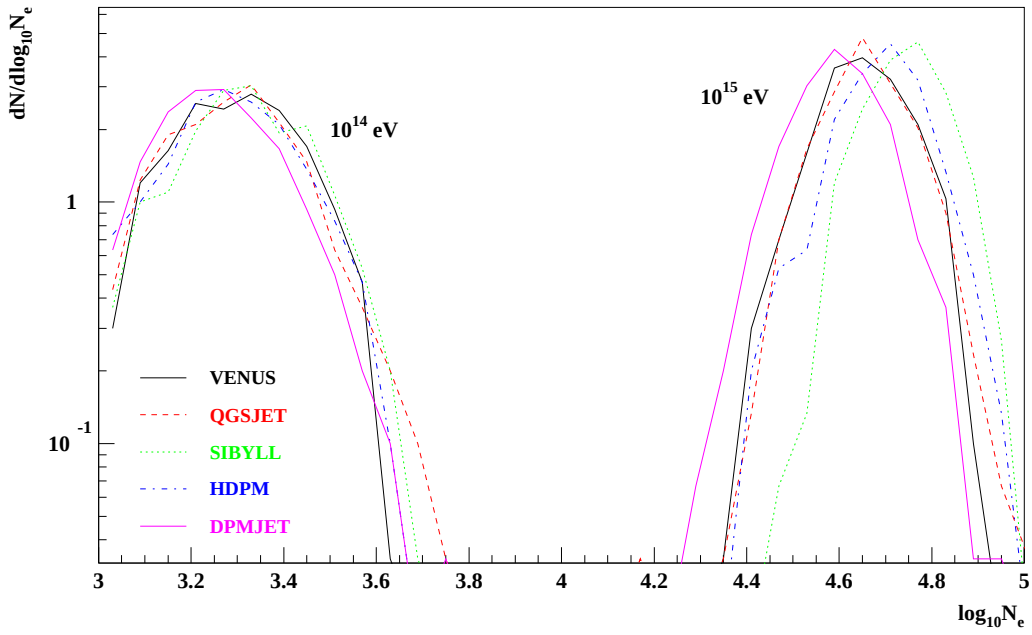

Figure 71: Distributions of electron number at 110 m a.s.l. for iron induced showers with $E_0 = 10^{14}$ and 10^{15} eV.

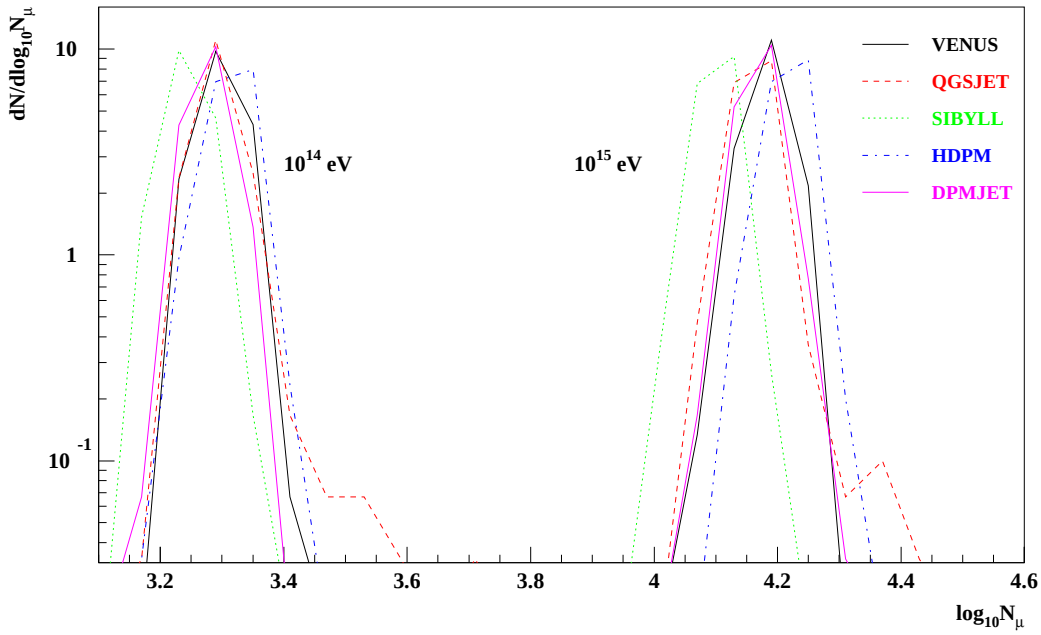

Figure 72: Distributions of muon number at 110 m a.s.l. for iron induced showers with $E_0 = 10^{14}$ and 10^{15} eV.

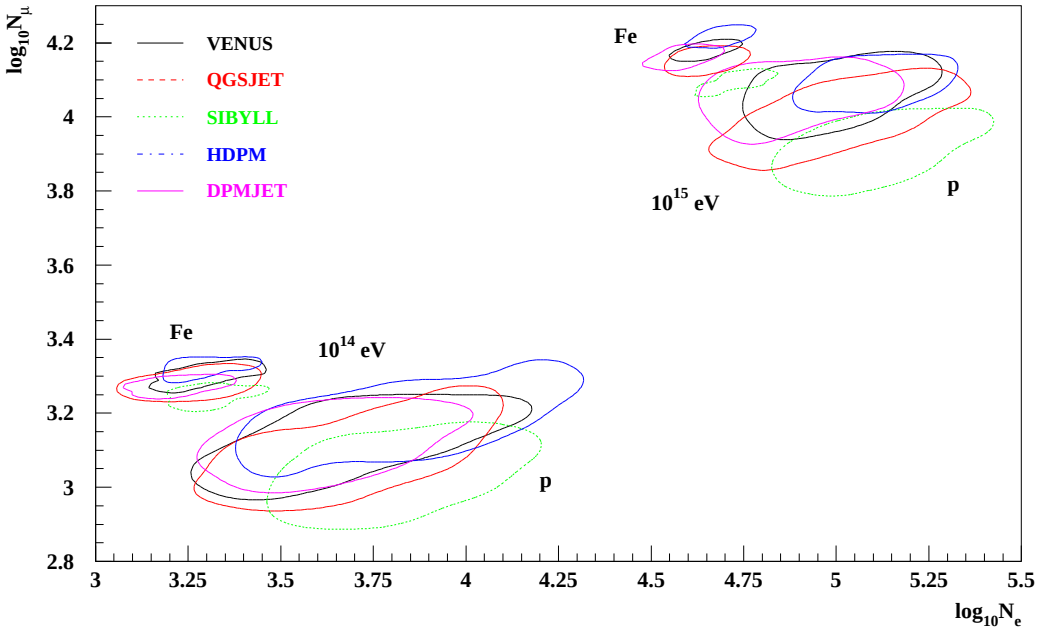

Figure 73: Smoothed contours of $\log N_\mu$ vs. $\log N_e$ for primary proton and iron showers at $E_0 = 10^{14}$ and 10^{15} eV.

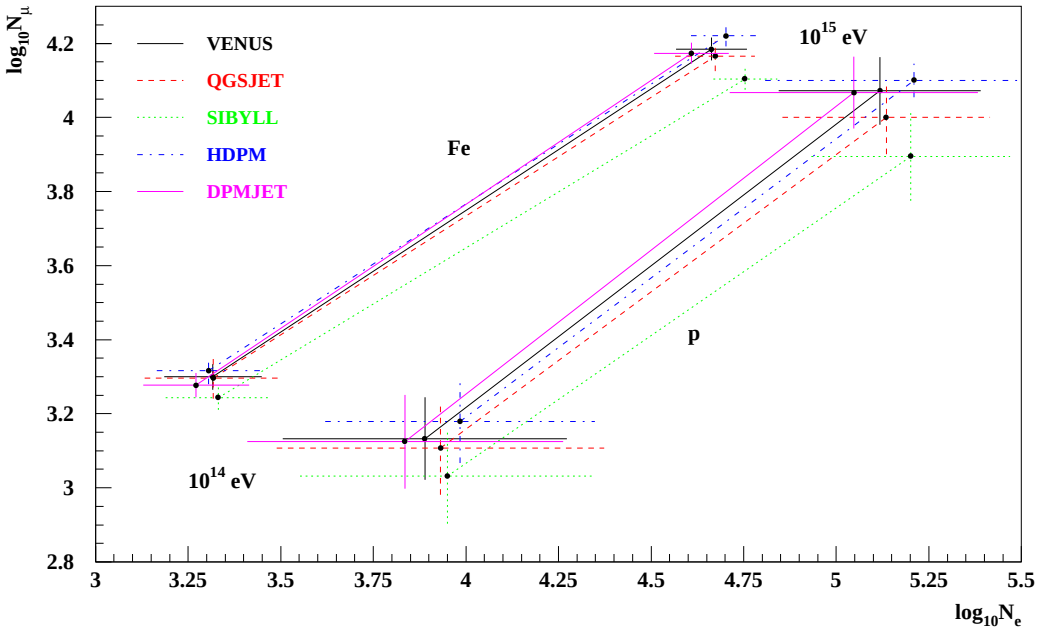

Figure 74: $\log_{10} N_\mu$ versus $\log_{10} N_e$ for primary proton and iron showers at $E_0 = 10^{14}$ and 10^{15} eV.

4 Concluding Remarks

On the whole, we find it difficult to correlate the observed differences in the results of the shower calculations from section 3 to the differences in individual interactions as described in section 2.

Nevertheless, some correlations are obvious. The elasticities of the interactions are connected with the longitudinal shower development, with the lateral electron distribution, and with the number of charged pions observed at ground level. In DPMJET the elasticity is lowest which causes an early development of the showers and a steep decrease after the shower maximum combined with a flat lateral electron distribution. For HDPM, the model with the highest elasticity, the maximum is reached deepest and attenuation following the maximum is the flattest. Consequently, there are still high energy baryons present in the shower core near observation level, producing secondaries which cause high electron and pion densities at small core distances.

A general feature of our results is that differences between models are smaller for iron primaries than for primary protons but show the same tendency. Since the superposition model is applied implicitly except for the first interaction, this is not self-evident. One should be aware, though, that an iron nucleus of 10^{15} eV corresponds to an energy per nucleon of 18 TeV, i.e much lower than the corresponding proton shower calculations.

It should be emphasized once more that the comparisons described in this report cannot give preference to one or another of the interaction models. The differences can only be considered as an indication (or lower limit) of the prevailing systematic uncertainties. It might be possible in principle to decide between models by comparing these or similar calculations with experimental data. We feel that this is far from trivial, among other reasons because this is only possible in a straightforward way, if the problem of primary composition has been solved - in itself a non-trivial task. However, some progress in that direction may be expected from the new generation of large EAS experiments such as CASA-MIA-DICE, HEGRA, and KASCADE. Three of the models investigated (DPMJET, QGSJET, and VENUS) start from the same basic physical approach. Nevertheless, clear differences in the results exist, indicating systematic uncertainties still inherent in this approach. This is even more a matter of concern, because these models may be expected to extrapolate more reliably to the highest energies.

Acknowledgment

This work would not have been possible without the help of J.N. Capdevielle, R.S. Fletcher, T.K. Gaisser, N.N. Kalmykov, P. Lipari, S.S. Ostapchenko, J. Ranft, T. Stanev, and K. Werner. We gratefully acknowledge the permission to use their hadronic interaction codes within CORSIKA, their generous support during the implementation phase, and many useful discussions.

References

[1] F. Abe et al., CDF Collaboration, *Phys. Rev. D* **41** (1990) 2330

[2] C. Albajar et al., UA1 Collaboration, *Nucl. Phys. B* **335** (1990) 261

[3] G.J. Alner et al., UA5 Collaboration, *Z. Phys. C* **33** (1986) 1

[4] G.J. Alner et al., UA5 Collaboration, *Phys. Lett. B* **167** (1986) 476

[5] G.J. Alner et al., UA5 Collaboration, *Phys. Rep.* **154** (1987) 247

[6] K. Alpgård et al., UA5 Collaboration, *Phys. Lett. B* **112** (1982) 183

[7] R.E. Ansorge et al., UA5 Collaboration, *Nucl. Phys. B* **328** (1989) 36

[8] R.E. Ansorge et al., UA5 Collaboration, *Z. Phys. C* **43** (1989) 357

[9] J.N. Capdevielle, KASCADE Collaboration, *Proc. 22nd Int. Cosmic Ray Conf. Dublin* **4** (1991) 405

[10] J.N. Capdevielle et al., *The Karlsruhe Extensive Air Shower Simulation Code CORSIKA, Kernforschungszentrum Karlsruhe* **KfK 4998** (1992)

[11] H. Fesefeldt, *The Simulation of Hadronic Showers -Physics and Application-, Rheinisch-Westfälische Technische Hochschule, Aachen* **PITHA 85/02** (1985)

[12] R.S. Fletcher, T.K. Gaisser, P. Lipari, T. Stanev, *Phys. Rev. D* **50** (1994) 5710
J. Engel, T.K. Gaisser, P. Lipari, T. Stanev, *Phys. Rev. D* **46** (1992) 5013

[13] M. Gazdzicki, O. Hansen, *Nucl. Phys.* **A528** (1991) 754

[14] C. Geich-Gimbel, *Int. J. Mod. Phys. A* **4** (1989) 1527

[15] N.N. Kalmykov, S.S. Ostapchenko, *Yad. Fiz.* **56** (1993) 105
N.N. Kalmykov, S.S. Ostapchenko, *Phys. At. Nucl.* **56** (3) (1993) 346
N.N. Kalmykov, S.S. Ostapchenko, A.I. Pavlov, *Bull. Russ. Acad. Sci. (Physics)* **58** (1994) 1966

[16] J. Knapp, D. Heck, *Extensive Air Shower Simulation with CORSIKA: A User's Manual, Kernforschungszentrum Karlsruhe* **KfK 5196 B** (1993)

[17] J. Ranft, *Phys. Rev. D* **51** (1995) 64

[18] W. Thomé et al., *Nucl. Phys. B* **129** (1977) 365

[19] K. Werner, *Phys. Rep.* **232** (1993) 87

[20] J. Whitmore et al., *Phys. Rep.* **10** (1974) 273

List of Figures

List of Tables